

UC Irvine

UC Irvine Electronic Theses and Dissertations

Title

Secondary Coordination Sphere Effects on Properties and Reactivities of Metal complexes

Permalink

<https://escholarship.org/uc/item/4t27b07h>

Author

Sun, Chen

Publication Date

2021

Peer reviewed|Thesis/dissertation

University of California,

Irvine

Secondary Coordination Sphere Effects on Properties and
Reactivities of Metal complexes

Dissertation

Submitted in partial satisfaction of the requirements

for the degree of

DCOTOR OF PHILOSOPHY

in Chemistry

by

Chen (Sunny) Sun

Dissertation Committee:

Professor A.S. Borovik, Chair

Professor Alan F. Heyduk

Professor Jenny Y. Yang

2021

Portion of Chapter 2 © 2019 American Chemical Society
Portion of Chapter 3 © 2021 Royal Society of Chemistry
All other materials © 2021 Sunny Sun

Table of Contents

List of Figures	iii
List of Schemes.....	ix
List of Tables.....	x
acknowledgement	xi
Curriculum Vitae	xiii
Abstract of The Dissertation	xv
Chapter 1 – Introduction.....	1
Chapter 2 – Regulating Basicity and Reactivity of Terminal Mn ^{III} -oxido Complexes with a Single Hydrogen Bond.....	13
Chapter 3 – Investigation of Iron–Ammine and Amido Complexes within a C ₃ -Symmetrical Phosphinic Amido Tripodal Ligand.....	39
Chapter 4 – Reactivity of Fe ^{IV} -oxido complex in C ₃ -symmetric phosphoryl amido tripodal framework.....	64
Chapter 5 – Binding of α-keto Acids with Tripodal Iron Complexes.....	97

List of Figures

Figure 1-1. (A) The active site in the OEC (PDB:3WU2), illustrating the {Mn ₄ CaO ₅ } cluster and H-bonding network. (B) The active site in the oxymyoglobin (PDB: 1A6M), illustrating the iron heme center and H-bonding to the O ₂ ligand. (C) The active site in the TauD (PDB: 1OS7), illustrating the resting state of the iron center with taurine anchored in close proximity by H-bonding interaction. (D) The active site in the SLO (PDB: 1F8N). All H-bonding interactions are highlighted with black dashed lines.	2
Figure 1-2. (A) Structurally characterized picket fence porphyrin complex supporting an Fe–O ₂ adduct. (B) Modified picket fence porphyrin complex containing a urea group capable of H-bonding.	4
Figure 1-3. (A) Fe ^{II} -OH complexes isolated by the Fout group (B) Dizinc peroxide complex isolated by the Szymczak group.	4
Figure 1-4. Complexes in various C ₃ -tripodal frameworks designed by the Borovik lab.	5
Figure 1-5. (A) [Mn ^{III} H ₃ buea(O)] ²⁻ complex. (B) [Mn ^{III} H ₃ bpuea-R(O)] ²⁻ complexes.	7
Figure 1-6. Fe ^{III} -NH ₃ complexes in the (A) [MST] ³⁻ and (B) [poat] ³⁻ ligand framework.	7
Figure 1-7. Fe ^{IV} -oxido complexes in C ₃ -symmetric tripodal ligand framework.	8
Figure 1-8. Proposed intramolecular proton transfer to form the [Fe ^{II} HPOP(PhP)] ²⁻ complex.	9
Figure 2-1. Molecular structure of (A) K ₂ [Mn ^{III} H ₃ bpuea-OMe(O)] and (B) K ₂ [Mn ^{III} H ₂ bpuea-OMe(OH)]. Thermal ellipsoids are shown at the 50% probability level. Only ureayl and hydroxide hydrogen atoms are shown for clarity. Solvent molecules and potassium counter ions were omitted for clarity.	18
Figure 2-2. (A) Electronic absorption spectrum of [Mn ^{III} (O)-OMe] ²⁻ in DMSO at room temperature. (B) EPR spectrum (//-mode, 2:1 DMF:THF, 10 K, 21.4 mM) of [Mn ^{III} (O)-OMe] ²⁻	19
Figure 2-3. (A) Titration of [Mn ^{III} (O)-OMe] ²⁻ with 2-aminopyrimidine by monitoring the intensity at 714 nm. (B) Plot for determination of equilibrium constant and pK _a	22

Figure 2-4. (A) EPR spectrum (\perp -mode, 10 K, 2:1 DMF:THF, 24.5 mM) of the $[\text{Mn}^{\text{II}}(\text{OH})\text{-OMe}]^{2-}$ complex. (B) Cyclic voltammogram of the $[\text{Mn}^{\text{II}}(\text{OH})\text{-OMe}]^{2-}$ complex measured in DMSO with glassy carbon working electrode, platinum wire counter electrode, silver wire reference electrode, and FeCp_2 as internal standard.	22
Figure 2-5. Hammett analysis with $\text{p}K_{\text{a}}$ values of the $[\text{Mn}^{\text{III}}(\text{O})\text{-R}]^{2-}$ complexes.	24
Figure 2-6. (A) Reaction between the $[\text{Mn}^{\text{II}}(\text{OH})\text{-OMe}]^{2-}$ complex (2mM) and excess DHA. (B) Plot of k_{obs} versus concentration of DHA. The slope of this linear relationship was used for determination of second order rate constant. The pseudo-first order rate constant of complexes $\text{R} = \text{OMe}, \text{H}, \text{F},$ and Cl were determined based on the feature at 500 nm, whereas that of $\text{R} = \text{CF}_3$ was determined based on the feature at 650 nm.	25
Figure 2-7. (A) Plot of $\log(k)$ vs $\text{p}K_{\text{a}}$ for the oxidation of DHA and (B) Hammett analysis for the oxidation of DHA for the $[\text{Mn}^{\text{III}}(\text{O})\text{-R}]^{2-}$ complexes.	26
Figure 2-8. Eyring analysis of the $[\text{Mn}^{\text{II}}(\text{OH})\text{-OMe}]^{2-}$ complex.	27
Figure 2-9. Second order rate constant of $[\text{Mn}^{\text{II}}(\text{OH})\text{-OMe}]^{2-}$ complex with DHA (black) and d_4 -DHA (blue).	27
Figure 3-1. Diagrams of (A) $[\text{MST}]^{3-}$, (B) $[\text{Fe}^{\text{III}}\text{MST}(\text{NH}_3)]^{-0}$ complexes, and (C) $[\text{poat}]^{3-}$	40
Figure 3-2. CV of (A) $\text{K}(\text{crypt})[\text{Fe}^{\text{II}}\text{poat}(\text{NH}_3)]$ and (B) $\text{Na}[\text{Fe}^{\text{II}}\text{MST}(\text{NH}_3)]$ in DCM:THF. The measurement was done with 100 mV/s scan rate using 100 mM tetrabutylammonium hexafluorophosphate (TBAPF_6) as electrolyte, glassy carbon electrode as working electrode, platinum wire as counter electrode, silver wire as reference electrode, and $[\text{Fe}^{\text{III}}\text{Cp}_2]^{+/0}$ couple as internal standard.	43
Figure 3-3. (A) Electronic absorption spectra of $\text{K}(\text{crypt})[\text{Fe}^{\text{II}}\text{poat}(\text{NH}_3)]$ (grey) and $[\text{Fe}^{\text{III}}\text{poat}(\text{NH}_3)]$ (black) in DCM. (B) EPR spectra of $\text{K}(\text{crypt})[\text{Fe}^{\text{II}}\text{poat}(\text{NH}_3)]$ (grey, \parallel -mode, 10K, 10.0 mM, DMF:THF) and $[\text{Fe}^{\text{III}}\text{poat}(\text{NH}_3)]$ (black, \perp -mode, 77 K, 13 mM, DCM:THF). Asterisks in panel B indicate signals from small amounts of impurities.	44
Figure 3-4. Thermal ellipsoid plots of (A) $\text{K}(\text{crypt})[\text{Fe}^{\text{II}}\text{poat}(\text{NH}_3)]$ and (B) $[\text{Fe}^{\text{III}}\text{poat}(\text{NH}_3)]$ determined by XRD methods. Only hydrogen atoms on NH_3 are shown; solvent molecules are omitted for clarity. Ellipsoids are drawn at the 50% probability.	45
Figure 3-5. Solid state FT-IR spectra of $\text{K}(\text{crypt})[\text{Fe}^{\text{II}}\text{poat}(\text{NH}_3)]$ (dashed line), and $[\text{Fe}^{\text{III}}\text{poat}(\text{NH}_3)]$ (solid line).	48

Figure 3-6. (A) Electronic absorption spectra of before (black) and after (blue) addition of excess TBD to 0.13 mM $[\text{Fe}^{\text{III}}\text{poat}(\text{NH}_3)]$ (black) in DCM. (B) EPR spectra of before (black) and after (blue) adding TBD to $[\text{Fe}^{\text{III}}\text{poat}(\text{NH}_3)]$ in DCM:THF (\perp -mode, 77 K, 13 mM). Asterisks in panel B indicate signals from small amounts of impurities.49

Figure 3-7. (A) Electronic absorption spectrum and (B) EPR spectrum (\perp -mode, 3.9 K) of $\text{K}[\text{Fe}^{\text{III}}\text{poat}(\text{NHtOl})]$ in DMF:THF. Asterisks in panel B indicate signals from small amounts of impurities.50

Figure 3-8. Thermal ellipsoid plots of $[\text{Fe}^{\text{III}}\text{poat}(\text{NHtOl})]^-$ determined by XRD methods. Only the hydrogen atom on amido ligand is shown. Carbon atoms on the amido ligand are highlighted in grey to distinguish from the other carbon atoms. Ellipsoids are drawn at the 50% probability. Only one orientation of the disordered molecule is shown.51

Figure 4-1. Three C_3 -symmetric tripodal ligand frameworks developed in the Borovik lab: $[\text{H}_3\text{buea}]^{3-}$, $[\text{poat}]^{3-}$, and $[\text{POP}]^{3-}$66

Figure 4-2. Illustration of $[\text{Fe}^{\text{IV}}\text{H}_3\text{buea}(\text{O})]^-$, $[\text{Fe}^{\text{IV}}\text{poat}(\text{O})]^-$, and space fill model of $[\text{Fe}^{\text{II}}\text{poat}(\text{H}_2\text{O})]^-$ (View from the top).66

Figure 4-3. Molecular structure of (A) $\{\text{K}[\text{Fe}^{\text{II}}\text{POP}(\text{H}_2\text{O})]\}_2$ as the aggregate and (B) view of $\text{K}[\text{Fe}^{\text{II}}\text{POP}(\text{H}_2\text{O})]$ fragment determined by XRD methods. Only hydrogen atoms on H_2O ligand are shown. Ellipsoids are drawn at 50% probability.69

Figure 4-4. (A1) Electronic absorption spectra of 0.39 mM $\text{K}[\text{Fe}^{\text{II}}\text{POP}]$ (grey) in the presents of 2 equiv. 18C6 and after addition of IBX-iPr (black) in dimethylformamide (DMF):THF at -80 °C. (A2) zoomed in view of the 900 nm transition for $[\text{Fe}^{\text{IV}}\text{POP}(\text{O})]^-$ when generated using 1.9 mM $\text{K}[\text{Fe}^{\text{II}}\text{POP}(\text{H}_2\text{O})]$ as the starting complex. (B) EPR spectra (\parallel -mode, 12.3 K, DMF:THF) of 15.8 mM $\text{K}[\text{Fe}^{\text{II}}\text{POP}]$ (grey) and after addition of IBX-iPr (black) at -80 °C. Asterisks in panel B indicate signals from small amounts of ferric impurities.69

Figure 4-5. The UV-vis spectra of monitoring self-decay of $[\text{Fe}^{\text{IV}}\text{POP}(\text{O})]^-$ (2 mM) at -20 °C in DMF. The starting complex for formation of $[\text{Fe}^{\text{IV}}\text{POP}(\text{O})]^-$ is either $\text{K}[\text{Fe}^{\text{II}}\text{POP}]$ or $\text{K}[\text{Fe}^{\text{II}}\text{POP}(\text{H}_2\text{O})]$. Determination of k_{obs} was done using absorbances monitored at 900 nm.69

Figure 4-6. (A) Example of TauD (PDB:1OS7) having taurine anchored within the active site by H-bonding between Asn₉₅ and Tau. (B) Three substrates used for comparing reactivity. (C) Proposed H-bonding interaction between benzyl alcohol and the $[\text{Fe}^{\text{IV}}\text{POP}(\text{O})]^-$ complex.73

Figure 4-7. (A) Gas chromatogram and (B) mass spectrum at retention time = 3.36 min from the GC-MS measurement in DCM for the extracted organic product from the bulk reaction.	74
Figure 4-8. ¹ H NMR measurement in <i>d</i> ₆ -DMSO of benzaldehyde reference (grey), the extracted organic product from the controlled experiment without substrate as reference (black), and the extracted organic product from the reaction with benzyl alcohol (blue).	74
Figure 4-9. (A) EPR spectrum (⊥-mode, 8.2 K, DMF:THF) of the inorganic product prepared as bulk synthesis of [Fe ^{IV} POP(O)] ⁻ + benzyl alcohol in an EPR tube. (B) zoomed in view of the low field region.	75
Figure 4-10. Comparison of the self-decay rate monitored via electronic absorption spectra at 900 nm band of [Fe ^{IV} POP(O)] ⁻ complex in DMF vs. in DMF:THF at -40 °C.	76
Figure 4-11. (A) The electronic absorption spectra of 1.9 mM [Fe ^{IV} POP(O)] ⁻ complex monitored at 900 nm during reaction with benzyl alcohol as substrate in DMF at -20 °C. (B) Plot of $\ln\left(\frac{A-A_f}{A_i-A_f}\right)$ vs. time corresponding to the change of intensity at 900 nm band for determination of pseudo-first order rate constant (<i>k</i> _{obs}).	77
Figure 4-12. (A) Plot of <i>k</i> _{obs} vs. concentration of 4-R-benzyl alcohol in DMF at -20 °C and (B) a zoomed-in version for substrates with R = H, Me, and OMe. The slopes of these linear equations are used for determining second order rate constant of the reaction between [Fe ^{IV} POP(O)] ⁻ complex and substrates.	77
Figure 4-13. Hammett plot for reactivity of [Fe ^{IV} POP(O)] ⁻ complex with <i>para</i> -substituted benzyl alcohols as substrates in DMF at -20 °C.	78
Figure 4-14. Plot for reactivity of [Fe ^{IV} POP(O)] ⁻ complex with benzyl alcohols and <i>d</i> ₂ -benzyl alcohol as substrates in DMF at -20 °C. The ratio of the measured <i>k</i> _{obs} for the two reactions is used to determine a KIE of 15.	79
Figure 4-15. ¹ H NMR studies of [Zn ^{II} POP(H ₂ O)] ⁻ + 4-Cl-benzyl alcohol in <i>d</i> ₆ -DMSO. Chemical shift also observed when same experiment was done using 4-Me-benzyl alcohol and 4-OMe-benzyl alcohol. Shift of [Zn ^{II} POP(H ₂ O)] ⁻ aqua ligand in experiments with 4-OMe-benzyl alcohol resulted in overlap with the substrate O–H peak and is reported in approximate value.	80
Figure 4-16. Proposed docking of 4-R-benzyl alcohol to the [Fe ^{II} POP(H ₂ O)] ⁻ complex in solution state based on ¹ H NMR studies of [Zn ^{II} POP(H ₂ O)] ⁻ + 4-R-benzyl alcohol in <i>d</i> ₆ -DMSO.	81

Figure 4-17. (A) Electronic absorption spectra of 2 mM $[\text{Fe}^{\text{IV}}\text{POP}(\text{O})]^-$ (black) and after adding d_2 -benzyl alcohol to it (grey) at $-60\text{ }^\circ\text{C}$ in DMF. (B) EPR spectra ($//$ -mode, DMF:THF) of 15 mM $[\text{Fe}^{\text{IV}}\text{POP}(\text{O})]^-$ (black, 6.6 K) and after adding d_2 -benzyl alcohol (grey, 8.9 K) at $-80\text{ }^\circ\text{C}$82

Figure 4-18. (A) $[\text{Fe}^{\text{IV}}\text{poat}(\text{O})]^-$ and $[\text{Fe}^{\text{IV}}\text{POP}(\text{O})]^-$. (B) Plot of k_{obs} vs. concentration of benzyl alcohol in DMF at $-20\text{ }^\circ\text{C}$ for $[\text{Fe}^{\text{IV}}\text{POP}(\text{O})]^-$ (black) and $[\text{Fe}^{\text{IV}}\text{poat}(\text{O})]^-$ (grey).83

Figure 4-S1. Plot of k_{obs} vs. concentration of $[\text{Fe}^{\text{IV}}\text{POP}(\text{O})]^-$ complex and rate vs. concentration of $[\text{Fe}^{\text{IV}}\text{POP}(\text{O})]^-$ complex during the reaction of $[\text{Fe}^{\text{IV}}\text{POP}(\text{O})]^-$ complex with benzyl alcohol under pseudo-first order condition.92

Figure 5-1. Mechanism of Taurine Dioxygenase (TauD).97

Figure 5-2. Examples of structurally characterized α -keto acids bound Fe^{II} complexes.98

Figure 5-3. C_3 -symmetric tripodal ligand frameworks developed in the Borovik lab hosting Fe^{IV} -oxido moiety: $[\text{Fe}^{\text{IV}}\text{poat}(\text{O})]^-$ and $[\text{Fe}^{\text{IV}}\text{POP}(\text{O})]^-$98

Figure 5-4. Two Fe^{II} -OAc complexes isolated in less sterically hindered ligand frameworks developed in the Borovik lab.100

Figure 5-5. (A) Molecular structure of $\{\text{Na}(\text{NMe}_4)[\text{Fe}^{\text{II}}\text{POP}(\text{OAc})]\}_2$ and (B) view of $\text{Na}(\text{NMe}_4)[\text{Fe}^{\text{II}}\text{POP}(\text{OAc})]$ fragment determined by XRD methods. The carbon atoms on acetate ligand (C1 and C2) are highlighted to distinguish from other carbon atoms. Hydrogen atoms and $(\text{NMe}_4)^+$ counter ions were omitted for clarity. Ellipsoids are drawn at 50% probability.101

Figure 5-6. (A) Molecular structure of $\{\text{Na}(\text{NMe}_4)[\text{Fe}^{\text{II}}\text{HPOP}(\text{PhP})]\}_2$ and (B) view of $\text{Na}(\text{NMe}_4)[\text{Fe}^{\text{II}}\text{HPOP}(\text{PhP})]$ fragment determined by XRD methods. The carbon atoms on $[\text{PhP}]^{2-}$ ligand (C1, C2, C3, and the phenyl ring) are highlighted to distinguish from other carbon atoms. Hydrogen atoms and outer sphere $(\text{NMe}_4)^+$ counter ion were omitted for clarity. Ellipsoids are drawn at 50% probability. Only one orientation of the disordered components is shown. H-bonding in (A) is not shown due to congestion of the figure.103

Figure 5-7. EPR spectrum ($//$ -mode, 15.9 K, DMF:THF) of $[\text{Fe}^{\text{II}}\text{POP}(\text{OAc})]^{2-}$ complex (15.3 mM).104

Figure 5-8. (A) Electronic absorption spectrum of $[\text{Fe}^{\text{II}}\text{POP}(\text{PhP})]^{2-}$ complex (0.39 mM) in DMF:THF at $-60\text{ }^\circ\text{C}$. (B) EPR spectrum ($//$ -mode, 15.9 K, DMF:THF) of $[\text{Fe}^{\text{II}}\text{POP}(\text{PhP})]^{2-}$ complex (49.6 mM).106

Figure 5-9. (A) Electronic absorption spectrum of putative Fe^{II}-PGA complex in DMSO at 20 °C (B) EPR spectrum (//-mode, 19.0 K, DMSO) of Fe^{II}-PGA complex.108

Figure 5-10. Solid state FTIR spectra of Na(NMe₄)[Fe^{II}POP(OAc)] (black), Na(NMe₄)[Fe^{II}HPOP(PhP)] (red), and the putative [Fe^{II}HPOP(PGA)]⁻ complex (blue).109

Figure 5-11. (A) Electronic absorption spectrum of the putative [Fe^{II}Hpoat(PGA)]⁻ complex collected in DMSO at 20 °C (B) EPR spectrum (//-mode, 19.0 K, DMSO) of the putative [Fe^{II}Hpoat(PGA)]⁻ complex.110

Figure 5-12. (A) Electronic absorption spectrum of [Fe^{II}HPOP(PhP)]²⁻ complex (grey) and 10 min after addition of 3 equiv. O₂ (black) in DMF:THF at -60 °C. (B) EPR spectrum (⊥-mode, 15.9 K, DMF:THF) after addition of 3 equiv. O₂ to the [Fe^{II}POP(PhP)]²⁻ complex.110

Figure 5-13. (A) Electronic absorption spectrum of the putative [Fe^{II}HPOP(PGA)]⁻ complex (grey) and 20 min after addition of 3 equiv. O₂ (black) in DMF:THF at -60 °C. (B) EPR spectrum (⊥-mode, 15.9 K, DMSO) after addition of 3 equiv. O₂ to the putative [Fe^{II}HPOP(PGA)]⁻ complex.110

Figure 5-14. (A) Electronic absorption spectra of [Fe^{II}HPOP(PhP)]²⁻ complex (grey) and the reaction after addition of FeCp₂BF₄ (black) in DMF:THF at -60 °C. (B) Electronic absorption spectra of the putative [Fe^{II}HPOP(PGA)]⁻ complex (grey) and the reaction after addition of FeCp₂BF₄ (black) in DMF:THF at -60 °C.111

Figure 5-15. (A1) Electronic absorption spectra of the putative [Fe^{II}Hpoat(PGA)]¹⁻ complex (black) and 33 min after addition of 3 equiv. O₂ (black) in DMSO at 20 °C. (A2) Electronic absorption spectra of the same reaction at 100 times higher concentration. (B) EPR spectrum (//-mode, 10.4 K, DMSO) of 33 min after addition of 3 equiv. O₂ to the putative [Fe^{II}Hpoat(PGA)]⁻ complex.112

List of Schemes

Scheme 2-1. Thermodynamic square schemes for (A) M–oxido complexes and (B) substrates with C–H bonds.	14
Scheme 2-2. (A) $[\text{Mn}^{\text{III}}\text{H}_3\text{buea}(\text{O})]^{2-}$ complex. (B) $[\text{Mn}^{\text{III}}\text{H}_3\text{bpuea-R}(\text{O})]^{2-}$ complexes.	15
Scheme 2-3. Design consideration of the $\text{K}_2[\text{Mn}^{\text{III}}\text{H}_3\text{bpuea-R}(\text{O})]$ complexes. R = 5F correspond to when the phenyl ring is pentafluoro substituted.	16
Scheme 2-4. Synthesis of the $\text{K}_2[\text{Mn}^{\text{III}}\text{H}_3\text{bpuea-OMe}(\text{O})]$ complex.	16
Scheme 2-5. Thermodynamic square schemes for the $[\text{Mn}^{\text{III}}(\text{O})\text{-R}]^{2-}$ complexes.	21
Scheme 2-6. Reaction of the $[\text{Mn}^{\text{III}}(\text{O})\text{-R}]^{2-}$ complexes with 9,10-dihydroanthracene.	24
Scheme 2-S1. Synthesis of $\text{H}_6\text{bpuea-R}$ ligand.	33
Scheme 3-1. Synthesis of $\text{K}[\text{Fe}^{\text{II}}\text{poat}]$ and $[\text{Fe}^{\text{III}}\text{poat}]$	41
Scheme 3-2. Synthesis of $\text{K}(\text{crypt})[\text{Fe}^{\text{II}}\text{poat}(\text{NH}_3)]$ and $[\text{Fe}^{\text{III}}\text{poat}(\text{NH}_3)]$	42
Scheme 3-3. Synthesis of $\text{K}[\text{Fe}^{\text{II}}\text{poat}(\text{NHtol})]$	50
Scheme 4-1. Mechanism of TauD (left) and Cytochrome P450 “rebound” (right).	54
Scheme 4-2. Synthesis of $\text{K}[\text{Fe}^{\text{II}}\text{POP}]$ and $\text{K}[\text{Fe}^{\text{II}}\text{POP}(\text{H}_2\text{O})]$	67
Scheme 4-3. Generation of $[\text{Fe}^{\text{IV}}\text{POP}(\text{O})]^-$ using $[\text{Fe}^{\text{II}}\text{POP}]^-$ as the starting complex. Identical UV-vis and EPR results were observed when using $[\text{Fe}^{\text{II}}\text{POP}(\text{H}_2\text{O})]^-$ as the starting complex.	70
Scheme 4-4. Reactivity between $[\text{Fe}^{\text{IV}}\text{POP}(\text{O})]^-$ and benzyl alcohol.	75
Scheme 5-1. Synthesis of $\text{Na}(\text{NMe}_4)[\text{Fe}^{\text{II}}\text{POP}(\text{OAc})]$ and $\text{Na}(\text{NMe}_4)[\text{Fe}^{\text{II}}\text{HPOP}(\text{PhP})]$	100
Scheme 5-2. Proposed intramolecular proton transfer to form the $[\text{Fe}^{\text{II}}\text{HPOP}(\text{PhP})]^{2-}$ complex.	104
Scheme 5-3. Synthesis of putative $[\text{Fe}^{\text{II}}\text{HPOP}(\text{PGA})]^-$ complex.	107

List of Tables

Table 2-1. Selected distances (Å) and angles (°) for $K_2[Mn^{III}H_3bpuea-OMe(O)]$ and $K_2[Mn^{III}H_2bpuea-5F(OH)]$.	19
Table 2-2. Spectroscopic results of the $[Mn^{III}(O)-R]^{2-}$ complexes.	20
Table 2-3. Thermodynamic parameters of the $[Mn^{III}(O)-R]^{2-}$ complexes.	23
Table 2-4. Activation parameters of the $[Mn^{III}(O)-R]^{2-}$ complexes.	24
Table 2-5. KIE of the $[Mn^{III}(O)-R]^{2-}$ complexes.	24
Table 2-6. Second-order rate constant of the $[Mn^{III}(O)-R]^{2-}$ complexes with various substrates.	28
Table 2-S1. Metric parameters for $K_2[Mn^{III}H_3bpuea-OMe(O)] \cdot H_2O \cdot 1.5$ DMA.	32
Table 3-1. Selected distances (Å) and angles (°) for $[Fe^{II/III}poat(NH_3)]^{-/0}$ and analogous Fe complexes with $[MST]^{3-}$ for comparison.	46
Table 3-2. Selected distances (Å) and angles (°) for $K[Fe^{II}poat(NHtol)]$	51
Table 3-S1. Metric parameters for $K(crypt)[Fe^{II}poat(NH_3)]$, $[Fe^{II}poat(NH_3)]$, and $K[Fe^{II}poat(NHtol)]$.	57
Table 4-1. Selected Distances (Å) and angles (°) for $K[Fe^{II}POP(H_2O)]$.	69
Table 4-2. The self-decay k_{obs} (900nm) of $[Fe^{IV}POP(O)]^-$ complex (-20 °C, DMF).	71
Table 4-3. Second order rate constants.	78
Table 4-4. chemical shifts (ppm) for 4-R-benzyl alcohol and the Zn^{II} -aqua complex.	81
Table 4-S1. Metric parameters for $\{K[Fe^{II}POP(H_2O)]\}_2$ and $\{K[Zn^{II}POP(H_2O)]\}_2$.	87
Table 5-1. Selected distances (Å) and angles (°) for $Na(NMe_4)[Fe^{II}POP(OAc)]$ and $Na(NMe_4)[Fe^{II}HPOP(PhP)]$.	103
Table 5-S1. Metric parameters for $\{Na(NMe_4)[Fe^{II}POP(OAc)]\}_2$ and $\{Na(NMe_4)[Fe^{II}HPOP(PhP)]\}_2$.	115

acknowledgement

First, I would like to thank Andy for being incredibly supportive over the past five years. You always encourage me to push myself, to explore possibilities, to be a better scientist. Even though sometimes I lack effective communication or get distracted and fall off the path, you are always there to guide me. I am truly grateful for having such a great scientist and mentor as my advisor.

I would also like to thank my committee members, Professor Alan Heyduk and Professor Jenny Yang, and other UCI inorganic chemistry professors, Professor Bill Evans, Professor Michael Green, and Professor Shane Ardo. When I visited UCI during recruitment in 2016, a graduate student told me I should not choose a university based on one single professor, because researchers will always be interactive with other labs. The welcoming and collaborative atmosphere in this department is why I chose to come to UCI, and I am grateful for having the opportunity to learn from so many talented and knowledgeable professors.

Thank you to Jorg Meyer, who made the crucial cuvettes I have been using for all my kinetic measurements since my first year. Even though you told me how much you hated making them, the cuvettes you made were always perfectly what I asked for.

The facilities in UCI are always exceedingly helpful. I am grateful for having the opportunity to be the x-ray facility fellow and learned not only how to mount crystals and solve structures, but also how to make a good margarita from Joe.

I have had great times in the Borovik lab because of all the great people. When I started in lab, I was lucky to have Justin Lee and Dolores Ross with me to go through all the ups and downs together. Thank you, Justin, for giving me those troublesome half triflate structures that I cannot solve, and thank you, Rosddl, for always cheering me up and making me laugh (and showing me pictures of fluffy ferric).

There is one previous member that I would like to give special thanks to -- Dr. Suman K. Barman. You have helped me in every possible way, answered all my endless questions about kinetics, shared fun times and cool ideas with me. I am also thankful for many talented chemists I worked with and learned from: Victoria, Kelsey, Nate, Jason, Sam, Deb, TMEDA, Lisa, and many who joined after me.

My cohort, Bronte, Jeff, and Tener have also been there since day one. It has been fun to go through these five years with you, and you are all so supportive and kind to me.

Lastly, I would like to thank my family and friends for all their love and support. Dad, thank you for shaping me into an independent and strong person. Grandpa, thank you for raising me and teaching me to be calm and patience. Rainy, we have grown up together and you felt more like my sister than cousin, and I am thankful for having you with me to share our joy and tear. My boyfriend, Zhu, and my two cats Bob and Po, thank you for cheering me up and supporting me, especially during the time I wrote this dissertation.

Curriculum Vitae

Education

- Sep 2016 – June 2021 Inorganic chemistry PhD degree
University of California, Irvine
- Sep 2012 – May 2016 B. A. Chemistry
 B. A. Mathematics-Statistics
Boston University

Publication

Sun, C.; Oswald, V. F.; Hill, E. A.; Ziller, J. W.; Borovik, A. S.*;
“Investigation of Iron–Ammine and Amido Complexes within a C_3 -Symmetrical
Phosphinic Amido Tripodal Ligand”
Dalton Trans. **2021**, Just accepted.

Barman, S. K.; Jones, J. R.*; Sun, C.; Hill, E. A.; Ziller, J. W.; Borovik, A. S.*;
“Regulating the Basicity of Metal–Oxido Complexes with a Single Hydrogen
Bond and Its Effect on C–H Bond Cleavage”
J. Am. Chem. Soc. **2019**, *141*, 11142-11150.

Steele, J. L.; Tahsin, L.i; Sun, C.; Elinburg, J. K.; Kotyk, C. M.; McNeely, J.;
Stoian, S. A.; Dragulescu-Andrasi, A.; Ozarowski, A.; Ozerov, M.; Krzystek, J.;
Telser, J.; Bacon, J. W.; Golen, J. A.; Rheingold, A. L.; Doerrer, L. H.*;
“Square-planar Co(III) in {O₄} coordination: large ZFS and reactivity with ROS”
Chem. Commun. **2018**, *54*, 12045-12048.

Awards and Fellowship

- 2019-present x-ray crystallography fellowship
 University of California, Irvine
- 2015-2016 undergraduate research opportunity program scholarship
 Boston University

Presentations

Sun, C.; Oswald, V. F.; Ziller, J. W.; Borovik, A. S.;

“10 Years of Fe^{IV}(O):from Room-temperature Stable Complex to Cleaving C–H Bond”

Presentation at UCI Student Inorganic Seminar Series, Irvine, CA, Nov. 5th, 2020

Sun, C.; Lee, J. L.; Ross, D. L.; Gomez, F. J.; Goulet, M. E.; Barman, S. K.; Oswald, V. F.; Borovik, A. S.;

“Bioinspired Inorganic Chemistry: Synthetic Models”

Poster at 3rd SoCal Bioinorganic Conference, Los Angeles, CA, Dec. 7th, 2019

Sun, C.; Oswald, V. F.; Ziller, J. W.; Borovik, A. S.;

“Investigation of the binding of nitrogen-based exogenous ligands in iron complexes within a C₃-symmetrical phosphinic amide tripodal ligand”

Presentation at Fall 2019 ACS National Meeting & Exposition, San Diego, CA, Aug. 25-29th, 2019

Sun, C.; Lee, J. L.; Ross, D. L.; Gomez, F. J.; Goulet, M. E.; Kneebone, J. L.; Barman, S. K.; Oswald, V. F.; Borovik, A. S.;

“Bioinspired Inorganic Chemistry: Synthetic Models”

Poster at 2nd SoCal Bioinorganic Conference, Pasadena, CA, Dec. 8th, 2018

Sun, C.; Barman, S. K.; Jones, J. R.; Ziller, J. W.; Borovik, A. S.;

“Effect of a Single Hydrogen Bonding Interaction in Reactivities of Manganese(III) Oxido Complexes”

Poster at 255th ACS National Meeting & Exposition, New Orleans, LA, Mar. 18-22nd, 2018

Oswald, V. F.; **Sun, C.;** Lee, J. L.; Barman, S. K.; Kneebone, J. L.; Weitz, A. C.; Hendrich, M. P.; Borovik, A. S.;

“Bioinspired Inorganic Chemistry: Synthetic Tripodal Models”

Poster at 1st SoCal Bioinorganic Conference, Irvine, CA, Dec. 2th, 2017

Abstract of The Dissertation

Secondary Coordination Sphere Effects on Properties and Reactivities of Metal complexes

By

Chen (Sunny) Sun

Doctor of Philosophy in Chemistry

University of California, Irvine, 2021

Professor A. S. Borovik, Chair

In nature, metalloproteins can perform difficult transformations with high selectivity and efficiency through precise control of the primary and secondary coordination sphere. Synthetic chemists have developed biomimetic ligand scaffolds to better understand the coordination environments in the active sites of metalloproteins. However, besides the ligands covalently bound to the metal center, secondary coordination sphere that is comprised of non-covalent interactions also has significant influence in complex properties. This dissertation describes how modulation of the secondary coordination sphere by incorporating different H-bond donors or acceptors affects the chemistry of metal complexes.

Chapter 2 describes a series of Mn^{III}-oxido complexes within the hybrid tripodal framework, [H₃bpuea-R]³⁻, which one of the ligand arms contains a *para*-substituted phenyl ring. Varying the R-groups on the phenyl ring allowed modulation on the strength of one single H-bond donor in the secondary coordination sphere without perturbing the primary coordination sphere. This modulation showed influences on basicity and reactivity of the Mn^{III}-oxido complexes.

Chapter 3 describes newly synthesized Fe^{II/III}-NH₃ and Fe^{III}-amido complexes in C₃-symmetric tripodal phosphinic amido ligand framework, [poat]³⁻. Comparing the Fe^{II/III}-NH₃ complexes in the [poat]³⁻ ligand framework and analogous complexes in [MST]³⁻ ligand framework showed significant differences in their structural and redox properties, suggesting [poat]³⁻ can serve as a stronger donor ligand and provide stronger H-bonding interactions.

Chapter 4 describes the reactivity of a high spin Fe^{IV}-oxido complex, [Fe^{IV}POP(O)]⁻, in C₃-symmetric tripodal phosphoryl amido ligand framework. Taking inspiration from TauD having substrate anchored in close proximity of the metal center, benzyl alcohol was used as a substrate that can participate in possible H-bond interaction with the P=O in phosphoryl amido arms of the complex. Reactivity of [Fe^{IV}POP(O)]⁻ with benzyl alcohol was observed. Hammett analysis and determination of kinetic isotope effect (KIE) for the reactions were performed. The KIE values suggest the cleavage of the C–H bond is involved in the rate determining step whereas the cleavage of the O–H bond is not. Furthermore, the reaction rate of the [Fe^{IV}POP(O)]⁻ complex with benzyl alcohol was ~100 times larger than that of the [Fe^{IV}poat(O)]⁻ complex. This result showed two complexes in similar primary coordination sphere can have significantly different reactivities by modification of the secondary coordination sphere around the Fe^{IV}-oxido moiety.

In chapter 5, extending the study of the C₃-symmetric tripodal phosphoryl amido ligand framework, [POP]³⁻, binding of α -keto acids such as sodium phenylpyruvate (NaPhP) and phenylglyoxylic acid (PGA) were studied as exogenous ligand for iron complex. The Na(NMe₄)[Fe^{II}HPOP(PhP)] complex was isolated and characterized. Intramolecular tautomerization was observed in the Fe^{II}-PhP complex with the [PhP]²⁻ ligand bound as enolate form and one of the phosphoryl amide arms protonated. Preliminary UV-vis and EPR results for reactivities of the α -keto acids bound iron complexes with O₂ showed possible oxidation of the iron center

Chapter 1 – Introduction

Biological Inspiration

Metalloproteins are known to perform a variety of chemical transformations with efficiency and selectivity.^{1–8} Precise control of the micro-environment in the active site of metalloproteins is a key factor in regulating function.^{9–11} The property and function of the enzyme are governed by the primary coordination sphere (ligands covalently bound to the metal ions in the active site) and the secondary coordination sphere (non-covalent interactions surrounding the active site). The primary coordination sphere has important influences in enzyme properties such as stability and reactivity. However, it has been found that covalent interactions alone are not sufficient to facilitate catalytic reactivities.^{12,13} The secondary coordination sphere is mostly comprised of hydrogen bonds (H-bonds), steric interactions, and electrostatic interactions that serve various purposes such as stabilizing reactive intermediates, participating in proton and electron transfer, and orienting substrates in close proximity.^{14–22} There are various examples that demonstrates the importance of local environment in the enzyme active site (Figure 1-1).^{23–26}

For instance, the oxygen evolving complex (OEC) of photosystem II is a {Mn₄CaO₅} cluster that can oxidize two water molecules to form dioxygen through a process involving four protons and four electrons.^{23,27,28} The cluster is anchored by several amino acid residues that define the primary coordination sphere and surrounded by intricate arrangement of H-bonds within secondary coordination sphere (Figure 1-1A). The primary coordination sphere is highly anionic, and therefore likely to stabilize high oxidation states of Mn required for O₂ production;^{29–31} the H-bonding network serves as a pathway for transferring protons and electrons and transporting substrate water molecules.^{23,32} It has been found that disruption of this H-bonding network by site-directed mutagenesis deactivate the enzyme and hinders O₂ production.^{33,34}

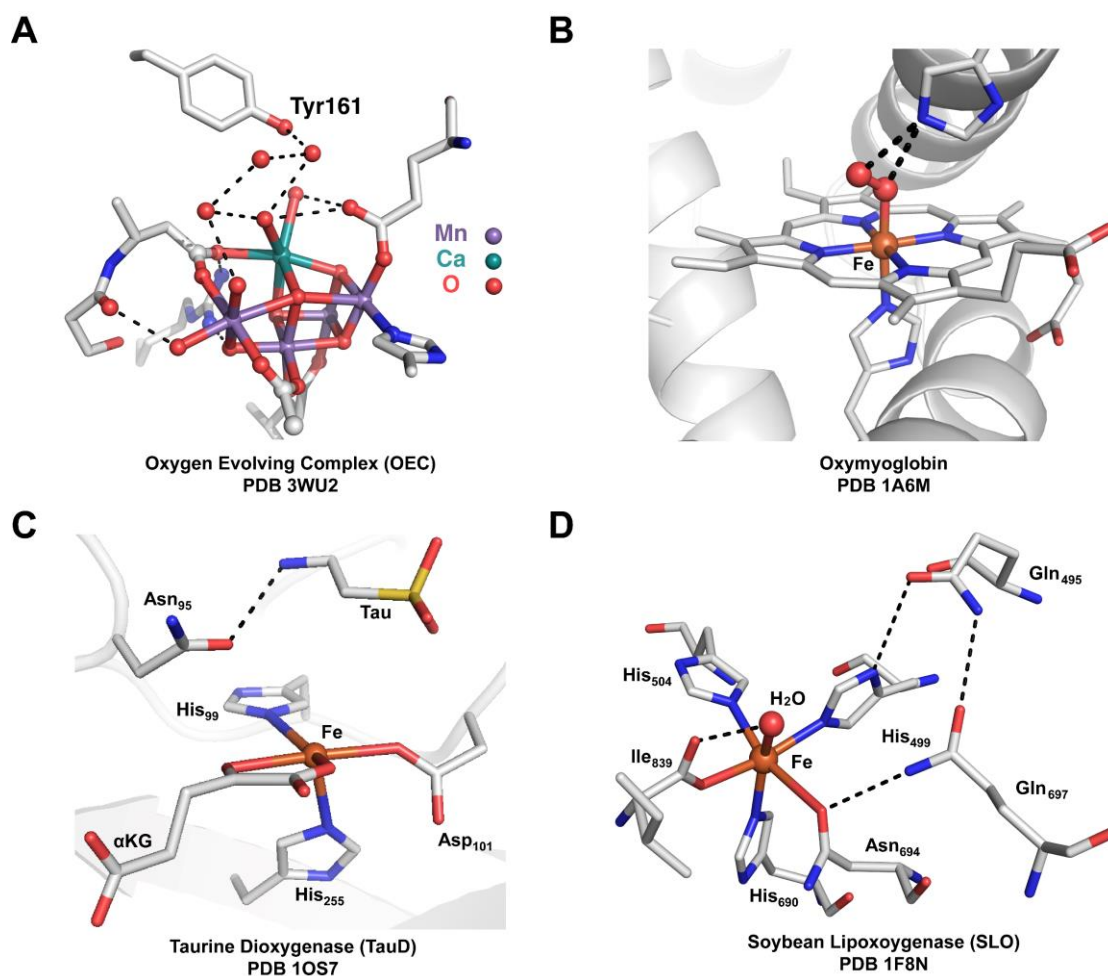


Figure 1-1. (A) The active site in the OEC (PDB:3WU2), illustrating the $\{Mn_4CaO_5\}$ cluster and H-bonding network. (B) The active site in the oxymyoglobin (PDB: 1A6M), illustrating the iron heme center and H-bonding to the O_2 ligand. (C) The active site in the TauD (PDB: 1OS7), illustrating the resting state of the iron center with taurine anchored in close proximity by H-bonding interaction. (D) The active site in the SLO (PDB: 1F8N). All H-bonding interactions are highlighted with black dashed lines.

Further illustration of importance of H-bonding network can be found in active site of iron heme proteins, myoglobin (Mb) and hemoglobin (Hb). Mb and Hb are respiratory proteins that can transfer O_2 via reversible binding to the Fe center to generate an Fe- O_2 adduct stabilized by H-bonding interaction (ex. Figure 1-1B).^{24,35} Extensive studies on synthetic iron porphyrin complexes have shown that without the H-bonding interactions or steric restraints, the complex irreversibly bind O_2 and form μ -oxo bridged dimers.^{36–38}

Synthetic Systems

Achieving the precise control of both primary and secondary coordination spheres demonstrated by enzyme active site in a synthetic metal complex is challenging. Many synthetic groups have designed different systems to tune the properties of the ligands covalently bound to the metal centers. However, extending this control beyond the primary sphere to weak, non-covalent interactions in the local environment around the metal center has proved to be difficult. One strategy that has been used to overcome this challenge in synthetic systems is using appended functional groups that can promote intramolecular H-bonds in a rigid ligand scaffold.

One of the earliest examples of synthetic systems incorporating ligand design to modulate the local environment around metal complexes was introduced by Collman.³⁹⁻⁴² As introduced before, there have been examples of synthetic iron porphyrin complexes that mimic the Mb and Hb active site, but unless under low temperature conditions, these complexes irreversibly bind O₂ and form μ -oxo bridged dimers.⁴³⁻⁴⁷ To circumvent this problem, Collman developed a substituted “picket fence” porphyrin with appended pivalamide groups that can serve as H-bond donor (Figure 1-2A). Although these amide NH groups were later found to be too far away from the Fe-O₂ unit to participate in H-bonding interaction (>5 Å), they did increase the steric bulk and form a “fence” around the Fe-O₂ moiety to prevent dimerization and allowed Collman to characterize the complex at ambient temperature. Further modification of the “picket fence” framework with an appended phenyl urea substituent to incorporate H-bond donor in closer proximity was studied (Figure 1-2B). Increase in the complex binding affinity for O₂ was found, which was proposed to be attributed to the H-bonding interaction between the NH_{urea} and O₂ unit.

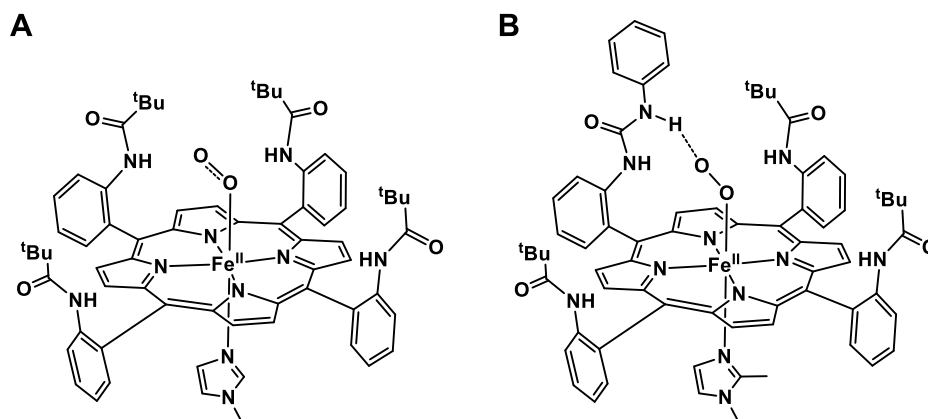


Figure 1-2. (A) Structurally characterized picket fence porphyrin complex supporting an Fe–O₂ adduct. (B) Modified picket fence porphyrin complex containing a urea group capable of H-bonding.

More recently, systems developed by Fout and Szymczak groups also illustrated the importance of local environment around the metal complexes. The Fout group characterized a series of Fe^{II}-OH complexes with different X-groups to modulate the donor strength of primary coordination sphere, and R-groups to modulate the H-bonding interactions of secondary coordination sphere (Figure 1-3A).⁴⁸ By varying these two factors, the complexes of this series were found to have Fe^{III/II}-OH redox events that span over a 400 mV range. The Szymczak group used a tripodal H-bond donor containing system that can capture and reduce dioxygen to form peroxo bridged dimers, and further study of the Zn^{II} complex showed the capture of dioxygen is reversible (Figure 1-3B).^{49,50} When an analogous system that does not contain H-bond donors was investigated, demetallation was observed instead of O₂ capture.

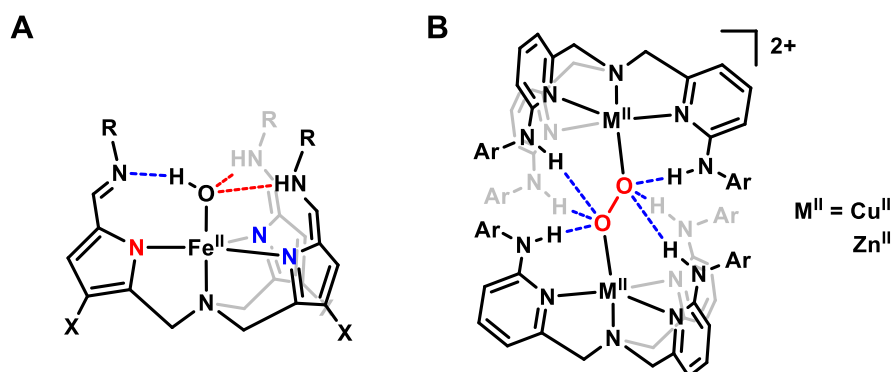


Figure 1-3. (A) Fe^{II}-OH complexes isolated by the Fout group (B) Dizinc peroxide complex isolated by the Szymczak group.

Previous Work in The Borovik Lab

The Borovik lab specializes at ligand designs that incorporates H-bonding interaction into C_3 -tripodal frameworks to achieve precise control of the local environment around the metal center. Various types of C_3 -tripodal frameworks have been developed in the Borovik lab with different design purposes (Figure 1-4).^{3,8,12,51-54}

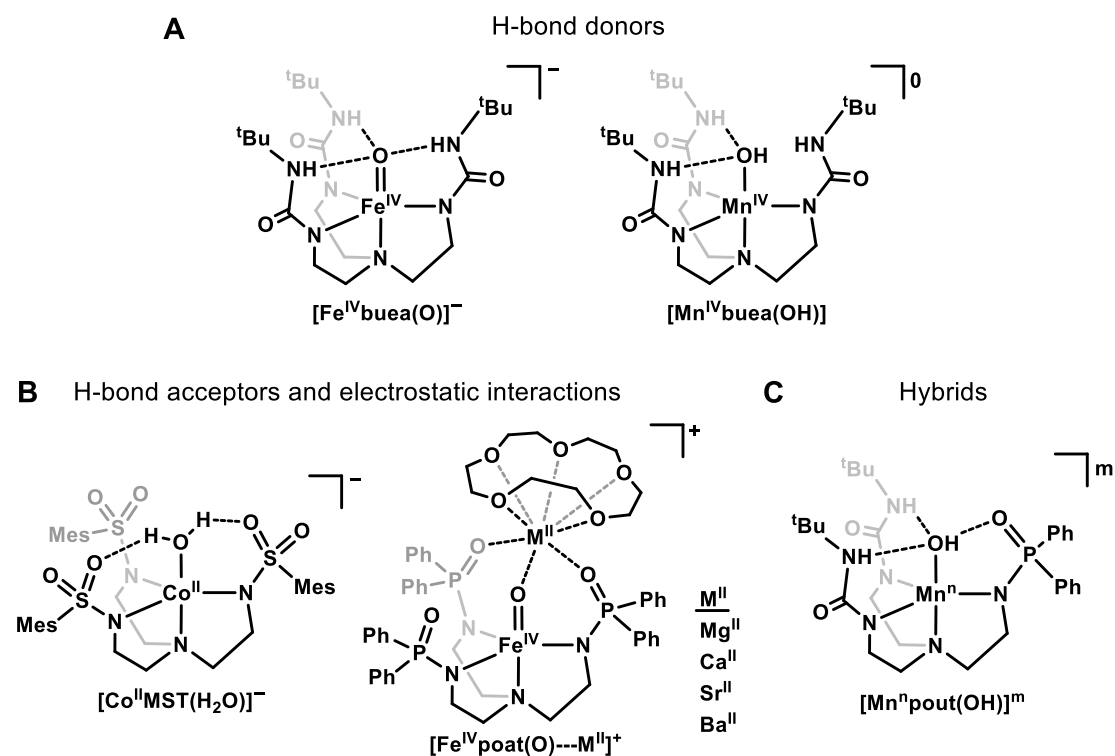


Figure 1-4. Complexes in various C_3 -tripodal frameworks designed by the Borovik lab.

For instance, the C_3 -symmetric tripodal urea ligand, $[\text{H}_3\text{buea}]^{3-}$ contains three H-bond donors positioned to stabilize metal-oxido complexes (Figure 1-4A). This stabilization allowed isolation of the first examples of crystallographically characterized terminal Mn^{III} -oxido and Fe^{III} -oxido complexes.⁵⁵⁻⁵⁸ Moreover, several monomeric Mn, Co, and Fe complexes at different oxidation states with terminal oxido and hydroxido ligands in this framework were successfully isolated and characterized.⁵⁵⁻⁶¹ In contrast, the C_3 -symmetric tripodal sulfonamido and phosphinic amido ligands, $[\text{MST}]^{3-}$ and

[poat]³⁻, contain S=O and P=O groups that can serve as H-bond acceptors as well as participate in electrostatic interactions (Figure 1-4B). These ligand frameworks afforded the characterization of several asymmetric heterobimetallic complexes with transition metals in the tripodal ligand and Group II metal ions interacting with oxygen atoms of the tripodal ligand.^{52,53,62} Furthermore, hybrid tripodal frameworks have been designed for more specific control of the H-bonding network in the complexes (Figure 1-4C).^{63,64}

Overview of remaining chapters

The research described in this dissertation focuses on the effect of both the primary and secondary coordination sphere on complex properties and reactivities. Complexes in three different tripodal frameworks that are each designed to utilize specific purposes will be discussed.

Chapter 2 describes a collaborative project that demonstrates fine-tuning of a single H-bonding interaction can modulate basicity and reactivities of a series of Mn^{III}-oxido complexes. The hybrid tripodal framework, [H₃bpuea-R]³⁻, contains a modification from the [H₃buea]³⁻ ligand where the *tert*-butyl groups on one of the urea arms is replaced with a *para*-substituted phenyl ring (Figure 1-5). This modification allows installment of various R-groups to tune the strength of one single H-bond donor in the secondary coordination sphere without perturbing the primary coordination sphere. Series of Mn^{III}-oxido complexes and their analogous Mn^{II}-hydroxido complexes in this ligand frameworks were synthesized and characterize for investigation of their thermodynamic parameters. The resulted p*K*_a(O–H) values of the Mn^{III} complexes showed a trend based on Hammett analysis, and the determined second order rate constants of these complex for reaction with 9,10-dihydroanthracene (DHA) showed a direct correlation between the basicity and reactivity of the complexes.

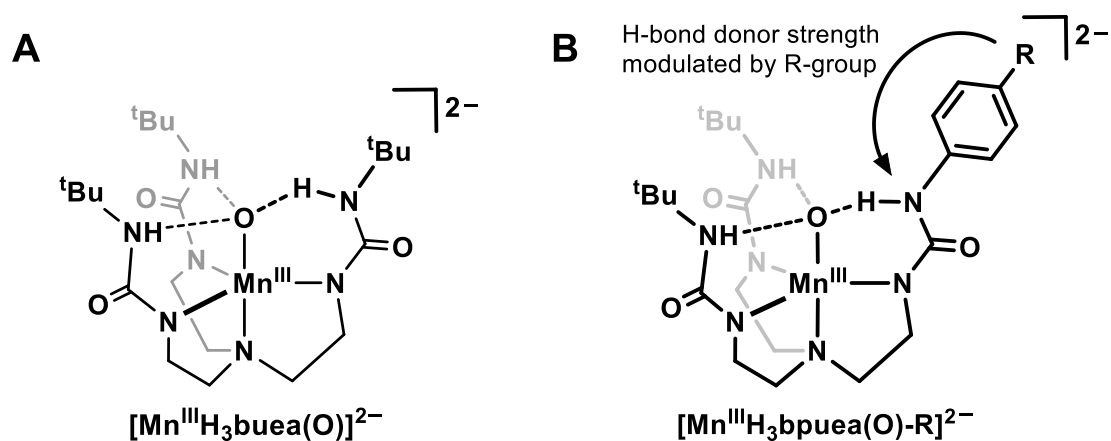


Figure 1-5. (A) $[\text{Mn}^{\text{III}}\text{H}_3\text{buea}(\text{O})]^{2-}$ complex. (B) $[\text{Mn}^{\text{III}}\text{H}_3\text{bpuea}-\text{R}(\text{O})]^{2-}$ complexes.

Chapter 3 describes newly synthesized $\text{Fe}^{\text{II/III}}-\text{NH}_3$ and Fe^{III} -amido complexes in C_3 -symmetric tripodal phosphinic amido ligand framework, $[\text{poat}]^{3-}$, and their comparison with analogous complexes in previous C_3 -symmetric tripodal sulfonamido ligand framework, $[\text{MST}]^{3-}$ (Figure 1-6). The phosphinic amido functional groups in $[\text{poat}]^{3-}$ are expected to serve as stronger donating ligands as well as better H-bond acceptors compare to sulfonamido groups. The comparisons between the $\text{Fe}^{\text{II/III}}-\text{NH}_3$ complexes in the $[\text{poat}]^{3-}$ and $[\text{MST}]^{3-}$ ligand frameworks showed significant differences in their structural and redox properties. These comparisons clearly demonstrated the significant impact on complex properties by both primary coordination sphere (strength of ligand field) and secondary coordination sphere (strength of H-bonds).

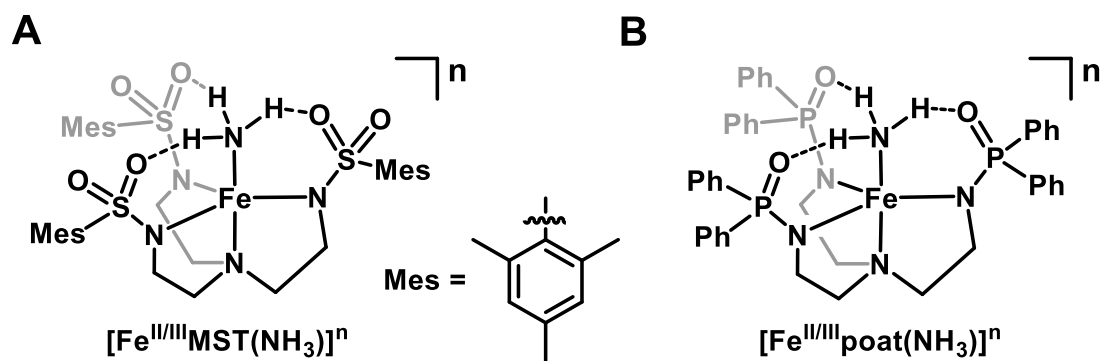


Figure 1-6. $\text{Fe}^{\text{II/III}}-\text{NH}_3$ complexes in the (A) $[\text{MST}]^{3-}$ and (B) $[\text{poat}]^{3-}$ ligand framework.

Chapter 4 describes the reactivity of a high spin Fe^{IV}-oxido complex, [Fe^{IV}POP(O)]⁻, in a C₃-symmetric tripodal phosphoryl amido ligand framework (Figure 1-7). In nature, a high spin Fe^{IV}-oxido moiety has been identified as the key intermediate in enzyme active sites responsible for cleaving strong C–H bonds.^{65–68} Several previously characterized high spin Fe^{IV}-oxido complexes by the Borovik lab such as [Fe^{IV}H₃buea(O)]⁻ and [Fe^{IV}poat(O)]⁻ did not show expected reactivity toward substrates (Figure 1-7). Therefore, the [POP]³⁻ ligand framework was investigated because it is proposed to have less steric hindering of the Fe^{IV}-oxido moiety that may promote reactivity of the complex.

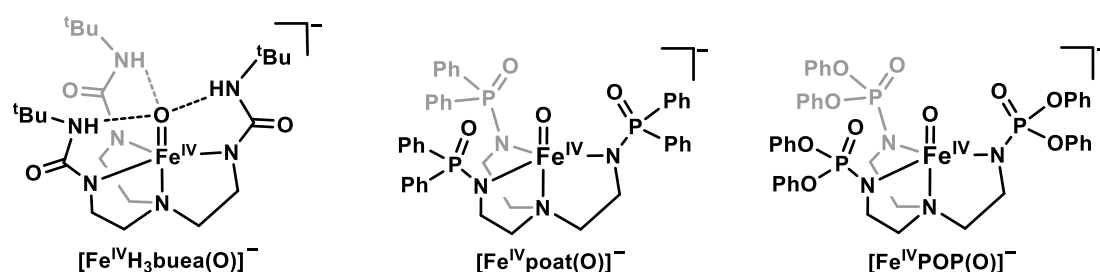


Figure 1-7. Fe^{IV}-oxido complexes in C₃-symmetric tripodal ligand framework.

Initial reactivity studies using various hydrocarbons did not show observable reactivity. Taking inspiration from TauD having substrates anchored in close proximity of the metal center (Figure 1-1C), benzyl alcohol was used as a substrate that could H-bond interact with the P=O in phosphoryl amido arms and reactivity was observed. Series of *para*-substituted benzyl alcohols were used, and a Hammett analysis of the reactions was obtained. Further understanding of the reaction mechanism was performed by determination of kinetic isotope effect (KIE) via two separate reactions: (1) KIE = 15 using α,α -d₂-benzyl alcohol that was deuterated at the benzylic carbon position, and (2) KIE = 1 using d₁-benzyl alcohol that was deuterated at the O–H position. These KIE values suggest the cleavage of the C–H bond is involved in the rate determining step whereas the cleavage of the O–H bond is not. Most importantly, the second order rate constant for the reaction of the [Fe^{IV}POP(O)]⁻

complex with benzyl alcohol was 100 times larger than that of the $[\text{Fe}^{\text{IV}}\text{poat}(\text{O})]^-$ complex. This result showed two complexes in extremely similar primary coordination sphere can have significantly different reactivities by modification of the local environment around the Fe^{IV} -oxido moiety.

Chapter 5 extends the study of the C_3 -symmetric tripodal phosphoryl amido ligand framework, $[\text{POP}]^{3-}$, on binding of α -keto acids such as sodium phenylpyruvate (NaPhP) and phenylglyoxylic acid (PGA) were studied as exogenous ligand for iron complex. A $\text{Na}(\text{NMe}_4)[\text{Fe}^{\text{II}}\text{POP}(\text{OAc})]$ salt was first synthesized and characterized as synthon. Addition of NaPhP to the acetate complex led to the isolation of a structurally characterized $\text{Na}(\text{NMe}_4)[\text{Fe}^{\text{II}}\text{HPOP}(\text{PhP})]$ salt. Intramolecular tautomerization was observed in the Fe^{II} -PhP complex with the $[\text{PhP}]^{2-}$ ligand bound as enolate form and one of the phosphoryl amide arms protonated (Figure 1-8). Preliminary UV-vis and EPR results for reactivities of the α -keto acids bound iron complexes with O_2 showed possible oxidation of the iron center, but further experiments are still needed to conclude the identity of the product.

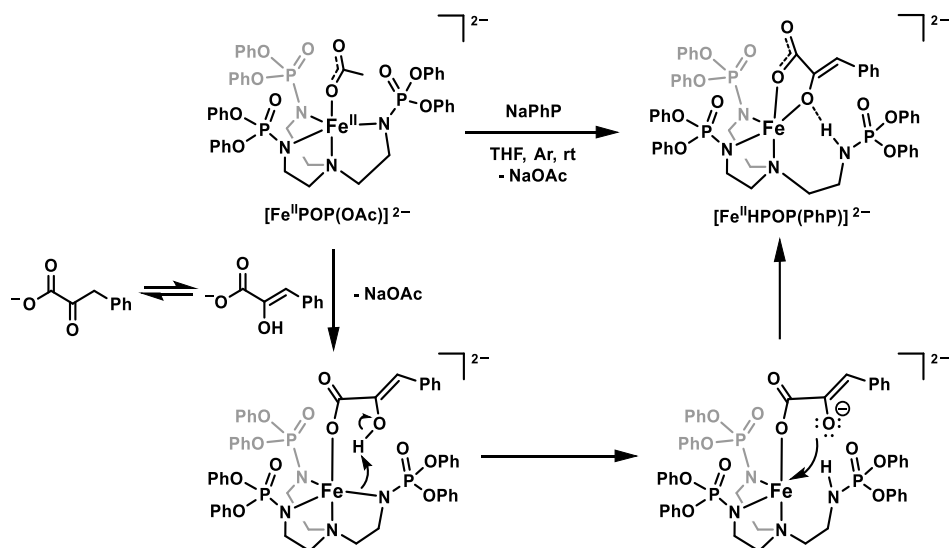


Figure 1-8. Proposed intramolecular proton transfer to form the $[\text{Fe}^{\text{II}}\text{HPOP}(\text{PhP})]^{2-}$ complex.

References

- (1) Poulos, T. L. *Chem. Rev.* **2014**, *114* (7), 3919–3962.
- (2) Tommos, C.; Babcock, G. T. *Acc. Chem. Res.* **1998**, *31* (1), 18–25.
- (3) Stone, K. L.; Borovik, A. S. *Curr. Opin. Chem. Biol.* **2009**, *13*, 114–118.
- (4) Que, L. J.; Tolman, W. B. *Nature* **2008**, *455*, 333–340.
- (5) Holm, R. H.; Kennepohl, P.; Solomon, E. I. *Chem. Rev.* **1996**, *96* (7), 2239–2314.
- (6) Liu, J.; Chakraborty, S.; Hosseinzadeh, P.; Yu, Y.; Tian, S.; Petrik, I.; Bhagi, A.; Lu, Y. *Chem. Rev.* **2014**, *114* (8), 4366–4369.
- (7) Borovik, A. S. *Chem. Soc. Rev.* **2011**, *40* (4), 1870–1874.
- (8) Cook, S. A.; Hill, E. A.; Borovik, A. S. *Biochemistry* **2015**, *54* (27), 4167–4180.
- (9) Solomon, E. I.; Light, K. M.; Liu, L. V.; Srnec, M.; Wong, S. D. *Acc. Chem. Res.* **2013**, *46* (11), 2725–2739.
- (10) Que, L. J.; Ho, R. Y. N. *Chem. Rev.* **1996**, *96* (7), 2607–2624.
- (11) Dawson, J. H. *Science (80-.)*. **1988**, *240* (4851), 433–439.
- (12) Borovik, A. S. *Acc. Chem. Res.* **2005**, *38* (1), 54–61.
- (13) Shook, R. L.; Borovik, A. S. *Inorg. Chem.* **2010**, *49* (8), 3646–3660.
- (14) Shaw, W. J. *Catal. Rev. - Sci. Eng.* **2012**, *54* (4), 489–550.
- (15) Walsh, A. P.; Laureanti, J. A.; Katipamula, S.; Chambers, G. M.; Priyadarshani, N.; Lense, S.; Bays, J. T.; Linehan, J. C.; Shaw, W. J. *Faraday Discuss.* **2019**, *215*, 123–140.
- (16) Costas, M.; Mehn, M. P.; Jensen, M. P.; Que, L. *Chem. Rev.* **2004**, *104* (2), 939–986.
- (17) Casadei, C. M.; Gumiero, A.; Metcalfe, C. L.; Murphy, E. J.; Basran, J.; Concilio, M. G.; Teixeira, S. C. M.; Schrader, T. E.; Fielding, A. J.; Ostermann, A.; Blakeley, M. P.; Raven, E. L.; Moody, P. C. E. *Science (80-.)*. **2014**, *345* (6193), 193–197.
- (18) Berggren, G.; Adamska, A.; Lambertz, C.; Simmons, T. R.; Esselborn, J.; Atta, M.; Gambarelli, S.; J-M., M.; Reijerse, E.; Lubitz, W.; Happe, T.; Artero, V.; Fontecave, M. *Nature* **2013**, *499*, 66–69.
- (19) Blasiak, L. C.; Vailancourt, F. H.; Walsh, C. T.; Drennan, C. L. *Nature* **2006**, *440*, 368–371.
- (20) Groves, J. T. *J. Inorg. Biochem.* **2006**, *100* (4), 434–447.
- (21) Ono, T. A.; Rompel, A.; Mino, H.; Chiba, N. *Biophys. J.* **2001**, *81* (4), 1831–1840.
- (22) Boussac, A.; Rappaport, F.; Carrier, P.; Verbavatz, J. M.; Gobin, R.; Kirilovsky, D.; Rutherford, A. W.; Sugiura, M. *J. Biol. Chem.* **2004**, *279* (22), 22809–22819.
- (23) Umena, Y.; Kawakami, K.; Shen, J.-R.; Kamiya, N. *Nature* **2011**, *473*, 55–60.
- (24) Vojtěchovský, J.; Chu, K.; Berendzen, J.; Sweet, R. M.; Schlichting, I. *Biophys. J.* **1999**, *77* (4), 2153–2174.
- (25) O'Brien, J. R.; Schuller, D. J.; Yang, V. S.; Dillard, B. D.; Lanzilotta, W. N. *Biochemistry* **2003**, *42* (19), 5547–5554.
- (26) Tomchick, D. R.; Phan, P.; Cymborowski, M.; Minor, W.; Holman, T. R. *Biochemistry* **2001**, *40* (25), 7509–7517.
- (27) Siegbahn, P. E. M. *Acc. Chem. Res.* **2009**, *42* (12), 1871–1880.
- (28) Yano, J.; Yachandra, V. *Chem. Rev.* **2014**, *114* (8), 4175–4205.
- (29) Cox, N.; Pantazis, D. A.; Neese, F.; Lubitz, W. *Acc. Chem. Res.* **2013**, *46* (7), 1588–1596.

- (30) Yano, J.; Walker, L. M.; Strickler, M. A.; Service, R. J.; Yachandra, V. K.; Debus, R. J. *J. Biol. Chem.* **2011**, *286* (11), 9257–9267.
- (31) Stich, T. A.; Yeagle, G. J.; Service, R. J.; Debus, R. J.; Britt, R. D. *Biochemistry* **2011**, *50* (34), 7390–7404.
- (32) Vogt, L.; Vinyard, D. J.; Khan, S.; Brudvig, G. W. *Curr. Opin. Chem. Biol.* **2015**, *25* (1), 152–158.
- (33) Oyala, P. H.; Stich, T. A.; Debus, R. J.; Britt, R. D. *J. Am. Chem. Soc.* **2015**, *137* (27), 8829–8837.
- (34) Navarro, M. P.; Ames, W. M.; Nilsson, H.; Lohmiller, T.; Pantazis, D. A.; Rapatskiy, L.; Nowaczyk, M. M.; Neese, F.; Boussac, A.; Messinger, J.; Lubitz, W.; Cox, N. *Proc. Natl. Acad. Sci. U. S. A.* **2013**, *110* (39), 15561–15566.
- (35) Paoli, M.; Liddington, R.; Tame, J.; Wilkinson, A.; Dodson, G. *J. Mol. Biol.* **1996**, *256* (4), 775–792.
- (36) Cohen, I. A.; Caughey, W. S. *Biochemistry* **1966**, *7* (2), 636–641.
- (37) Hoffman, A. B.; Collins, D. M.; Day, V. W.; Fleischer, E. B.; Srivastava, T. S.; Hoard, J. L. *J. Am. Chem. Soc.* **1972**, *94* (10), 3620–3626.
- (38) Shikama, K. *Coord. Chem. Rev.* **1988**, *83* (C), 73–91.
- (39) Collman, J. P.; Reed, C. A. *J. Am. Chem. Soc.* **1973**, *95* (6), 2048–2049.
- (40) Collman, J. P.; Gagne, R. R.; Reed, C. A.; Robinson, W. T.; Rodley, G. A. *Proc. Natl. Acad. Sci. U. S. A.* **1974**, *71* (4), 1326–1329.
- (41) Collman, J. P.; Brauman, J. I.; Doxsee, K. M.; Halbert, T. R.; Suslick, K. S. *Proc. Natl. Acad. Sci. U. S. A.* **1978**, *75* (2), 564–568.
- (42) Collman, J. P.; Gagné, R. R.; Reed, C. A. *J. Am. Chem. Soc.* **1974**, *96* (8), 2629–2631.
- (43) Anderson, D. L.; Weschler, C. J.; Basolo, F. *J. Am. Chem. Soc.* **1974**, *96* (17), 5599–5600.
- (44) Basolo, F.; Hoffman, B. M.; Ibers, J. A. *Acc. Chem. Res.* **1975**, *8* (11), 384–392.
- (45) Baldwin, J. E.; Huff, J. *J. Am. Chem. Soc.* **1973**, *95* (17), 5757–5759.
- (46) Wagner, G. C.; Kassner, R. J. *J. Am. Chem. Soc.* **1974**, *96* (17), 5593–5595.
- (47) Fleischer, E. B.; Srivastava, T. S. *J. Am. Chem. Soc.* **1969**, *91* (9), 2403–2405.
- (48) Gordon, Z.; Drummond, M. J.; Matson, E. M.; Bogart, J. A.; Schelter, E. J.; Lord, R. L.; Fout, A. R. *Inorg. Chem.* **2017**, *56* (9), 4852–4863.
- (49) Dahl, E. W.; Kiernicki, J. J.; Zeller, M.; Szymczak, N. K. *J. Am. Chem. Soc.* **2018**, *140* (32), 10075–10079.
- (50) Dong, H. T.; Szymczak, N. K. *Chem. Commun.* **2018**, *54*, 892–895.
- (51) Taguchi, T.; Stone, K. L.; Gupta, R.; Kaiser-Lassalle, B.; Yano, J.; Hendrich, M. P.; Borovik, A. S. *Chem. Sci.* **2014**, *5* (8), 3064–3071.
- (52) Lacy, D. C.; Park, Y. J.; Ziller, J. W.; Yano, J.; Borovik, A. S. *J. Am. Chem. Soc.* **2012**, *134* (Chart 1), 17526–17535.
- (53) Oswald, V. F.; Lee, J. L.; Biswas, S.; Weitz, A. C.; Mittra, K.; Fan, R.; Li, J.; Zhao, J.; Hu, M. Y.; Alp, E. E.; Bominaar, E. L.; Guo, Y.; Green, M. T.; Hendrich, M. P.; Borovik, A. S. *J. Am. Chem. Soc.* **2020**, *142* (27), 11804–11817.
- (54) Weitz, A. C.; Hill, E. A.; Oswald, V. F.; Bominaar, E. L.; Borovik, A. S.; Hendrich, M. P.; Guo, Y. *Angew. Chemie - Int. Ed.* **2018**, *57* (49), 16010–16014.
- (55) Lacy, D. C.; Gupta, R.; Stone, K. L.; Greaves, J.; Ziller, J. W.; Hendrich, M. P.; Borovik,

- A. S. *J. Am. Chem. Soc.* **2010**, *132* (35), 12188–12190.
- (56) MacBeth, C. E.; Golombek, A. P.; Young, J.; Yang, C.; Kuczera, K.; Hendrich, M. P.; Borovik, A. S. *Science* (80-). **2000**, *289* (5481), 938–941.
- (57) Gupta, R.; Taguchi, T.; Lassalle-Kaiser, B.; Bominaar, E. L.; Yano, J.; Hendrich, M. P.; Borovik, A. S. *Proc. Natl. Acad. Sci. U. S. A.* **2015**, *112* (17), 5319–5324.
- (58) Shirin, Z.; Young, V. G.; Borovik, A. S. **1997**, *036* (1), 1967–1968.
- (59) Gupta, R.; MacBeth, C. E.; Young, V. G.; Borovik, A. S. *J. Am. Chem. Soc.* **2002**, *124* (7), 1136–1137.
- (60) MacBeth, C. E.; Gupta, R.; Mitchell-Koch, K. R.; Young, V. G.; Lushington, G. H.; Thompson, W. H.; Hendrich, M. P.; Borovik, A. S. *J. Am. Chem. Soc.* **2004**, *126* (8), 2556–2567.
- (61) Shook, R. L.; Borovik, A. S. *Chem. Commun.* **2008**, No. 46, 6095–6107.
- (62) Park, Y. J.; Cook, S. A.; Sickerman, N. S.; Sano, Y.; Ziller, J. W.; Borovik, A. S. *Chem. Sci.* **2013**, *4* (2), 717–726.
- (63) Oswald, V. F.; Weitz, A. C.; Biswas, S.; Ziller, J. W.; Hendrich, M. P.; Borovik, A. S. *Inorg. Chem.* **2018**, *57* (21), 13341–13350.
- (64) Barman, S. K.; Jones, J. R.; Sun, C.; Hill, E. A.; Ziller, J. W.; Borovik, A. S. *J. Am. Chem. Soc.* **2019**, *141* (28), 11142–11150.
- (65) Decker, A.; Clay, M. D.; Solomon, E. I. *J. Inorg. Biochem.* **2006**, *100* (4), 697–706.
- (66) Price, J. C.; Barr, E. W.; Tirupati, B.; Bollinger, J. M.; Krebs, C. *Biochemistry* **2003**, *43* (4), 1134.
- (67) Krebs, C.; Galonić Fujimori, D.; Walsh, C. T.; Bollinger, J. M. *Acc. Chem. Res.* **2007**, *40* (7), 484–492.
- (68) Fujimori, D. G.; Barr, E. W.; Matthews, M. L.; Koch, G. M.; Yonce, J. R.; Walsh, C. T.; Bollinger, J. M.; Krebs, C.; Riggs-Gelasco, P. J. *J. Am. Chem. Soc.* **2007**, *129* (44), 13408–13409.

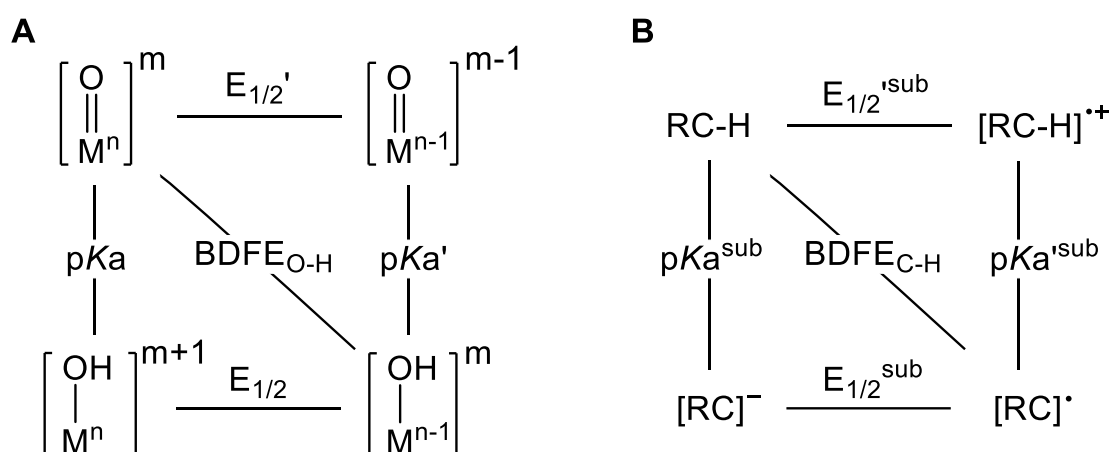
Chapter 2 – Regulating Basicity and Reactivity of Terminal Mn^{III}-oxido Complexes with a Single Hydrogen Bond

Introduction

C–H bond functionalization has numerous applications as an important type of bond transformation. Such synthesis may have large potential because C–H bonds are ubiquitous in organic substances, yet it is one of the most challenging chemical reactions due to the thermodynamic stability of the C–H bonds with relatively large bond dissociation free energies (BDFEs). However, nature has shown powerful capabilities in performing C–H bond functionalization using metalloenzymes with metal-oxido moieties as the key intermediates.^{1–6} For example, cytochrome P450 is a heme enzyme known to activate C–H bonds with BDFEs greater than 100 kcal/mol.^{7–10} However, this raises the question: how can such strongly oxidizing active site functionalize inert C–H bonds without intramolecular oxidative damage of the surrounding moiety?^{11,12} Although the oxidative strength of a compound is often discussed regarding the redox potential, it is not the only parameter that needs to be considered. One important property of P450 enzyme is that the ferryl forms of P450 are surprisingly basic, and Green has suggested that the role of thiolate ligand and its effect on pK_a of Fe^{IV}=O unit is important in C–H bond activation.^{9,10,12}

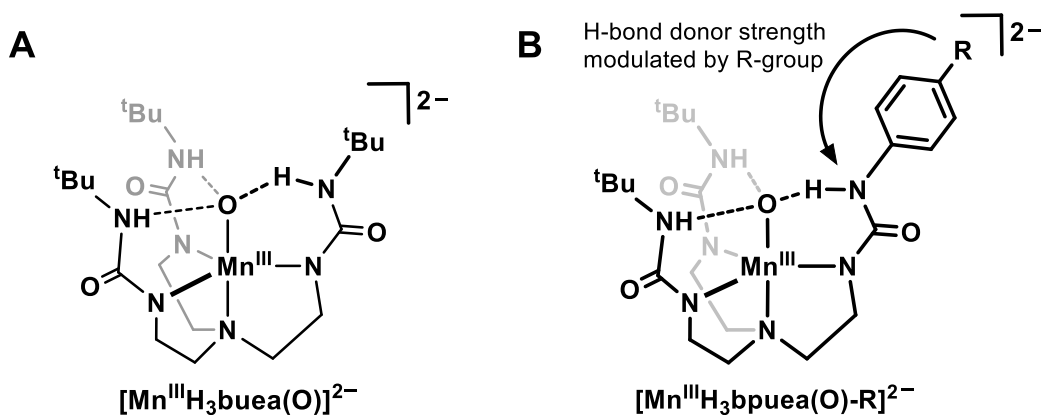
Based on the Bell-Evans-Polanyi principle, ground state thermodynamic analysis of metal oxido complexes shows that BDFE of the O–H bond in metal-hydroxido complexes formed after the C–H bond cleavage is comparable to the energy of the C–H bond cleaved (Scheme 2-1).^{13–16} Three general mechanisms are often used to describe different routes in square scheme: (1) concerted proton–electron transfer (CPET); (2) a two-step electron-transfer/proton-transfer path (ET-PT); and (3) a two-step proton-transfer/electron-transfer path

(PT-ET). The square scheme (Scheme 2-1A) illustrates that redox potentials alone is not always sufficient to describe the reactivity of a metal-oxido complex toward C–H bonds. Basic metal-oxido unit with higher pK_a values for their conjugate acids can have greater $BDFE_{O-H}$ and provide better reactivity at lower potential for C–H bond functionalization. Therefore, tuning basicity of the system may provide significant effects on complex reactivities.



Scheme 2-1. Thermodynamic square schemes for (A) M–oxido complexes and (B) substrates with C–H bonds.

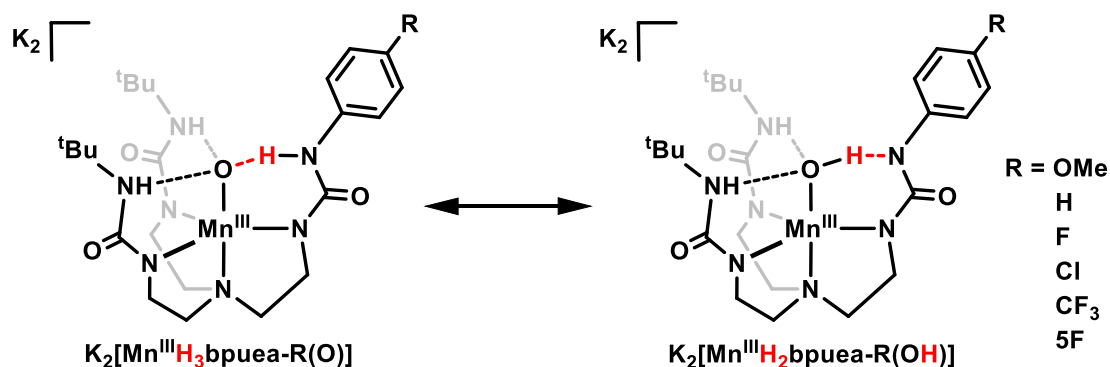
The Borovik group has shown that a well-characterized $[\text{Mn}^{\text{III}}\text{H}_3\text{buea}(\text{O})]^{2-}$ complex can oxidatively cleave C–H bonds in 9,10-dihydroanthracene (DHA) to afford anthracene and $[\text{Mn}^{\text{II}}\text{H}_3\text{buea}(\text{OH})]^{2-}$ (Scheme 2-2A).¹⁷ The $E_{1/2}$ of the $\text{Mn}^{\text{III/II}}(\text{O})$ redox couple was too negative to observe (< -2.0 V vs. $\text{Fc}^{+/0}$). Such negative $E_{1/2}$ is usually associated with reductant. However, high basicity of the $\text{Mn}^{\text{III}}\text{–O}$ complex promoted the capability of this complex to perform C–H bond cleavage. The basic terminal oxido moiety is stabilized by three intramolecular H-bonding interactions from the tripodal ligand, which shows that H-bonding can regulate properties of these types of complexes. To further investigate the effects of H-bonds, precise tuning of the strength of the H-bonds without perturbing the primary coordination sphere around the metal center is required. This motivation led to the design of a new series hybrid ligand $\text{H}_6\text{bpuea-R}$ (Scheme 2-2B).¹⁸



Scheme 2-2. (A) $[Mn^{III}H_3buea(O)]^{2-}$ complex. (B) $[Mn^{III}H_3bpuea(O)-R]^{2-}$ complexes.

Design considerations¹⁸

The design of the complexes relies on modifications within the secondary coordination sphere with minimal changes within the primary coordination sphere. Replacing one of the *tert*-butyl group on urea arm of H_6buea ligand to phenyl ring would allow modulation of a single intramolecular H-bond via substituents effects off the *para*-position of the ring. Using *para*-R-phenyl groups would minimize the effects on the primary coordination sphere because the major changes within the series of complexes would be at the HN_{urea} group, which is not covalently coordinated to the Mn metal center. This more remote HN_{urea} group is, however, involved in forming an intramolecular H-bond; therefore, as the primary coordination sphere around the Mn center remains relatively constant, a change in one H-bond within the secondary coordination sphere would occur that affects the basicity of the oxido ligand. Moreover, as the phenyl ring becomes more electron-withdrawing, the possibility for intramolecular proton transfer can occur to protonate the oxido ligand and afford the species $Mn^{III}-OH\dots-NR$ (Scheme 2-3). This project is a collective effort of Dr. Jason R. Jones, Dr. Suman K. Barman and I. Therefore, this chapter focus on discussion of one of the complexes in this series, $K_2[Mn^{III}H_3bpuea-OMe(O)]$, which was studied by me; the properties and reactivities of it will be compared with other complexes of this series that were prepared and studied by Dr. Jason R. Jones and Dr. Suman K. Barman.

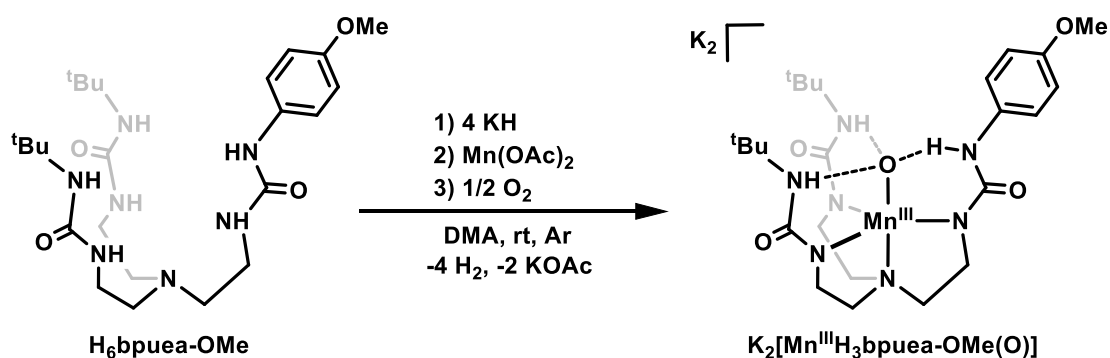


Scheme 2-3. Design consideration of the $K_2[Mn^{III}H_3bpuea-R(O)]$ complexes. R = 5F correspond to when the phenyl ring is pentafluoro substituted.

Result and Discussion

Synthesis of $K_2[Mn^{III}H_3bpuea-OMe(O)]$

The synthesis of the ligand precursor $H_6bpuea-OMe$ and the $K_2[Mn^{III}H_3bpuea-OMe(O)]$ complex followed the reported procedures (Scheme 2-4).¹⁸ $K_2[Mn^{III}H_3bpuea-OMe(O)]$ was synthesized by deprotonating $H_6bpuea-OMe$ with 4 equiv. of KH in dimethylacetamide (DMA) and then solid $Mn^{II}(OAc)_2$ was added to produce a yellow heterogeneous mixture. The mixture was treated with 0.5 eq dry O_2 to produce a dark brown solution, which was layered with Et_2O to yield purple solids. Ligand precursors and complexes with other R substituents are synthesized via same procedure and studied by Dr. Jason R. Jones and Dr. Suman K. Barman. The Mn^{III} -oxido complexes of this series will be referred to as $[Mn^{III}(O)-R]^{2-}$ in future discussions.



Scheme 2-4. Synthesis of the $K_2[Mn^{III}H_3bpuea-OMe(O)]$ complex.

Structural properties of $K_2[Mn^{III}H_3bpuea-OMe(O)]$

The molecular structures of $[Mn^{III}(O)-OMe]^{2-}$ was determined by X-ray diffraction (XRD) methods (Figure 2-1A, Table 2-1) as $K_2[Mn^{III}H_3bpuea-OMe(O)] \cdot H_2O \cdot 1.5 DMA$. XRD analysis revealed that the asymmetric unit of $K_2[Mn^{III}H_3bpuea-OMe(O)] \cdot H_2O \cdot 1.5 DMA$ consists of two independent, but chemically identical $[Mn^{III}(O)-OMe]^{2-}$ anions, with similar metrical parameters (only one of them will be discussed). The complex has N4O donor sets arranged in a trigonal bipyramidal coordination geometry in which the trigonal planes are defined by the three deprotonated ureayl N atoms. The axial coordination sites are occupied by the O1 atom and N1 atom from the tripodal ligands with O1–Mn1–N1 angles of $177.0(1)^\circ$. The structure of $[Mn^{III}(O)-OMe]^{2-}$ provided important structural information for comparison with the molecular structure of the $[Mn^{III}(OH)-5F]^{2-}$ complex obtained by Dr. Jason R. Jones (Figure 2-1B, Table 2-1).

The structure of $[Mn^{III}(O)-OMe]^{2-}$ was determined as a Mn^{III} -oxido complex, whereas the structure of $[Mn^{III}(OH)-5F]^{2-}$ was determined as a Mn^{III} -hydroxido complex with a deprotonated N5 atom of the ligand. Differences were observed in the Mn–O1 bond distances between the two complexes to support that the oxido ligands in these complexes have different protonation states. For instance, the Mn1–O1 bond length of $1.771(3) \text{ \AA}$ in $[Mn^{III}(O)-OMe]^{2-}$ is the same as that found in $[Mn^{III}H_3buea(O)]^{2-}$ ($1.771(5) \text{ \AA}$) and Mn1–O1 bond distance in $[Mn^{III}(OH)-5F]^{2-}$ ($1.819(4) \text{ \AA}$) is significantly longer compared to $[Mn^{III}(O)-OMe]^{2-}$ or $[Mn^{III}H_3buea(O)]^{2-}$. A difference was also found in the Mn1–N1 bond distances, which for $[Mn^{III}(O)-OMe]^{2-}$ is $2.095(4) \text{ \AA}$ and contracts to $2.058(5) \text{ \AA}$ in $[Mn^{III}(OH)-5F]^{2-}$; this change is consistent with an oxido ligand having a stronger trans influence than a hydroxido ligand.¹⁹ Three intramolecular H-bonds involving the O1 atom are also present in the two complexes. In each complex, two N–H \cdots O1 H-bonds are formed with the N6H6 and N7H7 units of the $[H_3bpuea-R]^{3-}$ ligands. However, a noticeable difference was found in the

third H-bond formed with N5 of the phenyl urea. In $[\text{Mn}^{\text{III}}(\text{O})\text{-OMe}]^{2-}$, the O1 atom serves as an H-bond acceptor to produce the $\text{N5-H1}\cdots\text{O1}$, a result that further supports O1 being an oxido ligand. In $[\text{Mn}^{\text{III}}(\text{OH})\text{-5F}]^{2-}$, O1 is protonated and serves as an H-bond donor to form the $\text{N5}\cdots\text{H1-O1}$ H-bond. The H1 atom in $[\text{Mn}^{\text{III}}(\text{O}(\text{H}))\text{-5F}]^{2-}$ was located from a difference-Fourier map and refined to give an O1-H1 bond distance of 0.85 Å. Moreover, the difference-Fourier map showed no residual electron density within bonding distance to N5 to further suggest that it has been deprotonated. We were also able to find H6 and H7 in the difference-Fourier map of $[\text{Mn}^{\text{III}}(\text{OH})\text{-5F}]^{2-}$ and after refinement found N-H bond distances of 0.90 Å for each. These structural data thus support that $[\text{Mn}^{\text{III}}(\text{O})\text{-OMe}]^{2-}$ has a Mn^{III} -oxido unit, while $[\text{Mn}^{\text{III}}(\text{OH})\text{-5F}]^{2-}$ has a Mn^{III} -hydroxido unit that is H-bonded to the deprotonated N5 atom of the ligand $[\text{H}_2\text{bpuea-5F}]^{3-}$.

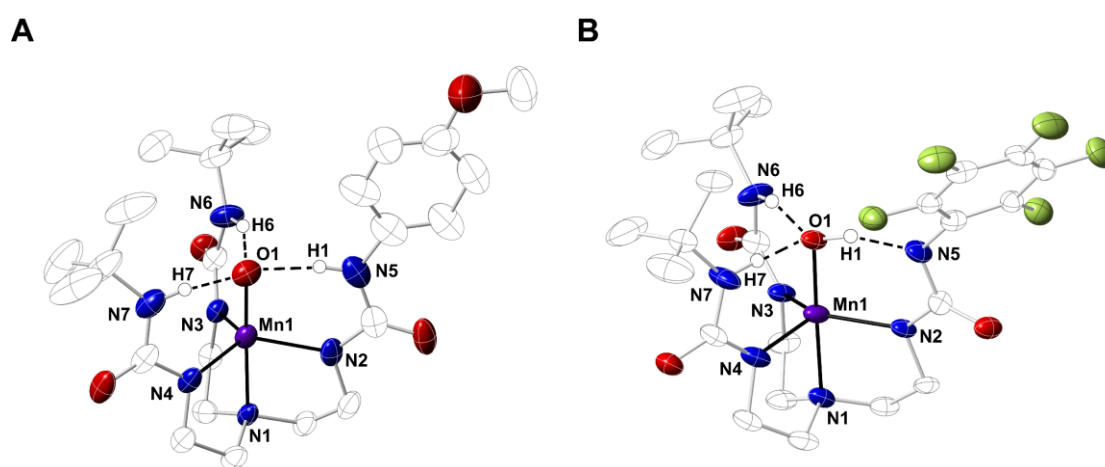


Figure 2-1. Molecular structure of (A) $\text{K}_2[\text{Mn}^{\text{III}}\text{H}_3\text{bpuea-OMe}(\text{O})]$ and (B) $\text{K}_2[\text{Mn}^{\text{III}}\text{H}_2\text{bpuea-OMe}(\text{OH})]$. Thermal ellipsoids are shown at the 50% probability level. Only ureayl and hydroxide hydrogen atoms are shown for clarity. Solvent molecules and potassium counter ions were omitted for clarity.

Table 2-1. Selected distances (Å) and angles (°) for $K_2[Mn^{III}H_3bpuea-OMe(O)]$ and $K_2[Mn^{III}H_2bpuea-5F(OH)]$.

Complexes	$K_2[Mn^{III}H_3bpuea-OMe(O)]$	$K_2[Mn^{III}H_2bpuea-5F(OH)]$
<i>Distances (Å)</i>		
Fe1–O1	1.771(3)	1.819(4)
Fe1–N1	2.095(4)	2.058(5)
Fe1–N2	2.087(3)	2.017(5)
Fe1–N3	2.084(3)	2.069(5)
Fe1–N4	2.039(3)	2.059(5)
O1··N5	2.613(5)	2.613(6)
O1··N6	2.701(5)	2.798(7)
O1··N7	2.732(5)	2.760(7)
<i>Angles (°)</i>		
O1–Fe1–N1	177.01(14)	178.6(2)

EPR and absorption properties of $[Mn^{III}(O)-R]^{2-}$ complexes

The electronic absorption spectrum of $[Mn^{III}(O)-OMe]^{2-}$ revealed two ligand-field bands with $\lambda_{max}/nm(\epsilon/M^{-1}cm^{-1}) = 500(420)$ and $714(210)$ (Figure 2-2A). The wavelengths and extinction coefficient of $[Mn^{III}(O)-OMe]^{2-}$ matched those found for $[Mn^{III}H_3buea(O)]^{2-}$. The EPR spectrum of $[Mn^{III}(O)-OMe]^{2-}$ has $g = 8.03$ ($A = 277$ MHz) with six-line hyperfine splitting (A) pattern that is consistent with a high-spin, mononuclear Mn^{III} complex (Figure 2-2B).

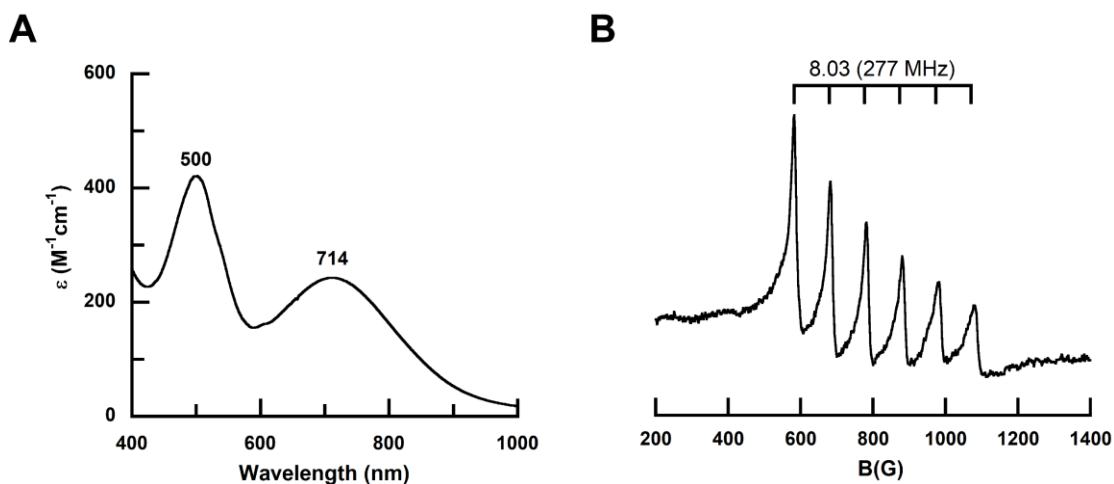


Figure 2-2. (A) Electronic absorption spectrum of $[Mn^{III}(O)-OMe]^{2-}$ in DMSO at room temperature. (B) EPR spectrum ($//$ -mode, 2:1 DMF:THF, 10 K, 21.4 mM) of $[Mn^{III}(O)-OMe]^{2-}$.

Comparing the electronic absorption spectrum of $[\text{Mn}^{\text{III}}(\text{O})\text{-OMe}]^{2-}$ with other $[\text{Mn}^{\text{III}}(\text{O})\text{-R}]^{2-}$ complexes, the higher energy band for all the complexes is found at $\lambda_{\text{max}} = 500$ nm with nearly identical extinction coefficients. There is a red shift of the lower energy band as more electron-withdrawing R-groups are appended to the phenyl ring (Table 2-2). This small shift corresponds to an energy difference of only ~ 340 cm^{-1} , suggesting there is little change in the ligand-field splitting for these complexes. In contrast, the electronic absorbance spectra for $[\text{Mn}^{\text{III}}(\text{O})\text{-CF}_3]^{2-}$ and $[\text{Mn}^{\text{III}}(\text{OH})\text{-5F}]^{2-}$ contain broad shoulders at $\lambda_{\text{max}} = 650$ and 677 nm that lack the similarity to other Mn^{III} -oxido species. The spectra of the $[\text{Mn}^{\text{III}}(\text{O})\text{-R}]^{2-}$ complexes indicates that complexes with $\text{R} = \text{OMe}$, H , F , and Cl can be best described as a monomeric Mn^{III} -oxido species, whereas the electronic absorption of $[\text{Mn}^{\text{III}}(\text{OH})\text{-5F}]^{2-}$ is consistent with the structural analysis of it as a Mn^{III} -hydroxido species.

Comparing the EPR spectrum of $[\text{Mn}^{\text{III}}(\text{O})\text{-OMe}]^{2-}$ with other $[\text{Mn}^{\text{III}}(\text{O})\text{-R}]^{2-}$ complexes, all of the EPR spectra are consistent with high-spin, mononuclear Mn^{III} complexes with g-values of ~ 8 (Table 2-2). However, a trend was observed in the A values among some of the complexes. For the $[\text{Mn}^{\text{III}}(\text{O})\text{-R}]^{2-}$ complexes with $\text{R} = \text{OMe}$, H , F , and Cl , A-values were found to range from 277 to 279 MHz, which are similar to the 280 MHz splitting observed for $[\text{Mn}^{\text{III}}\text{H}_3\text{buea}(\text{O})]^{2-}$. The A values decrease below 270 MHz for $[\text{Mn}^{\text{III}}(\text{O})\text{-CF}_3]^{2-}$ and $[\text{Mn}^{\text{III}}(\text{OH})\text{-5F}]^{2-}$, which are comparable to those we reported for the related Mn^{III} -OH complex, $[\text{Mn}^{\text{III}}\text{H}_3\text{buea}(\text{OH})]^-$.²⁰

Table 2-2. Spectroscopic results of the $[\text{Mn}^{\text{III}}(\text{O})\text{-R}]^{2-}$ complexes.

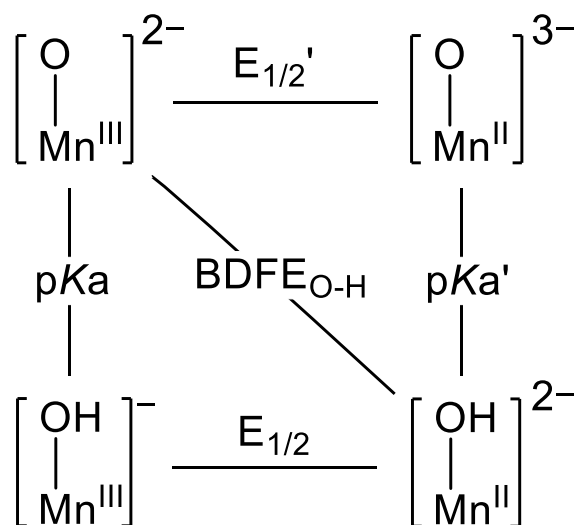
R	$\lambda_{\text{max}}/\text{nm}$ ($\epsilon/\text{M}^{-1}\text{cm}^{-1}$)	g (A/MHz)
OMe	714(210), 500(420)	8.03(277)
H	710(240), 498(440)	7.95(278)
F	706(240), 498(440)	7.95(278)
Cl	697(300), 600(430)	8.05(279)
CF ₃	650(300)	8.16(268)
5F	677(270)	7.97(262)

Thermodynamic square scheme

To experimentally determine the $BDFE_{O-H}$ of the $[Mn^{III}(O)-R]^{2-}$ complexes using the approach described in the Introduction, in which the pK_a and $E_{1/2}$ values needs to be measured based on Scheme 2-5 and $BDFE_{O-H}$ can be calculated based on equation (2-1)

$$BDFE_{O-H} = 23.06E_{1/2} + 1.37pK_a + C \quad (2-1)$$

Where C accounts for the thermodynamic properties of the hydrogen atom in solution and has a value of 71.1 kcal/mol for the conditions used in our studies.¹³ In the following sections, experiments of the $[Mn^{III}(O)-OMe]^{2-}$ complex will be discussed first as an example, then compared with other $[Mn^{III}(O)-R]^{2-}$ complexes.



Scheme 2-5. Thermodynamic square schemes for the $[Mn^{III}(O)-R]^{2-}$ complexes.

pK_a measurements

Titration of $[Mn^{III}(O)-OMe]^{2-}$ with 2-aminopyrimidine ($pK_a = 25.3^{21}$) showed decrease of absorbance at 500 nm and increase of absorbance at 714 nm, indicating conversion of $Mn^{III}-O$ to $Mn^{III}-OH$ (Figure 2-3A), giving determined pK_a value of 24.4 for $[Mn^{III}(O)-OMe]^{2-}$ (Figure 2-3B).

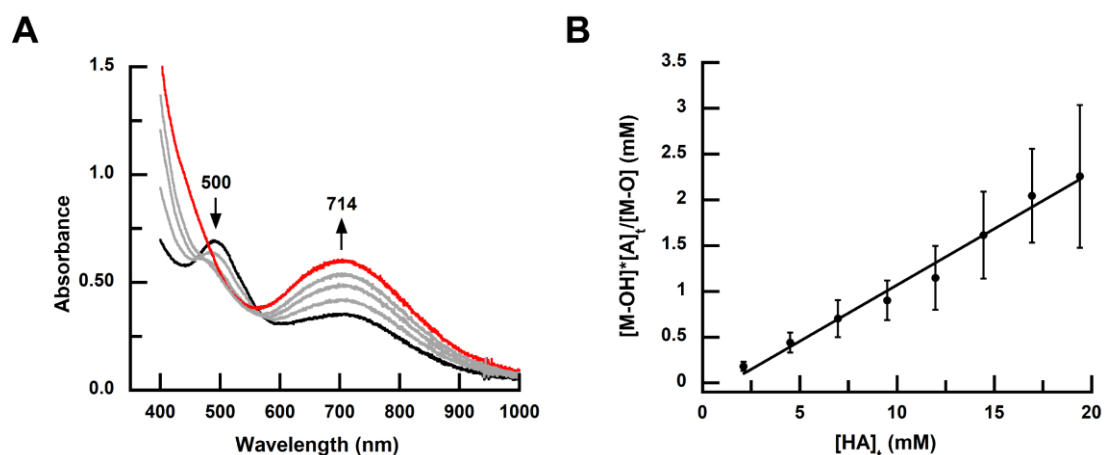


Figure 2-3. (A) Titration of $[\text{Mn}^{\text{III}}(\text{O})\text{-OMe}]^{2-}$ with 2-aminopyrimidine by monitoring the intensity at 714 nm. (B) Plot for determination of equilibrium constant and $\text{p}K_{\text{a}}$.

$E_{1/2}$ measurements

The redox properties of $\text{Mn}^{\text{III/II}}\text{-OH}$ are also needed for thermodynamic analysis. To obtain this value, the analogous $[\text{Mn}^{\text{II}}(\text{OH})\text{-OMe}]^{2-}$ complex was synthesized using H_2O through previously established procedures.^{22,23} The EPR spectrum of the $[\text{Mn}^{\text{II}}(\text{OH})\text{-OMe}]^{2-}$ complex was obtained to confirm the complex has $S = 5/2$ spin ground states consistent with a high-spin monomeric Mn^{II} complex (Figure 2-4A). Cyclic voltammetry (CV) was performed with the $[\text{Mn}^{\text{II}}(\text{OH})\text{-OMe}]^{2-}$ complex and redox event of $\text{Mn}^{\text{III/II}}\text{-OH}$ was observed with $E_{1/2} = -1.38$ V (vs. $[\text{FeCp}_2]^{+/0}$ in DMSO) (Figure 2-4B).

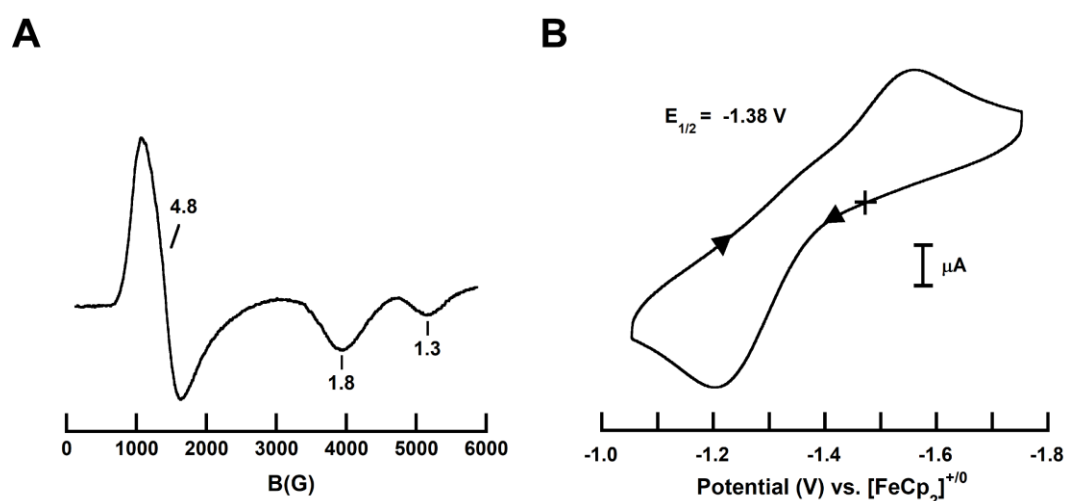


Figure 2-4. (A) EPR spectrum (\perp -mode, 10 K, 2:1 DMF:THF, 24.5 mM) of the $[\text{Mn}^{\text{II}}(\text{OH})\text{-OMe}]^{2-}$ complex. (B) Cyclic voltammogram of the $[\text{Mn}^{\text{II}}(\text{OH})\text{-OMe}]^{2-}$ complex measured in DMSO with glassy carbon working electrode, platinum wire counter electrode, silver wire reference electrode, and FeCp_2 as internal standard.

Thermodynamic parameters of the $[\text{Mn}^{\text{III}}(\text{O})\text{-R}]^{2-}$ complexes

With the determined $\text{p}K_{\text{a}}$ and redox values of the $[\text{Mn}^{\text{II}}(\text{OH})\text{-OMe}]^{2-}$ complex, the $\text{BDFE}_{\text{O-H}}$ was found to be 73 kcal/mol based on equation (1). Using same procedures, the $\text{p}K_{\text{a}}$ and redox values of other $[\text{Mn}^{\text{III}}(\text{O})\text{-R}]^{2-}$ complexes in this series were obtained, and the $\text{BDFE}_{\text{O-H}}$ of these complexes were determined (Table 2-3). The titration of the $[\text{Mn}^{\text{II}}(\text{OH})\text{-CF}_3]^{2-}$ and $[\text{Mn}^{\text{II}}(\text{OH})\text{-5F}]^{2-}$ complexes monitored by UV-vis spectroscopy was unsuccessful due to instability of the product. Therefore, the $\text{p}K_{\text{a}}$ of the two complexes were bracketed using various acids to be 22-23 and 19-20, respectively.

Table 2-3. Thermodynamic parameters of the $[\text{Mn}^{\text{III}}(\text{O})\text{-R}]^{2-}$ complexes.^a

R	$\text{p}K_{\text{a}}$	$E_{1/2}^{\text{b}}$	$\text{BDFE}_{\text{O-H}}^{\text{c}}$	k^{d}
OMe	24.4(1)	-1.38	73	0.038(3)
H	23.7(1)	-1.39	72	0.022(1)
F	23.8(1)	-1.41	71	0.019(2)
Cl	23.4(1)	-1.29	73	0.012(1)
CF_3	22-23	-1.33	71-72	0.0020(2)

^a In DMSO. ^b $\text{Mn}^{\text{III/II}}\text{-OH}$ redox couple in V versus $[\text{FeCp}_2]^{+/0}$. ^c kcal/mol. ^d $k = k_2/4$, $\text{M}^{-1}\text{s}^{-1}$.

CV analysis found redox event for each $[\text{Mn}^{\text{II}}(\text{OH})\text{-R}]^{2-}$ complex with $E_{1/2}$ values that only changed by 0.090 V vs $[\text{FeCp}_2]^{+/0}$ (Table 2-3) with no observable trend. In contrast, the data showed a direct correlation between the $\text{p}K_{\text{a}}$ values and the R-groups that can be illustrated by a Hammett analysis (Figure 2-5), with complexes containing more electron withdrawing groups have lower $\text{p}K_{\text{a}}$ values. This trend can be explained by the HN_{urea} groups with more electron withdrawing R-groups could provide stronger H-bond interaction with the Mn^{III} -oxido unit. Therefore, modulating this single H-bond interaction within the secondary coordination sphere allowed fine tuning of basicity of the complexes.

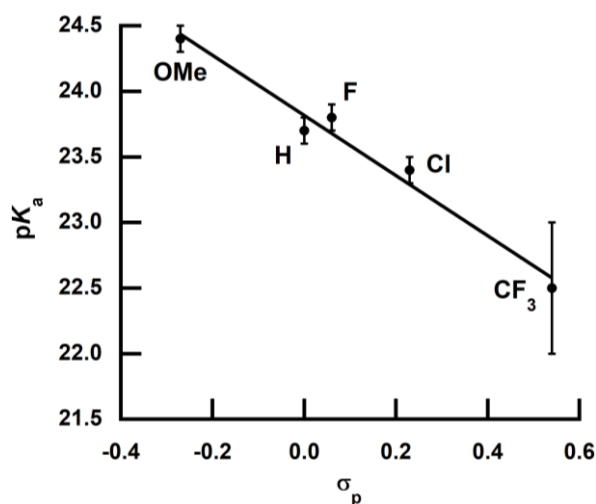
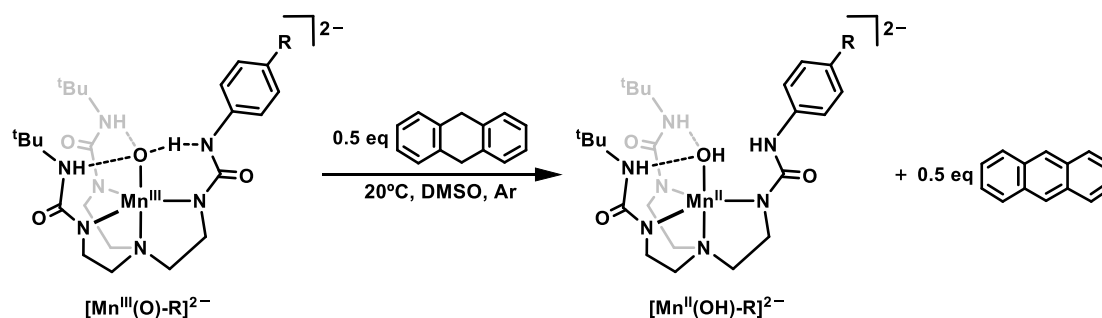


Figure 2-5. Hammett analysis with pK_a values of the $[\text{Mn}^{\text{III}}(\text{O})\text{-R}]^{2-}$ complexes.

Kinetic studies with 9,10-dihydroanthracene

9,10-Dihydroanthracene (DHA) was used as a substrate to investigate the reactivities of the $[\text{Mn}^{\text{III}}(\text{O})\text{-R}]^{2-}$ complexes for C–H bond cleavage (Scheme 2-6). The reaction was monitored by UV-vis spectroscopy: a decrease in the spectral features of $[\text{Mn}^{\text{III}}(\text{O})\text{-R}]^{2-}$ complexes and an increase in spectral features corresponding to anthracene product were observed (Figure 2-6A). To perform kinetic studies of the complexes, DHA was added in excess (>10 equiv.) to obtain pseudo-first order condition. The determined pseudo-first order rate constants (k_{obs}) were found to be linearly dependent on the concentration of DHA (Figure 2-6B). The slope of this linear relationship was used to determine the second-order rate constants (k_2) of each $[\text{Mn}^{\text{III}}(\text{O})\text{-R}]^{2-}$ complexes, which were corrected for the four chemically equivalent activable C–H bonds in DHA to give the reported second-order rate constant (k) (Table 2-3).



Scheme 2-6. Reaction of the $[\text{Mn}^{\text{III}}(\text{O})\text{-R}]^{2-}$ complexes with 9,10-dihydroanthracene.

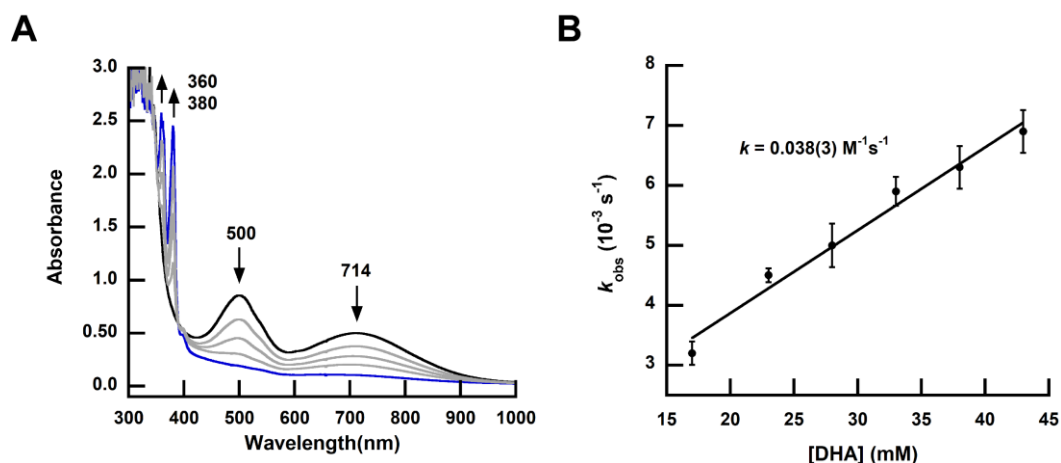


Figure 2-6. (A) Reaction between the $[\text{Mn}^{\text{II}}(\text{OH})\text{-OMe}]^{2-}$ complex (2mM) and excess DHA. (B) Plot of k_{obs} versus concentration of DHA. The slope of this linear relationship was used for determination of second order rate constant. The pseudo-first order rate constant of complexes R = OMe, H, F, and Cl were determined based on the feature at 500 nm, whereas that of R = CF_3 was determined based on the feature at 650 nm.

For the $[\text{Mn}^{\text{III}}(\text{O})\text{-OMe}]^{2-}$ complex, addition of 18-crown-6 (18C6) showed significant effect on k ($0.029(2) \text{ M}^{-1} \text{ s}^{-1}$ without 18C6 and $0.038(2) \text{ M}^{-1} \text{ s}^{-1}$ with 18C6). This is possibly due to the potassium ion interacting with the oxido unit, which was observed in the molecular structure of the the $[\text{Mn}^{\text{III}}(\text{O})\text{-OMe}]^{2-}$ complex. Addition of excess (10 equiv.) 18C6 can encapsulate the potassium ion and allow better accessibility of the oxido unit to the DHA that lead to higher k . However, the effect of 18C6 was not observed for the other $[\text{Mn}^{\text{III}}(\text{O})\text{-R}]^{2-}$ complexes in this series. Therefore, only k of the $[\text{Mn}^{\text{III}}(\text{O})\text{-OMe}]^{2-}$ complex was reported in the presents of excess 18C6.

The rate constants of the reactions decreases significantly as the R group becomes more electron withdrawing (Table 2-3), with the extreme case of $[\text{Mn}^{\text{III}}\text{H}_2\text{3}^{5\text{F}}(\text{OH})]^{-}$, which does not go through one half-life within a 24 h period even at 50° . However, The $\text{BDFE}_{\text{O-H}}$ of the complexes are all within experimental error with each other, which could be due to the tuning of H-bond is a subtle change on the coordination environment of the complexes, and therefore does not change the $\text{BDFE}_{\text{O-H}}$ by observable magnitude. Therefore, the relative trend of the rate constants cannot be correlated with their $\text{BDFE}_{\text{O-H}}$.

In contrast, the trend in the rate constants showed a correlation with the change in the basicity of the complexes, with the less basic complex having lower rate constant (Figure 2-7A).

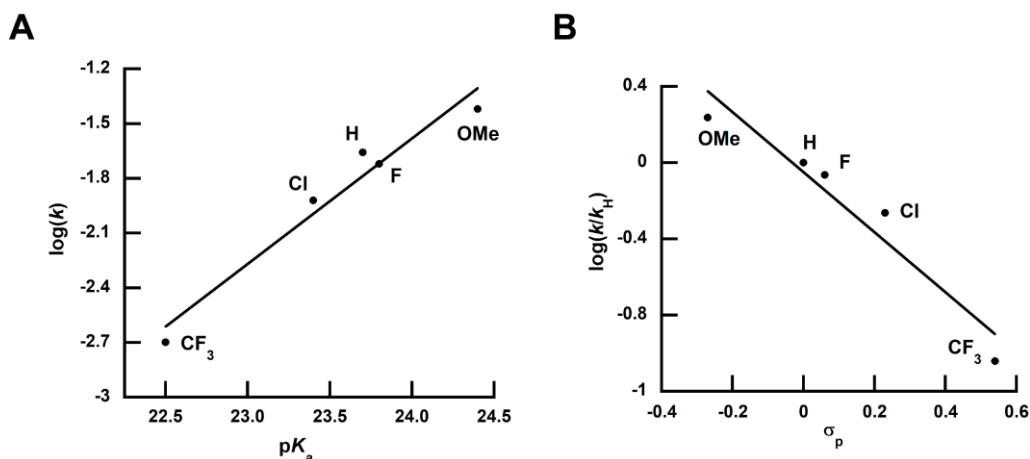


Figure 2-7. (A) Plot of $\log(k)$ vs pK_a for the oxidation of DHA and (B) Hammett analysis for the oxidation of DHA for the $[Mn^{III}(O)-R]^{2-}$ complexes.

As discussed before, the H-bond interaction between the oxido ligand and the para-substituted-phenyl urea NH can be modulated by substituent effects on the distal phenyl ring. Therefore, a Hammett correlation can be observed by plotting $\log(k/k_H)$ versus σ_p values of the para-substituents on distal phenyl ring, which resulted in a linear relationship with $\rho = -1.57$ (Figure 2-7B).

This analysis demonstrated the significant effects of one single H-bond interaction on both properties and reactivities of the Mn^{III} -oxido complexes without perturbing the primary coordination sphere of these complexes.

To gain additional insights into this process, the temperature dependence of the second-order rate constants was investigated to determine activation parameters for the $[Mn^{III}(O)-CR]^{2-}$ complexes with $R = OMe, H, Cl,$ and CF_3 . The rate constants were measured at 20, 30, 40, and 50°C to perform an Eyring analysis (Figure 2-8, Table 2-4). The enthalpies of activation (ΔH^\ddagger) for all four complexes were within experimental error of each other and agree with those reported for $[Mn^{III}H_3buea(O)]^{2-}$. The entropies of activation (ΔS^\ddagger) were also

similar to each other, with only that for $[\text{Mn}^{\text{III}}(\text{O})\text{-CF}_3]^{2-}$ being slightly lower. For these activation parameters, ΔH^\ddagger is greater than $-T\Delta S^\ddagger$, indicating a reaction profile for C–H bond cleavage with the enthalpy of activation predominates over the entropy of activation.

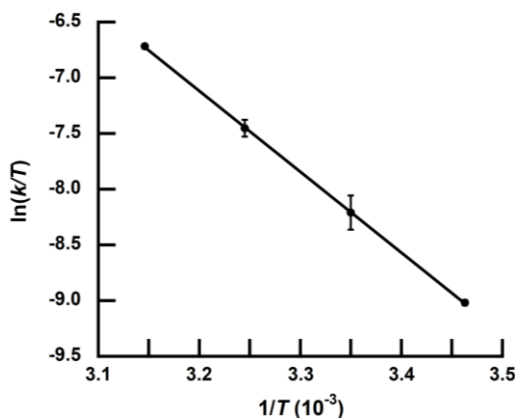


Table 2-4. Activation parameters of the $[\text{Mn}^{\text{III}}(\text{O})\text{-R}]^{2-}$ complexes.

R	ΔH^\ddagger (kcal/mol)	ΔS^\ddagger (e.u.)
OMe	15(1)	-15(2)
H	15(1)	-16(2)
Cl	15(1)	-15(2)
CF ₃	13(1)	-25(3)

Figure 2-8. Eyring analysis of the $[\text{Mn}^{\text{II}}(\text{OH})\text{-OMe}]^{2-}$ complex.

The kinetic isotope effects (KIE) of the the $[\text{Mn}^{\text{III}}(\text{O})\text{-R}]^{2-}$ complexes with R = OMe, H, Cl, and CF₃ were measured at 20 °C using *d*₄-DHA (Figure 2-9 and Table 2-5). The values obtained are ~ 5 indicative of primary isotope effects, which indicates that C–H bond cleavage is involved in the rate limiting step of the reaction. These values are larger than that was found for $[\text{Mn}^{\text{III}}\text{H}_3\text{buea}(\text{O})]^{2-}$ (KIE = 2.6).

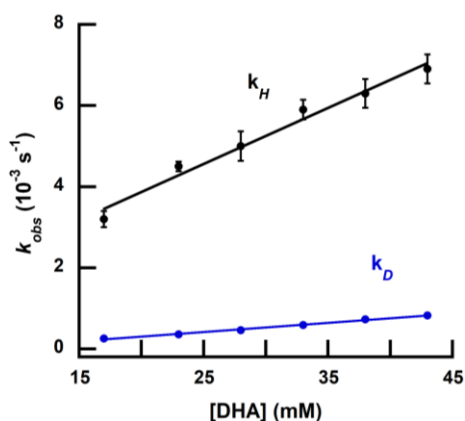


Table 2-5. KIE of the $[\text{Mn}^{\text{III}}(\text{O})\text{-R}]^{2-}$ complexes.

R	KIE
OMe	5.8
H	5.1
Cl	4.4
CF ₃	5.7

Figure 2-9. Second order rate constant of $[\text{Mn}^{\text{II}}(\text{OH})\text{-OMe}]^{2-}$ complex with DHA (black) and *d*₄-DHA (blue).

Reactivities with other substrates

To gain more insights into C–H bond cleavage by the $[\text{Mn}^{\text{III}}(\text{O})\text{-R}]^{2-}$ complexes, the reactivity of $[\text{Mn}^{\text{III}}(\text{O})\text{-H}]^{2-}$, $[\text{Mn}^{\text{III}}(\text{O})\text{-Cl}]^{2-}$, and $[\text{Mn}^{\text{III}}(\text{O})\text{-CF}_3]^{2-}$ with other substrates having different pK_a and BDFE values for their C–H bonds were explored (Table 2-6). When a more acidic substrate, fluorene ($pK_a = 22.6$ in DMSO whereas for DHA $pK_a = 30.1$), was used as substrate, only acid-base chemistry was observed with $[\text{Mn}^{\text{III}}(\text{OH})\text{-R}]^{2-}$ complexes as the initial product. When xanthene (XAN), which is a substrate with similar pK_a but lower BDFE as DHA was used, the obtained second-order rate constants were an order of magnitude higher than that was found for DHA.

Table 2-6. Second-order rate constant of the $[\text{Mn}^{\text{III}}(\text{O})\text{-R}]^{2-}$ complexes with various substrates.^a

R	DHA	Fluorene	Xanthene
H	0.022(1)	Acid-base	0.37(2)
Cl	0.012(1)	Acid-base	0.17(1)
CF ₃	0.0020(1)	Acid-base	0.014(1)

^a $\text{M}^{-1}\text{s}^{-1}$ in DMSO.

The reactivities of the $[\text{Mn}^{\text{III}}(\text{O})\text{-R}]^{2-}$ complexes with DHA suggest the basicity is the dominant factor in their reactivities toward C–H bond cleavage, but the reactivities with XAN revealed that the reaction cannot be explained by a simple two-steps PT-ET mechanism. These results suggest the possibility of an asynchronous transition state that is dominated by proton transfer with partial electron transfer. A similar premise has recently been reported for a Co^{III} -oxido complexes²⁴ and found for a theoretical analysis of $[\text{Fe}^{\text{III}}\text{H}_3\text{buea}(\text{O})]^{2-}$ and Fe^{IV} -oxido complexes.^{25,26}

Summary and Conclusion

Hydrogen bonds within the secondary coordination sphere have been invoked as an important factor that influences the properties and function of enzyme active site. The synthetic system discussed in this chapter demonstrated the significance of a single H-bond on Mn^{III}-oxido complex properties and reactivities. The design of the hybrid tripodal ligand, [H₃bpuea-R]³⁻, allowed fine tuning in a single H-bonding interaction that result in systematic changes within the secondary coordination sphere.

In this chapter, the comparison between the [Mn^{III}(O)-OMe]²⁻ complex I studied and other [Mn^{III}(O)-R]²⁻ complexes illustrated by changing R-groups in the para-position of the distal phenyl ring can allow precise modulation of a single H-bonding interaction and showed significant changes in basicity of Mn^{III}-oxido complexes that lead to reactivity rate changes. The structural comparison of the [Mn^{III}H₃bpuea(O)-OMe]²⁻ and [Mn^{III}H₂bpuea(OH)-5F]²⁻ demonstrated the HN_{urea} H-bond donor can be sufficient to promote intramolecular proton transfer.

The reactivity studies produced a Hammett analysis with linear correlation, suggesting the modulation of secondary coordination sphere can alter the rate of C–H bond cleavage by Mn^{III}-oxido complexes. The dependence of pK_a in reactivities with DHA and the significantly higher second-order rate constant in reactivities with XAN suggest the reaction mechanism cannot be explained by the three general mechanistic pathways of CPET, PT-ET, or ET-PT in a conventional square scheme. Therefore, a proton transfer dominated asynchronous processes was suggested to best fit for the C–H bond cleavage processes by the [Mn^{III}(O)-R]²⁻ complexes.

Experimental¹⁸

General procedure

Unless otherwise stated, all manipulations were performed under an Ar atmosphere in a Vacuum Atmospheres drybox. N,N-Dimethylacetamide (DMA) was purchased from Sigma-Aldrich and further dried as follows: prior to use, the liquid was stirred over BaO for 2 days, refluxed for 1 h, and then vacuum distilled. The DMA obtained was further dried by storing over molecular sieves (3 Å). 1-*tert*-Butyl-3-(2-chloroethyl)urea, N-*tert*-butoxycarbonyl-1,2-diaminoethane, (N'-*tert*-butoxycarbonyl)-N-ethyl]bis[(N'-*tert*-butylureayl), 1,1'-(((2-aminoethyl)azanediyl)bis-(ethane-2,1-diyl))bis(3-(*tert*-butyl)urea) were prepared by following literature methods.^{18,27–29} The metal precursor Mn^{II}(OAc)₂ was obtained from Sigma-Aldrich and was used as received. Potassium hydride (KH) as a 30% dispersion in mineral oil was filtered with a glass frit, washed with 20 mL of pentane and Et₂O five times, dried under vacuum, and stored under an Ar atmosphere. 9,10-Dihydroanthracene(DHA) was purchased from Sigma-Aldrich, crystallized from ethanol three times, washed with pentane, and dried under vacuum. *d*₄-DHA and *d*₂-xanthene were synthesized by following literature procedures.^{17,30} 4-Aminopyridine was purchased from Sigma-Aldrich in ≥99% purity, crystallized from toluene, washed with Et₂O, and dried under vacuum. 2-Amino-pyrimidine was purchased from Sigma-Aldrich in 97% purity, crystallized from EtOH three times, washed with Et₂O, and dried under vacuum. Silica gel (40–60 μm) was used for column chromatography to purify the ligand precursors.

Physical methods

Electronic absorption spectra for kinetics experiments were recorded in a 1 cm cuvette on an 8453E Agilent UV–vis spectrophotometer equipped with an Unisoku Unispeks cryostat. Room-temperature electronic absorption spectra

for determining extinction coefficients were recorded in a 1 cm cuvette on a Cary 50 spectrophotometer. Room-temperature electronic absorption spectra used for measuring the pKa values of the Mn– OH complexes were recorded in a 1 cm cuvette on a Cary 60 spectrophotometer that was housed within a N₂ atmosphere glovebox; connections were made using fiber-optic cables. Electron paramagnetic resonance (EPR) spectra were recorded using an Xband Bruker EMX spectrometer equipped with an ER041XG microwave bridge, an Oxford Instrument liquid-helium quartz cryostat, and a dual-mode cavity (ER4116DM). ¹H and ¹³C NMR spectroscopies were conducted using a Bruker DRX500 spectrometer. Cyclic voltammetry experiments were conducted using a CHI600C electrochemical analyzer. A 2.0 mm glassy carbon electrode was used as the working electrode at scan velocities of 50 mV s⁻¹. A ferrocenium/ferrocene couple (FeCp²⁺ /FeCp²) was used to monitor the Ag wire reference electrode, and all potentials are referenced to the [FeCp²⁺]/0 couple.

X-ray crystallography for K₂[Mn^{III}H₃bpuea-OMe(O)]

A green crystal of approximate dimensions 0.166 x 0.345 x 0.409 mm was mounted in a cryoloop and transferred to a Bruker SMART APEX II diffractometer. The APEX2³¹ program package was used to determine the unit-cell parameters and for data collection (60 sec/frame scan time for a sphere of diffraction data). The raw frame data was processed using SAINT³² and SADABS³³ to yield the reflection data file. Subsequent calculations were carried out using the SHELXTL³⁴ program. There were no systematic absences nor any diffraction symmetry other than the Friedel condition. The centrosymmetric triclinic space group $P\bar{1}$ was assigned and later determined to be correct.

The structure was solved by dual space methods and refined on F² by full-matrix least-squares techniques. The analytical scattering factors³⁵ for neutral atoms were used throughout the analysis. Hydrogen atoms were included

using a riding model. Hydrogen atoms associated with O(14) and O(15) could not be located and were not included in the refinement. Least-squares analysis yielded $wR2 = 0.2666$ and $Goof = 1.035$ for 816 variables refined against 20897 data (0.73 Å), $R1 = 0.0873$ for those 14060 data with $I > 2.0\sigma(I)$. There were several high residuals present in the final difference-Fourier map. It was not possible to determine the nature of the residuals. The SQUEEZE³⁶ routine in the PLATON³⁷ program package was used to account for the electrons in the solvent accessible voids.

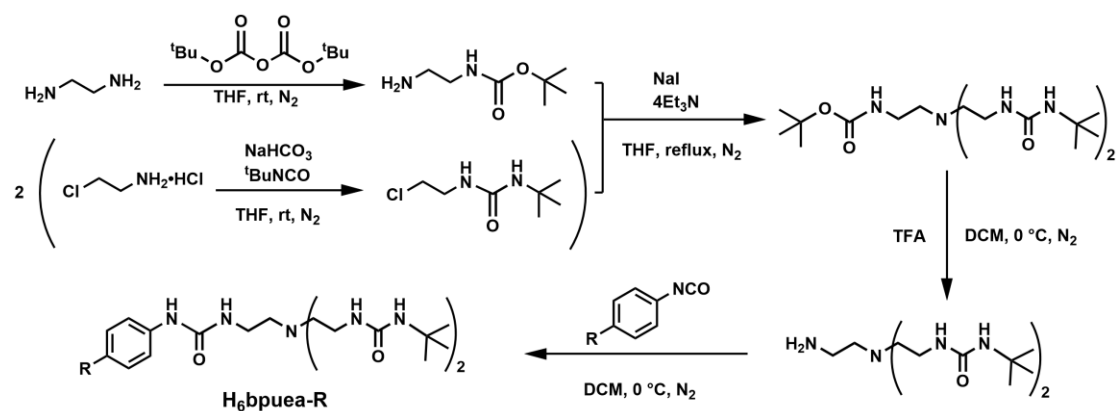
Table 2-S1. Metric parameters for $K_2[Mn^{III}H_3bpuea-OMe(O)] \cdot H_2O \cdot 1.5 DMA$.

Complex	$K_2[Mn^{III}H_3bpuea-OMe(O)] \cdot H_2O \cdot 1.5 DMA$
Empirical Formula	$[C_{57}H_{103}K_4Mn_2N_{17}O_{15}]_{\infty}$
Fw	1532.84
T (K)	88(2)
Crystal system	Triclinic
Space group	$P\bar{1}$
a (Å)	14.941(1)
b (Å)	14.996(1)
c (Å)	20.121(1)
α (°)	99.745(1)
β (°)	105.665(1)
γ (°)	94.127(1)
V (Å ³)	4244.3(5)
Z	2
δ_{calcd} (Mg/m ³)	1.199
GOF on F ²	1.035
R1	0.0873
wR2	0.2666
CCDC#	1904549

Synthesis of 1-(2-(bis(2-(3-(*tert*-butyl)ureido)ethyl)amino)ethyl)-3-(4-methoxyphenyl)urea (H₆bpuea-OMe)

The first four steps of the synthesis were based on reported procedures, and the last step of the synthesis is described here (Scheme 2-S1): 1,1'-(((2-aminoethyl)azanediyl)-bis(ethane-2,1-diyl))bis(3-(*tert*-butyl)urea) (2.14 g, 6.19 mmol) was dissolved in 50 mL of CH₂Cl₂ and cooled to 0 °C in an ice bath. 4-

Methoxyphenyl isocyanate (1.015 g, 6.807 mmol), which was dissolved in 80 mL CH₂Cl₂, was added dropwise solution for over 1 hr. The ice bath was removed, and the reaction was stirred overnight. Volatiles were removed under reduced pressure to give a white solid which was purified using column chromatography over silica gel: from TLC two impurities were found with R_f values larger than the products. To remove these impurities the following conditions were used: a 1% Et₃N in EtOAc mixture was used to elute the first impurity, a 1% Et₃N/20% MeOH in EtOAc mixture eluted the second impurity and a 1% Et₃N/40% MeOH in EtOAc mixture gave 2.459 g of a white solid (80.42 %). ¹H NMR (500 MHz, DMSO, ppm): 1.24 (s, 18H), 2.45-2.53 (m, 6H), 3.04 (q, 4H), 3.12 (q, 2H), 3.71 (s, 3H), 5.72 (m, 4H), 6.09 (t, 1H), 6.82(d, 2H), 7.30 (d, 2H), 9.31 (s, 1H). ¹³C NMR (500 MHz, CDCl₃, ppm): 159.05, 157.43, 155.41, 132.75, 121.50, 114.25, 55.61, 50.11, 46.46, 38.13, 29.68. HRMS (ES+) [C₂₄H₄₃N₇O₄ + Na⁺], 516.3274. Found 516.3274.



Scheme 2-S1. Synthesis of H₆bpuea-R ligand.

Synthesis of K₂[Mn^{III}H₃bpuea-OMe(O)]

H₆bpuea-OMe (152 mg, 0.307 mmol) was dissolved in 3 mL of DMA, and solid KH (51.6 mg, 1.29 mmol) was added in one portion. The mixture was stirred for 45 min until gas evolution to cease. The solution was treated with solid Mn^{II}(OAc)₂ (54.5 mg, 0.315 mmol) and stirred for an additional 2 hr to produce a light yellow heterogeneous mixture. After transferring to a Schlenk flask and

sealing with a rubber septum, the mixture was treated with dry O₂ (3.4 mL, 0.15 mmol), which produced an immediate color change to brown. The mixture was further allowed to stir for 2 hr and then degassed under vacuum for 5 min. The flask was transferred back to a drybox, after which the reaction mixture was filtered through a medium-porosity glass filter, and the brown filtrate was layered with 10 mL of Et₂O. After 1 day, a brown solid was collected on a medium porosity glass filter and washed with 20 mL of MeCN and 5 mL of Et₂O to give 159 mg of the desired purple solid (81%). Single crystals suitable for X-ray diffraction were obtained by vapor diffusion of Et₂O to a dimethylformamide (DMF) solution of the product. λ_{\max}/nm (DMSO, $\epsilon/M^{-1}\text{cm}^{-1}$): 714, (211); 500, (419). EPR (2:1 DMF:tetrahydrofuran (THF), 10 K): $g = 8.03$, $A_z = 277$ MHz. HRMS (ES⁺): [C₂₄H₄₀K₂MnN₇O₅ + H⁺], 640.1824; found, 640.1826. Anal. Calcd (found) for C₂₄H₄₀K₂MnN₇O₅•H₂O: C, 43.82 (43.87); H, 6.44 (6.53); N, 14.91 (15.50). FTIR (ATR, cm⁻¹): 2961, 2896, 2853, 2831, 1661, 1595, 1579, 1526, 1505, 1447, 1407, 1382, 1352, 1327, 1315, 1249, 1223, 1201, 1177, 1139, 1092, 1061, 1034, 915, 850, 828, 787, 758, 722, 682, 660.

Synthesis of K₂[Mn^{II}H₃bpuea-OMe(OH)]

H₆bpuea-OMe (219 mg, 0.442 mmol) was dissolved in 3 mL DMA. Solid KH (76 mg, 1.9 mmol) was added and stirred for 45 min until bubbling ceased. Mn^{II}(OAc)₂ (80.6 mg, 0.466 mmol) was then added and the resultant mixture was stirred for 2 hr to produce a light yellow heterogenous mixture. Water (8.0 μL , 0.44 mmol) was added and the reaction mixture was stirred for an additional 1 hr. The reaction was filtered through a medium porous glass fritted funnel and the filtrate was layered with 15 mL of Et₂O. After 1 day, a light-yellow precipitate was obtained and washed with 5 mL of Et₂O and dried under vacuum to afford 0.125 g of the desired product (44%). Anal. Calcd (found) for C₂₃H₄₃F₅K₂MnN₇O₅•DMA: C, 47.04 (46.55); H, 7.53 (7.33); N, 15.43 (15.40).

pK_a Measurements

For a typical set of pK_a measurements, ~ 8 mL of a 1-2 mM stock solution of Mn^{III} complex was prepared in DMSO. Using a volumetric pipette, 2 mL of the Mn^{III} complex stock solution was transferred into a 1 cm cuvette. Stock solution of 2-aminopyrimidine (pK_a = 25.3 in DMSO) was prepared with concentrations between 0.5-2 M. Via a syringe, aliquots of acids were injected in 5 μL increment of the lowest concentration stock solution first, then with larger volume and higher concentration gradually. After each addition of acids, the solutions were allowed to fully mix and come to equilibrium before each titration point was optically collected. For calculation, mass balance was assumed, and Henderson-Hasselbalch equation was used. The measured equilibrium constant *K* and the pK_a of 2-aminopyrimidine is used to determine the pK_a value of the Mn^{III}-O complexes (eq. 2-S1). Detailed derivation of the pK_a value can be found in previously reported procedures.¹⁸

$$pK_a (\text{Mn}^{\text{II}}(\text{OH})) = \log K + pK_a (\text{HA}) \quad (\text{eq. 2-S1})$$

Kinetic studies.

All kinetic experiments were done with 1-2 mM solutions of Mn^{III} complex in DMSO. The concentration of each Mn^{III} complex was determined using the extinction coefficient at λ_{max} = ~ 500 nm. 5 ml 470 mM of stock solution was prepared for substrate (DHA or xanthene). Using a volumetric pipette, 2 ml of Mn^{III} complex solution was taken in a cuvette (containing a stir-bar) with 1 cm pathlength. Then the cuvette was allowed to equilibrate with the temperature for ~10 min. Then the reaction was initiated with injecting the stock solution of substrate (75 μL to 200 μL with 25 μL increment). The progress of the reaction was monitored by following the decrease in absorbance at 500 nm. Experiments at each temperature and for each concentration of DHA or xanthene were repeated at least three times. Under these conditions, substrate

concentration was in excess (>10 equiv.) compared to complex concentration to provide pseudo first-order reaction conditions. The expression, $\ln[(A_t - A_f)/(A_i - A_f)]$, was plotted against the reaction time for the first three half-lives of any reaction to provide linear plots. Here, A_i is the initial absorbance, A_t is the absorbance at time t , and A_f is the absorbance at the endpoint of the reaction at 500 nm. The observed pseudo first-order rate constants (k_{obs} , s^{-1}) for each reaction was determined from the slope/2 of the above-mentioned linear plots. The factor of 2 is necessary to account for the stoichiometry of the reaction as for the oxidation of one DHA molecule, 2 equiv. of complex were required.

Experiments where the substrate concentration was constant while varying the Mn^{III} complex concentration were performed to confirm the rate of the reaction is second order. Therefore, the second-order rate law can be utilized (eq. 2-S2)

$$\text{Rate} = [Mn^{III}(O)-R][DHA] \quad (\text{eq. 2-S2})$$

When k_{obs} for various concentrations of DHA at a particular temperature were plotted against the concentrations of DHA, a linear dependence was observed. This is consistent with pseudo first-order reaction conditions as k_{obs} is expected to follow $k_{obs} = k_2[DHA]$ where k_2 is the second-order rate constants. Now the second-order rate constants were divided by 4 to normalize for the 4 equivalently reactive C–H bonds per DHA molecule to provide the corrected second-order rate constants k ($k = k_2/4$). For xanthene (XAN), the second-order rate constants were divided by 2 to normalize for the 2 equivalently reactive C–H bonds per XAN molecule to provide the corrected second-order rate constants k ($k = k_2/2$).

References

- (1) Baglia, R. A.; Zaragoza, J. P. T.; Goldberg, D. P. *Chem. Rev.* **2017**, *117* (21), 13320–13352.
- (2) Gunay, A.; Theopold, K. H. *Chem. Rev.* **2010**, *110* (2), 1060–1081.
- (3) McDonald, A. R.; Que, L. *Coord. Chem. Rev.* **2013**, *257* (2), 414–428.
- (4) Borovik, A. S. *Chem. Soc. Rev.* **2011**, *40* (4), 1870–1874.
- (5) Sacramento, J. J. D.; Goldberg, D. P. *Acc. Chem. Res.* **2018**, *51* (11), 2641–2652.
- (6) Rice, D. B.; Massie, A. A.; Jackson, T. A. *Acc. Chem. Res.* **2017**, *50* (11), 2706–2717.
- (7) Groves, J. T.; McClusky, G. A. *J. Am. Chem. Soc.* **1976**, *98* (3), 859–861.
- (8) Groves, J. T. *J. Am. Chem. Soc.* **1985**, *62* (11), 924–927.
- (9) Green, M. T.; Dawson, J. H.; Gray, H. B. *Science (80-)*. **2004**, *304* (5677), 1653–1656.
- (10) Rittle, J.; Green, M. T. *Science (80-)*. **2010**, *330*, 933–937.
- (11) Stone, K. L.; Borovik, A. S. *Curr. Opin. Chem. Biol.* **2009**, *13*, 114–118.
- (12) Green, M. T. *Curr. Opin. Chem. Biol.* **2009**, *13* (1), 84–88.
- (13) Warren, J. J.; Tronic, T. A.; Mayer, J. M. *Chem. Rev.* **2010**, *110* (12), 6961–7001.
- (14) Darcy, J. W.; Koronkiewicz, B.; Parada, G. A.; Mayer, J. M. *Acc. Chem. Res.* **2018**, *51* (10), 2391–2399.
- (15) Bell, R. P. *Proc. R. Soc. A* **1936**, *154*, 414–429.
- (16) Evans, M. G.; Polanyi, M. *Trans. Faraday Soc.* **1938**, *34*, 11–24.
- (17) Parsell, T. H.; Yang, M. Y.; Borovik, A. S. *J. Am. Chem. Soc.* **2009**, *131* (8), 2762–2763.
- (18) Barman, S. K.; Jones, J. R.; Sun, C.; Hill, E. A.; Ziller, J. W.; Borovik, A. S. *J. Am. Chem. Soc.* **2019**, *141* (28), 11142–11150.
- (19) MacBeth, C. E.; Gupta, R.; Mitchell-Koch, K. R.; Young, V. G.; Lushington, G. H.; Thompson, W. H.; Hendrich, M. P.; Borovik, A. S. *J. Am. Chem. Soc.* **2004**, *126* (8), 2556–2567.
- (20) Peterson, S. M.; Shook, R. L.; Borovik, A. S. *ACS Natl. Meet. B. Abstr.* **2011**, No. eq 1, 5810–5817.
- (21) Bordwell, F. G. *Acc. Chem. Res.* **1988**, *21* (12), 456–463.
- (22) MacBeth, C. E.; Gupta, R.; Mitchell-Koch, K. R.; Young, V. G.; Lushington, G. H.; Thompson, W. H.; Hendrich, M. P.; Borovik, A. S. *J. Am. Chem. Soc.* **2004**, *126* (8), 2556–2567.
- (23) Gupta, R.; MacBeth, C. E.; Young, V. G.; Borovik, A. S. *J. Am. Chem. Soc.* **2002**, *124* (7), 1136–1137.
- (24) Goetz, M. K.; Anderson, J. S. *J. Am. Chem. Soc.* **2019**, *141* (9), 4051–4062.
- (25) Usharani, D.; Lacy, D. C.; Borovik, A. S.; Shaik, S. *J. Am. Chem. Soc.* **2013**, *135* (45), 17090–17104.
- (26) Bím, D.; Maldonado-Domínguez, M.; Rulísek, L.; Srnc, M. *Proc. Natl. Acad. Sci. U. S. A.* **2018**, *115* (44), E10287–E10294.

- (27) Lucas, R. L.; Zart, M. K.; Mukherjee, J.; Sorrell, T. N.; Powell, D. R.; Borovik, A. S. *J. Am. Chem. Soc.* **2006**, *128*, 15476–15489.
- (28) Jones, J. R.; Ziller, J. W.; Borovik, A. S. *Inorg. Chem.* **2017**, *56* (3), 1112–1120.
- (29) Douat-Casassus, C.; Marchand-Geneste, N.; Diez, E.; Gervois, N.; Jotereau, F.; Quideau, S. *J. Med. Chem.* **2007**, *50* (7), 1598–1609.
- (30) Gao, H.; Groves, J. T. *J. Am. Chem. Soc.* **2017**, *139* (11), 3938–3941.
- (31) APEX3 Version 2014.1-1, Bruker AXS Inc: Madison, WI 2014.
- (32) SAINT Version 8.34a, Bruker AXS Inc: Madison, WI 2013.
- (33) Sheldrick, G. M. SADABS Version 2014/5, Bruker AXS, Inc: Madison 2014.
- (34) Sheldrick, G. M. SHELXTL Version 2014/7, Bruker AXS, Inc: Madison 2014.
- (35) Wilson, A. J. C.; Geist, V. *Cryst. Res. Technol.* **1993**, *28* (1), 110.
- (36) Spek, A. L. *Acta Crystallogr. Sect. C Struct. Chem.* **2015**, *71* (1), 9–18.
- (37) Spek, A. L. *Acta Crystallogr. Sect. D Biol. Crystallogr.* **2009**, *65* (2), 148–155.

Chapter 3 – Investigation of Iron–Ammine and Amido Complexes within a C₃-Symmetrical Phosphinic Amido Tripodal Ligand

Introduction

Many of the physical and chemical properties of metal complexes are governed by the primary and secondary coordination spheres. The active sites in metalloproteins exemplify how these coordination spheres can interact to achieve highly functional systems.^{1,2} One major difference between them is that the primary coordination sphere relies on covalent bonds whereas the secondary coordination sphere often uses non-covalent interactions, such as hydrogen bonds (H-bonds) and electrostatic interactions. There are now several examples of bioinspired synthetic complexes which were designed to better understand how the two coordination spheres cooperate.^{3–7} The Borovik lab has been developing metal complexes with intramolecular H-bonds to investigate how these interactions affect the structure and function of first-row transition metal complexes.^{8,9} Most of our studies have focused on designing tripodal ligands that have two distinct characteristics: 1) they have anionic N-atom donors within the trigonal plane to support high-valent metal centers, and 2) they enforce relatively rigid frameworks that position H-bond donors or acceptors proximal to the metal center(s).

One symmetrical tripodal ligand that has been studied is *N,N',N''*-[2,2',2''-nitriлотris(ethane-2,1-diyl)]tris(2,4,6-trimethylbenzenesulfonamido) ([MST]³⁻, Figure 1A),^{10,11} which provides a trianionic metal binding pocket and incorporates sulfonamido O-atoms within the secondary coordination sphere to serve as H-bond acceptors.^{12,13} One limitation of using this ligand is that sulfonamido groups cannot stabilize metal centers with formal oxidation states higher than 3+. ¹⁴ To circumvent this problem, a new related symmetrical tripodal

ligand was recently introduced: *N,N',N''*-[nitrilotris(ethane-2,1-diyl)]tris(*P,P*-diphenylphosphinic amido) ([poat]³⁻, Figure 1C) that has phosphinic amido groups instead of sulfonamido groups and was found to stabilize Fe^{IV}-oxido complexes.¹⁵ These findings suggested that phosphinic amido donors provide a stronger ligand field than the corresponding sulfonamido groups. To provide more quantitative evidence for this difference between the properties of [MST]³⁻ and [poat]³⁻ (Figure 1), analogous Fe complexes in [poat]³⁻ ligand framework were synthesized.

This chapter discuss investigation in the chemistry of [Fe^{II/III}poat]^{-/0} complexes and the related Fe-NH₃ (ammine) and Fe-NR₂ (amido) species.¹⁶⁻²³ The structural, vibrational, and redox properties of these newly synthesized Fe-NH₃ complexes were directly compared with the analogous Fe complexes in [MST]³⁻ (Figure 3-1B) that have been previously reported.²⁴ This comparison clearly demonstrates that the phosphinic amido groups do indeed provide a stronger ligand field which stabilizes higher oxidation states. Moreover, this work shows that the P=O groups are excellent H-bond acceptors and assist in forming relatively strong intramolecular H-bonds.

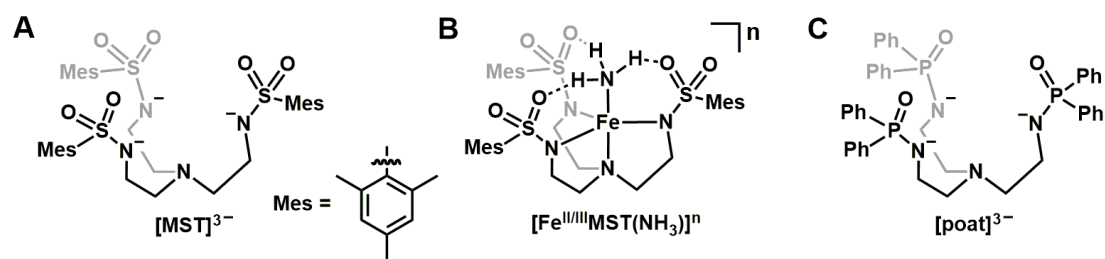


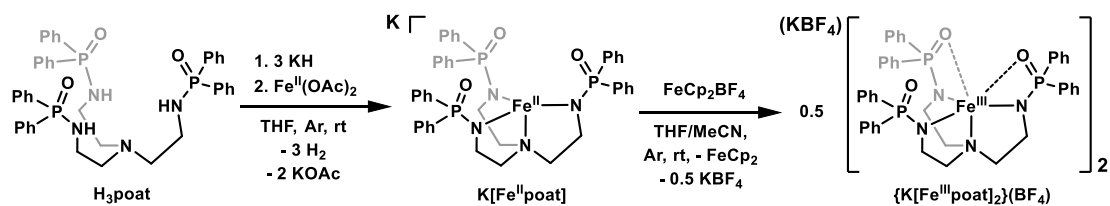
Figure 3-1. Diagrams of (A) [MST]³⁻, (B) [Fe^{II/III}]MST(NH₃)^{-/0} complexes, and (C) [poat]³⁻.

Result and Discussion

Synthesis of K(crypt)[Fe^{II}poat(NH₃)] and [Fe^{III}poat(NH₃)]

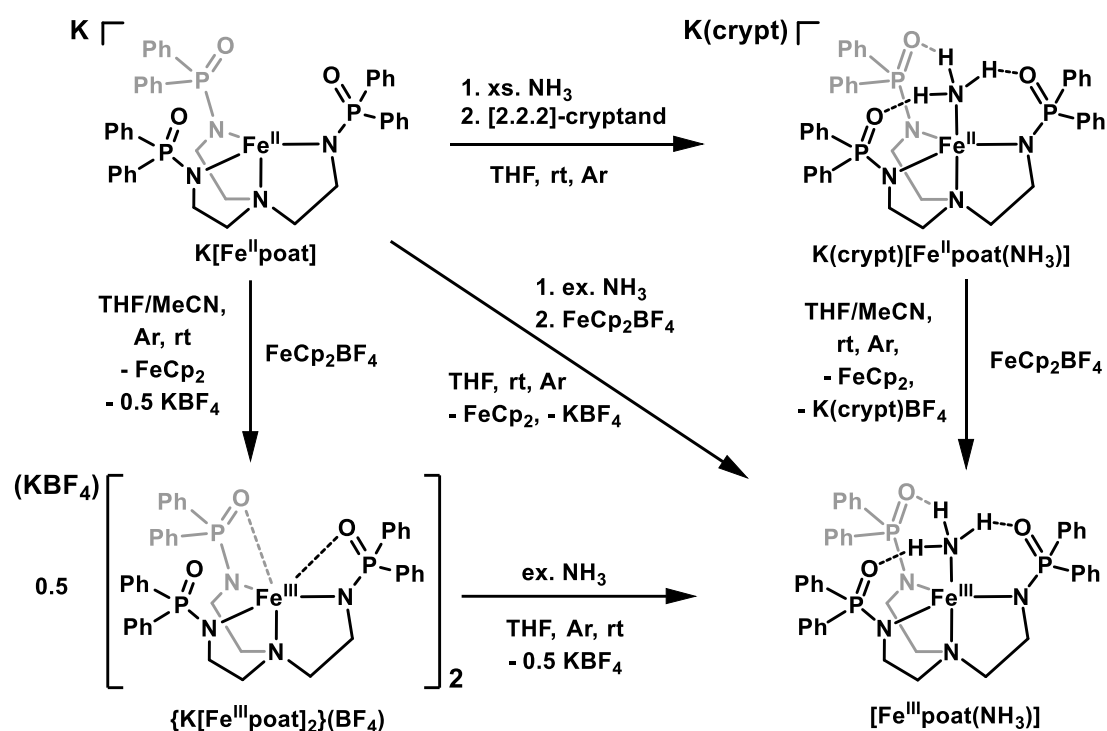
The two synthons, K[Fe^{II}poat] and [Fe^{III}poat], were synthesized based on previously reported procedures with slight modifications (Scheme 3-1) and used for preparation of Fe-NH₃ complexes. The ligand precursor H₃poat was

deprotonated using three equivalents of KH followed by metalation with $\text{Fe}(\text{OAc})_2$ to yield $\text{K}[\text{Fe}^{\text{II}}\text{poat}]$ as yellow crystals in yields of >70 %. Oxidation of $\text{K}[\text{Fe}^{\text{II}}\text{poat}]$ by ferrocenium tetrafluoroborate (FcCp_2BF_4) in THF/acetonitrile (MeCN) produced $[\text{Fe}^{\text{III}}\text{poat}]$ as a red solid in >80 % yield. The $[\text{Fe}^{\text{III}}\text{poat}]$ complex formed as an aggregate of $\{\text{K}[\text{Fe}^{\text{III}}\text{poat}]_2\}\text{BF}_4$ in the crystalline phase, but the KBF_4 will be omitted in future discussion for clarity.



Scheme 3-1. Synthesis of $\text{K}[\text{Fe}^{\text{II}}\text{poat}]$ and $[\text{Fe}^{\text{III}}\text{poat}]$.

The vacant axial coordination site in $[\text{Fe}^{\text{II}}\text{poat}]^-$ provided an opportunity to examine the effects of binding external ligands. Initial attempts to synthesize $\text{K}[\text{Fe}^{\text{II}}\text{poat}(\text{NH}_3)]$ from $\text{K}[\text{Fe}^{\text{II}}\text{poat}]$ and NH_3 solution in THF were unsuccessful and appeared to only give the starting $\text{K}[\text{Fe}^{\text{II}}\text{poat}]$ complex. We reasoned that the strong $\text{P}=\text{O} \cdots \text{K}$ interactions could possibly interfere with the stability of the complex by hindering the intramolecular H-bonds that are presumably formed between the NH_3 ligand and $[\text{poat}]^{3-}$. To overcome this synthetic problem, we introduced [2.2.2]-cryptand (crypt) to the reaction mixture to encapsulate the K^+ ion and avoid any interactions with $[\text{Fe}^{\text{II}}\text{poat}(\text{NH}_3)]^-$. This route proved successful and the desired salt, $[\text{K}(\text{crypt})][\text{Fe}^{\text{II}}\text{poat}(\text{NH}_3)]$, was prepared in greater than 85% yield as yellow crystals (Scheme 3-2).



Scheme 3-2. Synthesis of K(crypt)[Fe^{II}poat(NH₃)] and [Fe^{III}poat(NH₃)].

The cyclic voltammogram (CV) of [Fe^{II}poat(NH₃)]⁻ measured in DCM:THF revealed a one-electron reversible redox couple at $E_{1/2} = -1.21$ V versus [Fe^{III/II}Cp₂]⁺⁰ (Figure 3-2A). This potential is 0.57 V more negative than the analogous redox process found in [Fe^{II}MST(NH₃)]⁻ which has an $E_{1/2} = -0.64$ V versus [Fe^{III/II}Cp₂]⁺⁰ in DCM:THF (Figure 3-2B). This large difference in redox potentials agrees with our other observations that phosphinic amido groups are useful in stabilizing higher oxidized metal complexes. For example, we recently showed that [poat]³⁻ can stabilize an unusual high-spin Fe^{IV}=O complex which is not possible with tripodal sulfonamido ligands.^{14,15} The [Fe^{II}poat(NH₃)]⁻ and [Fe^{II}MST(NH₃)]⁻ complexes have the same trigonal bipyramidal geometry with an N-donor environment, yet their redox properties differ significantly. This suggests a key factor contributing to the difference in their redox potentials is that the phosphinic amido donors provide a stronger ligand field to the Fe center than the sulfonamido groups.

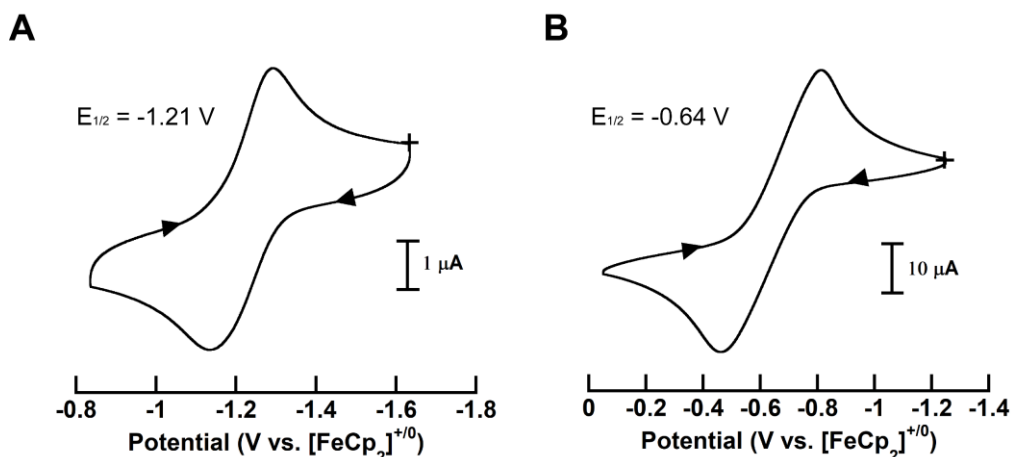


Figure 3-2. CV of (A) $\text{K}(\text{crypt})[\text{Fe}^{\text{II}}\text{poat}(\text{NH}_3)]$ and (B) $\text{Na}[\text{Fe}^{\text{II}}\text{MST}(\text{NH}_3)]$ in DCM:THF. The measurement was done with 100 mV/s scan rate using 100 mM tetrabutylammonium hexafluorophosphate (TBAPF_6) as electrolyte, glassy carbon electrode as working electrode, platinum wire as counter electrode, silver wire as reference electrode, and $[\text{Fe}^{\text{III/II}}\text{Cp}_2]^{+/0}$ couple as internal standard.

The information obtained from the CV experiments suggests $[\text{Fe}^{\text{III}}\text{Cp}_2]\text{BF}_4$ is a suitable oxidant to prepare the one-electron oxidized analogue of $\text{K}(\text{crypt})[\text{Fe}^{\text{II}}\text{poat}(\text{NH}_3)]$. Two independent routes were used (Scheme 3-2): a direct oxidation of $\text{K}(\text{crypt})[\text{Fe}^{\text{II}}\text{poat}(\text{NH}_3)]$ in THF/MeCN and an indirect method that first treated solid $\text{K}[\text{Fe}^{\text{II}}\text{poat}]$ with THF solution of NH_3 which was followed by oxidation with $[\text{Fe}^{\text{III}}\text{Cp}_2]\text{BF}_4$. Both routes afforded the neutral species $[\text{Fe}^{\text{III}}\text{poat}(\text{NH}_3)]$ in similar yields and purity. We also examined treating $[\text{Fe}^{\text{III}}\text{poat}]$ directly with NH_3 to produce $[\text{Fe}^{\text{III}}\text{poat}(\text{NH}_3)]$ but the purity and yields were significantly poorer than the other routes and was therefore not further studied.

Spectroscopic studies of $\text{K}(\text{crypt})[\text{Fe}^{\text{II}}\text{poat}(\text{NH}_3)]$ and $[\text{Fe}^{\text{III}}\text{poat}(\text{NH}_3)]$

The absorbance spectrum of $\text{K}(\text{crypt})[\text{Fe}^{\text{II}}\text{poat}(\text{NH}_3)]$ is featureless in the visible region (Figure 3A). The absorbance spectrum of $[\text{Fe}^{\text{III}}\text{poat}(\text{NH}_3)]$ is dominated by a strong band at $\lambda_{\text{max}} (\epsilon_{\text{M}}) = 382 \text{ nm}$ ($4260 \text{ M}^{-1}\text{cm}^{-1}$, Figure 3-3A) and a shoulder at 513 nm. The EPR spectrum of $\text{K}(\text{crypt})[\text{Fe}^{\text{II}}\text{poat}(\text{NH}_3)]$ showed a valley-shaped signal at $g = 9.1$ that arises from a high spin Fe^{II} center (Figure 3-3B). An axial EPR spectrum was observed for $[\text{Fe}^{\text{III}}\text{poat}(\text{NH}_3)]$ with g -values at ~ 6 and 2 that suggests an $S = 5/2$ spin systems with C_3 symmetry in

solution (Figure 3B). The EPR spectra of the $[\text{Fe}^{\text{II/III}}\text{poat}(\text{NH}_3)]^{-/0}$ complexes are similar to that was observed for the $[\text{Fe}^{\text{II/III}}\text{MST}(\text{NH}_3)]^{-/0}$ complexes, suggesting similarity in the primary coordination sphere around the iron center in the two systems.

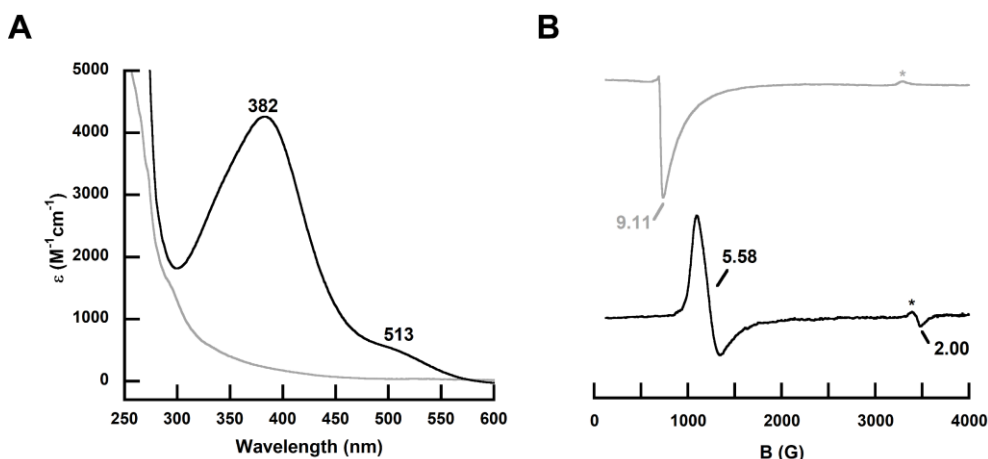


Figure 3-3. (A) Electronic absorption spectra of $\text{K}(\text{crypt})[\text{Fe}^{\text{II}}\text{poat}(\text{NH}_3)]$ (grey) and $[\text{Fe}^{\text{III}}\text{poat}(\text{NH}_3)]$ (black) in DCM. (B) EPR spectra of $\text{K}(\text{crypt})[\text{Fe}^{\text{II}}\text{poat}(\text{NH}_3)]$ (grey, // mode, 10K, 10.0 mM, DMF:THF) and $[\text{Fe}^{\text{III}}\text{poat}(\text{NH}_3)]$ (black, \perp -mode, 77 K, 13 mM, DCM:THF). Asterisks in panel B indicate signals from small amounts of impurities.

Molecular structures of $\text{K}(\text{crypt})[\text{Fe}^{\text{II}}\text{poat}(\text{NH}_3)]$ and $[\text{Fe}^{\text{III}}\text{poat}(\text{NH}_3)]$

The molecular structure of $[\text{K}(\text{crypt})][\text{Fe}^{\text{II}}\text{poat}(\text{NH}_3)]$ was determined using XRD methods (Figure 3-4A). The $[\text{Fe}^{\text{II}}\text{poat}(\text{NH}_3)]^{-}$ complex has a trigonal bipyramidal primary coordination geometry in which the N-atoms of the phosphinic amido groups define the trigonal plane with an avg. $\text{Fe1-N}_{\text{equatorial}}$ bond length of 2.108(2) Å. The exogenous NH_3 ligand is bound to an axial site with an Fe1-N5 bond length of 2.143(2) Å and is trans to the apical N-atom of $[\text{poat}]^{3-}$. The Fe1-N1 bond length of 2.220(1) Å in $[\text{Fe}^{\text{II}}\text{poat}(\text{NH}_3)]^{-}$ is significantly longer than that found in $[\text{Fe}^{\text{II}}\text{poat}]^{-}$ (2.127(4)),²⁵ which is attributed to the trans influence from coordination of NH_3 . A commensurate increase of 0.144 Å was observed for the displacement of the Fe^{II} center from the trigonal plane toward the NH_3 ligand in $[\text{Fe}^{\text{III}}\text{poat}(\text{NH}_3)]^{-}$ compare to $[\text{Fe}^{\text{II}}\text{poat}]^{-}$. The potassium ion is encapsulated by the crypt with an avg. $\text{K}\cdots\text{O}$ distance of 2.825(3) Å and is not interacting with $[\text{Fe}^{\text{II}}\text{poat}(\text{NH}_3)]^{-}$.

The $[\text{poat}]^{3-}$ ligand was designed to support intramolecular H-bonds and the molecular structure of $[\text{Fe}^{\text{II}}\text{poat}(\text{NH}_3)]^-$ demonstrates that this type of non-covalent interaction is possible within the secondary coordination sphere of the Fe center. Three intramolecular H-bonds are present that are formed between the NH_3 ligand and phosphinic amido groups of $[\text{poat}]^{3-}$ (Table 2). As found in $[\text{Fe}^{\text{II}}\text{MST}(\text{NH}_3)]^-$, there is a match between the symmetries of the $[\text{poat}]^{3-}$ ligand with that of the NH_3 ligand to align the N–H groups to form H-bonds with the O-atoms of phosphinic groups. We note that the overall molecular structures of $[\text{Fe}^{\text{II}}\text{poat}(\text{NH}_3)]^-$ and $[\text{Fe}^{\text{II}}\text{MST}(\text{NH}_3)]^-$ are nearly equivalent with the same arrangement of N-atom donors within the primary coordination sphere and the number of H-bonds within secondary coordination sphere. However, the sodium ion interactions in $\text{Na}[\text{Fe}^{\text{II}}\text{MST}(\text{NH}_3)]$ prevents a direct comparison between the two complexes.

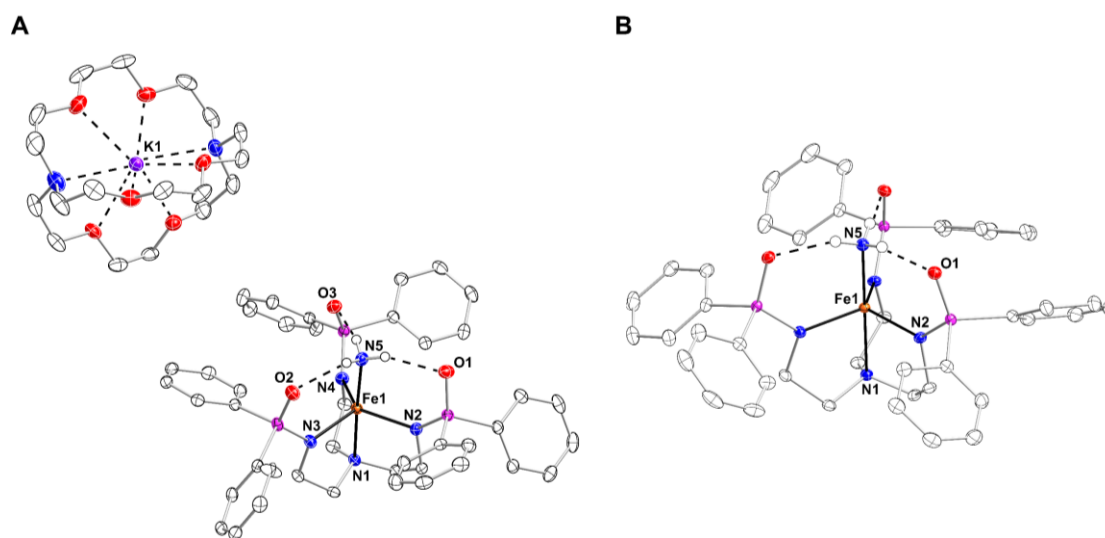


Figure 3-4. Thermal ellipsoid plots of (A) $\text{K}(\text{crypt})[\text{Fe}^{\text{II}}\text{poat}(\text{NH}_3)]$ and (B) $[\text{Fe}^{\text{III}}\text{poat}(\text{NH}_3)]$ determined by XRD methods. Only hydrogen atoms on NH_3 are shown; solvent molecules are omitted for clarity. Ellipsoids are drawn at the 50% probability.

Table 3-1. Selected distances (Å) and angles (°) for [Fe^{III}poat(NH₃)]⁻⁰ and analogous Fe complexes with [MST]³⁻ for comparison.

Complexes	K(crypt)[Fe ^{II} poat(NH ₃)]	Na[Fe ^{II} MST(NH ₃)] ^b	[Fe ^{III} poat(NH ₃)] ^a	[Fe ^{III} MST(NH ₃)] ^b
<i>Distances (Å)</i>				
Fe1–N1	2.220(1)	2.224(1)	2.220 (4)	2.295(3)
Fe1–N2	2.112(1)	2.096(1)	1.998(3)	1.979(2)
Fe1–N3	2.110(1)	2.098(1)	-	-
Fe1–N4	2.104(1)	2.104(1)	-	-
Fe1–N5	2.143(2)	2.145(1)	2.060(4)	2.080(3)
N5···O1	2.884(2)	2.810(2)	2.774(3)	2.881(2)
N5···O2	2.921(2)	2.914(2)	-	-
N5···O3	2.988(2)	2.918(2)	-	-
<i>Angles (°)</i>				
N1–Fe1–N5	177.74(6)	177.58(5)	180.0	180.0

^abond lengths and angles are reported as an average; ^bfrom ref 24.

The molecular structure of [Fe^{III}poat(NH₃)] was determined by XRD methods to find a similar trigonal bipyramidal coordination as discussed for [Fe^{II}poat(NH₃)]⁻. [Fe^{III}poat(NH₃)] crystallized in the *P3* space group with the NH₃ ligand being on a principle C₃-rotational axis with respect to the Fe–N5 bond; in addition, there are two crystallographically different, but chemically equivalent, molecules in the asymmetric unit and we will discuss the average of their metrical parameters (Figures 3-4B, Table 3-1). The Fe–N2 and Fe–N5 bond distances of 1.998(2) and 2.051(1) Å in [Fe^{III}poat(NH₃)] are significantly shorter than those found in its Fe^{II}–NH₃ analogue which is consistent with oxidation of the Fe center.

The similar structures of the neutral [Fe^{III}poat(NH₃)] and [Fe^{III}MST(NH₃)] complexes offer a direct comparison on the structural effects of these two tripodal ligands. There is a small, but statistically significant decrease in the Fe–N5 bond length in [Fe^{III}poat(NH₃)] compared to that in [Fe^{III}MST(NH₃)] (2.060(4) versus 2.080(3) Å) but a larger decrease in the Fe–N1 bond distance (2.220(4) versus 2.295(3) Å). In addition, there is an over 0.1 Å increase in the N5···O1 distances from [Fe^{III}poat(NH₃)] (2.774(3) Å) to [Fe^{III}MST(NH₃)] (2.881(2) Å).

These heavy atom distances are used as a marker to gauge the strength of the H-bond and suggest that stronger intramolecular H-bonds are formed in $[\text{Fe}^{\text{III}}\text{poat}(\text{NH}_3)]$. The stronger $\text{N5-H1}\cdots\text{O1}$ in $[\text{Fe}^{\text{III}}\text{poat}(\text{NH}_3)]$ is attributed to the combination of two effects: 1) the stronger Fe–N5 interaction in $[\text{Fe}^{\text{III}}\text{poat}(\text{NH}_3)]$ should increase the acidity of the ammine ligand which should make it a better H-bond donor, and 2) the stronger dipole in the P=O units of the phosphinic amido group should make it a better H-bond acceptor than the S=O units in the sulfonamido ligand. In addition, for $[\text{Fe}^{\text{III}}\text{poat}(\text{NH}_3)]$ we were able to locate the hydrogen atom on the ammine ligand to give N–H and H \cdots O distances of 0.84(3) Å and 1.98(3) Å which further support the presence of intramolecular H-bonds. Unfortunately, the analogous H-atom in $[\text{Fe}^{\text{III}}\text{MST}(\text{NH}_3)]$ could not be located in the difference map for comparison.

The structural differences between $[\text{Fe}^{\text{III}}\text{poat}(\text{NH}_3)]$ and $[\text{Fe}^{\text{III}}\text{MST}(\text{NH}_3)]$ are supported by solid state vibrational studies using Fourier transform infrared (FT-IR) spectroscopy (Figure 3-5). For $[\text{Fe}^{\text{III}}\text{poat}(\text{NH}_3)]$, the energies of N–H vibrations of the ammine ligand were observed at 3183 and 3109 cm^{-1} while those in $[\text{Fe}^{\text{III}}\text{MST}(\text{NH}_3)]$ were found at 3339 and 3309 cm^{-1} . The significantly lower values in $[\text{Fe}^{\text{III}}\text{poat}(\text{NH}_3)]$ are consistent with weakening of the N–H bond that would arise from a stronger H-bond involving $[\text{poat}]^{3-}$. For comparison, there were no observable vibrational features above 3100 cm^{-1} for $\text{K}[\text{Fe}^{\text{II}}\text{poat}]$ and $\{\text{K}[\text{Fe}^{\text{III}}\text{poat}]_2\}(\text{BF}_4)$ complexes.

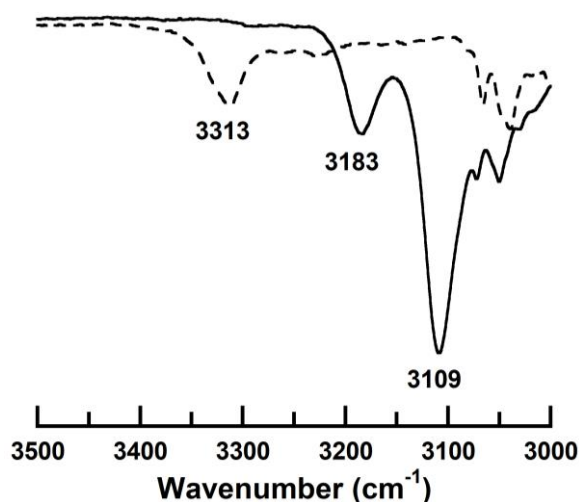


Figure 3-5. Solid state FT-IR spectra of K(crypt)[Fe^{III}poat(NH₃)] (dashed line), and [Fe^{III}poat(NH₃)] (solid line).

Investigation of Fe^{III}–amido Complexes

The coordination of NH₃ to the Lewis acidic Fe^{III} center in [Fe^{III}poat(NH₃)] suggests that we may be able to deprotonate the ammine ligand to prepare the corresponding Fe^{III}–amido complex. We screened a series of non-nucleophilic bases to attempt this deprotonation and the reactions were monitored using UV-vis and EPR spectroscopies. For instance, addition of 1,8-diazabicyclo[5.4.0]undec-7-ene (DBU, $pK_{a,THF} = 16.8$) to [Fe^{III}poat(NH₃)] resulted in only small changes in the optical and axial EPR spectra that indicated the pK_a of the Fe^{III}–NH₃ unit was higher than 16.8. A reaction was observed when the stronger base 1,5,7-triazobicyclo[4.4.0]dec-5-ene (TBD, $pK_{a,THF} = 21.0$) was used and the new species had an absorption band at $\lambda_{max} = 335$ nm (Figure 3-6A). In addition, there was a pronounced change in the EPR properties after deprotonation from the axial EPR spectrum of [Fe^{III}poat(NH₃)] to a rhombic $S = 5/2$ spectrum with g -values at 9.33, 4.80, and 3.88 (Figure 3-6B). This new spectrum is consistent with the formation of a putative [Fe^{III}poat(NH₂)]⁻ species in which the rhombicity would increase because it is no longer C_3 -symmetric. Several attempts to grow single crystals of this deprotonated product to understand its molecular structure were unfortunately unsuccessful.

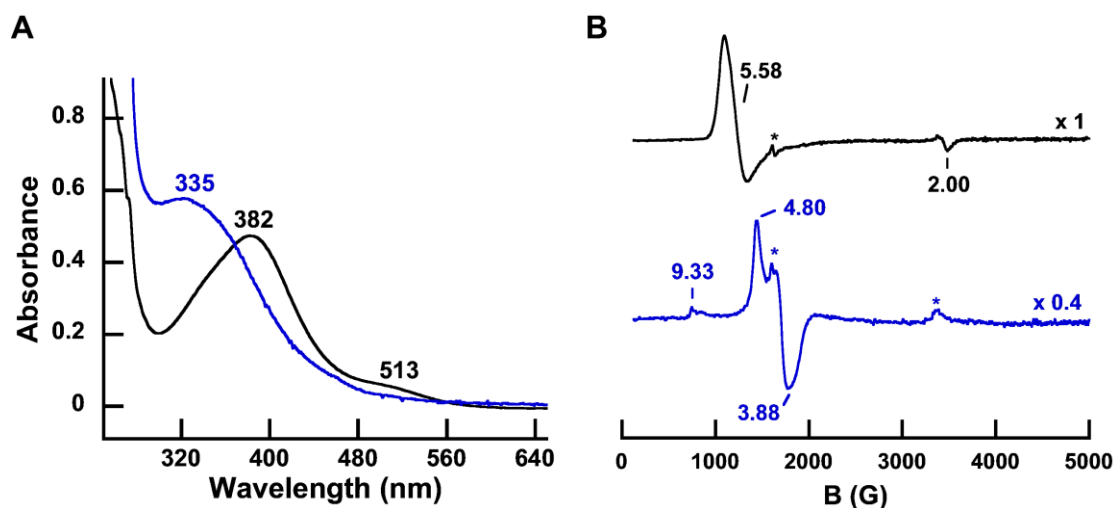
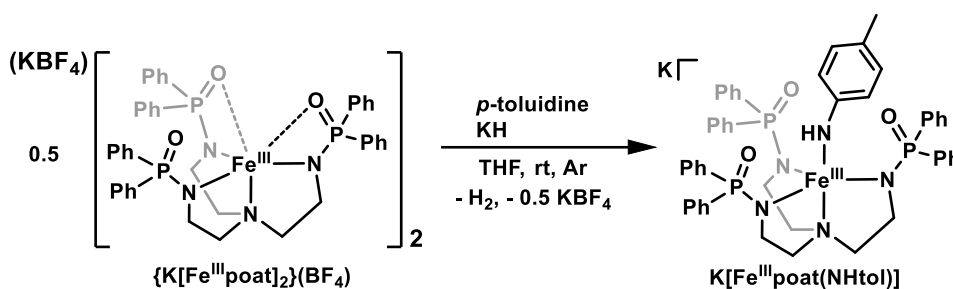


Figure 3-6. (A) Electronic absorption spectra of before (black) and after (blue) addition of excess TBD to 0.13 mM $[\text{Fe}^{\text{III}}\text{poat}(\text{NH}_3)]$ (black) in DCM. (B) EPR spectra of before (black) and after (blue) adding TBD to $[\text{Fe}^{\text{III}}\text{poat}(\text{NH}_3)]$ in DCM:THF (\perp -mode, 77 K, 13 mM). Asterisks in panel B indicate signals from small amounts of impurities.

To further explore the binding of exogenous amido ligands to $[\text{Fe}^{\text{III}}\text{poat}]$, the new $\text{Fe}^{\text{III}}\text{-NHtol}$ complex was prepared, where NHtol is the *p*-toluidine anion. The formation of $\text{Fe}^{\text{III}}\text{-N(H)R}$ complexes are known and nearly all are prepared from the treatment of Fe^{III} complexes with organic azides or N-group transfer reagents.^{26–35} The synthesis of $[\text{Fe}^{\text{III}}\text{poat}(\text{NHtol})]^-$ relied on the deprotonation of *p*-toluidine with KH prior to addition to a suspension of $\{\text{K}[\text{Fe}^{\text{III}}\text{poat}]_2\}^+$, (Scheme 3-3). The reaction mixture immediately changed from orange to dark green which is consistent with formation of an $\text{Fe}^{\text{III}}\text{-NHtol}$ species. For example, the absorption spectrum (Figure 3-7A) of $[\text{Fe}^{\text{III}}\text{poat}(\text{NHtol})]^-$ contains bands at $\lambda_{\text{max}} (\epsilon_M) = 344 (5210)$ and $672 (2040)$ nm that are similar to those observed in the related $[\text{Fe}^{\text{III}}\text{H}_21(\text{NHtol})]^-$ complex ($\lambda_{\text{max}} (\epsilon_M) = 410 (4000)$, $582 (2000)$, where $[\text{H}_21]^{3-}$ is bis[(*N*-*tert*-butylureayl)-*N*-ethyl]-(*N*'-isopropylcarbamoyl-methyl)aminato.³⁰ In addition, the EPR spectrum of $[\text{Fe}^{\text{III}}\text{poat}(\text{NHtol})]^-$ contains signals at *g*-values at 8.8, 5.2, and 3.5 that are also similar to $[\text{Fe}^{\text{III}}\text{H}_21(\text{NHtol})]^-$ and consistent with a rhombic Fe^{III} complex with $S = 5/2$ spin ground state (Figure 3-7B).



Scheme 3-3. Synthesis of $\text{K}[\text{Fe}^{\text{III}}\text{poat}(\text{NHtol})]$.

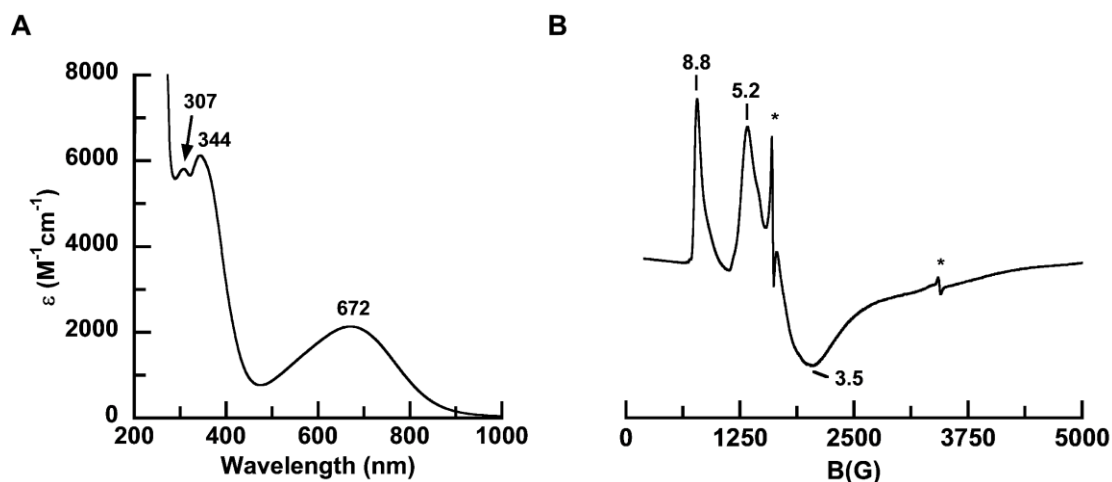


Figure 3-7. (A) Electronic absorption spectrum and (B) EPR spectrum (\perp -mode, 3.9 K) of $\text{K}[\text{Fe}^{\text{III}}\text{poat}(\text{NHtol})]$ in DMF:THF. Asterisks in panel B indicate signals from small amounts of impurities.

The structure of the $\text{K}[\text{Fe}^{\text{III}}\text{poat}(\text{NHtol})]$ complex also aggregated in the crystalline phase with two $[\text{Fe}^{\text{III}}\text{poat}(\text{NHtol})]^-$ complexes interacting with two potassium ions. The molecular structure of the $[\text{Fe}^{\text{III}}\text{poat}(\text{NHtol})]^-$ unit supports our findings in solution of an Fe^{III} -amido complex (Figure 3-8, Table 3-2) with a trigonal bipyramidal geometry similar to that observed for $[\text{Fe}^{\text{III}}\text{poat}(\text{NH}_3)]$. The external amide ligand is bound to the axial position of the Fe^{III} center with an Fe1-N5 bond length of 1.950(3) Å. The Fe1-N1 and avg. $\text{Fe1-N}_{\text{equatorial}}$ bond lengths are 2.401(3) and 2.025(5) Å. The Fe center is displaced 0.454 Å from the plane formed by the deprotonated phosphinic nitrogen atoms which is a significant increase from that found in $[\text{Fe}^{\text{III}}\text{poat}(\text{NH}_3)]$ (0.309 Å). Similar metrical parameters were found when $[\text{Fe}^{\text{III}}\text{poat}(\text{NHtol})]^-$ was compared to the structure of $\text{K}[\text{Fe}^{\text{III}}\text{H}_2\text{1}(\text{NHtol})]$, except that the Fe1-N1 bond length is

significantly longer (0.210 Å) with the [poat]³⁻ ligand. However, a major structural difference was found between the secondary coordination spheres in K[Fe^{III}poat(NHtol)] and K[Fe^{III}H₂1(NHtol)]. Unlike K[Fe^{III}H₂1(NHtol)], there are no H-bond donors in [poat]³⁻ framework and thus there are no interactions with the N5. Furthermore, the O-atoms on P=O groups interact with the potassium ions and do not serve as H-bond acceptors to the amido N–H bond. However, another type of non-covalent interaction: π-π stacking interactions were observed between the aromatic rings on the [NHtol]⁻ ligand and one of the phosphinic amido groups with a centroid-to-centroid distance of 3.617 Å.

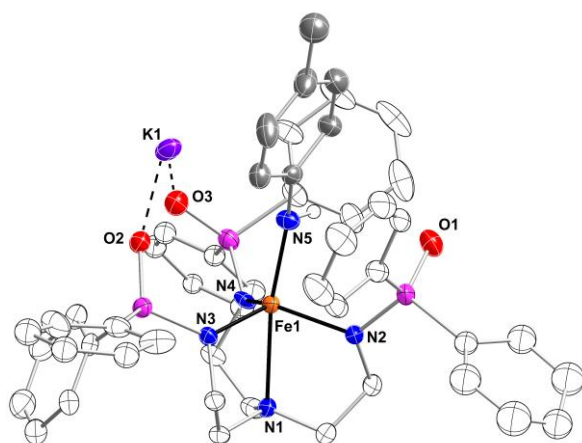


Table 3-2. Selected distances (Å) and angles (°) for K[Fe^{III}poat(NHtol)].

<i>Distances</i>	
Fe1–N1	2.401(3)
Fe1–N2	2.030(3)
Fe1–N3	2.004(3)
Fe1–N4	2.040(3)
Fe1–N5	1.950(3)
<i>Angle</i>	
N1–Fe1–N5	168.79(12)

Figure 3-8. Thermal ellipsoid plots of [Fe^{III}poat(NHtol)]⁻ determined by XRD methods. Only the hydrogen atom on amido ligand is shown. Carbon atoms on the amido ligand are highlighted in grey to distinguish from the other carbon atoms. Ellipsoids are drawn at the 50% probability. Only one orientation of the disordered molecule is shown.

Summary and Conclusion

Ligand modification offers a convenient way to design metal complexes in which control of both the primary and secondary coordination spheres can be achieved. These features are illustrated in the Fe^{II/III} chemistry with the tripodal [poat]³⁻ ligand in which the three phosphinic amido groups provide a strong ligand field *and* control the secondary coordination sphere through the appended P=O groups. Our structural work on the [Fe^{II/III}poat]^{-/0} complexes further illustrate this

ligand's versatility: [poat]³⁻ is a tetradentate ligand in the Fe^{II} complex with a trigonal monopyramidal coordination geometry that is derived from the tripod's N₄ donor set. In Fe^{III} analogue, [poat]³⁻ is a hexadentate ligand with two additional O-atom donors being provided by P=O units of the phosphinic amido groups. These additional donors are presumably needed to help stabilize the increased positive charge at the metal center. In addition, the structures show the propensity of the P=O unit to bind additional metal ions that results in clusters within the crystal lattices. This ability is highlighted by the cluster formed with the neutral Fe^{III} complex whereby two [Fe^{III}poat] molecules are linked by a single potassium ion to form {K[Fe^{III}poat]₂}BF₄.

Experiments aimed at binding an external ligand showed the important role of non-covalent interactions within the secondary coordination on the stability of metal complexes. Attempts to coordinate ammonia to {K[Fe^{II}poat]}₂·3THF were unsuccessful and analysis of isolated solids indicated that no binding had occurred. One possibility is that the interactions of the potassium ion with [Fe^{II}poat]⁻ limited access to the Fe^{II} center which hindered the binding of ammonia. We found that isolating the potassium ion within a cryptand alleviated these interactions and allowed formation of [Fe^{II}poat(NH₃)]⁻ which molecular structure showed a trigonal bipyramidal coordination geometry. The structure also established the presence of three intramolecular H-bonds between the NH groups for the ammine ligand and the P=O groups of the phosphinic amido groups, which was corroborated by results from FT-IR studies. The low one-electron redox potential for Fe^{II}-NH₃ complex allowed for isolation and characterization of [Fe^{III}poat(NH₃)] which also contains three intramolecular H-bonds. A similar H-bond network was found in [Fe^{III}MST(NH₃)] that used a tripodal ligand with sulfonamido groups that led to structural and electrochemical comparisons between the two neutral Fe^{III}-NH₃ complexes. Our findings indicated that [poat]³⁻ is better at stabilizing higher oxidized metal

center that we suggest is because the phosphinic amido groups provide a stronger ligand field *and* form stronger H-bonds.

Attempts to convert $[\text{Fe}^{\text{III}}\text{poat}(\text{NH}_3)]$ to the mono-deprotonated ion $[\text{Fe}^{\text{III}}\text{poat}(\text{NH}_2)]^-$ yielded a relatively unstable species which could not be structural evaluated. We turned to prepare the amido complex $[\text{Fe}^{\text{III}}\text{poat}(\text{NHtOl})]$ which was synthesized by a straightforward route from $\{\text{K}[\text{Fe}^{\text{III}}\text{poat}]_2\}[\text{BF}_4]$ and deprotonated *p*-toluidine. The molecular structure illustrates the formation of the five-coordinate amido complex which is supported by spectroscopic data. Taken together, our studies illustrate the versatility of the $[\text{poat}]^{3-}$ ligand in the preparation of metal complexes; more generally, these results show the utility of incorporating phosphinic amido group in the design of new ligands.

Experimental

General procedure

Unless otherwise stated, all reactions were performed under an argon atmosphere in a Vac Nexus One dry box. Solvents were sparged with argon and dried over columns containing Q-5 and molecular sieves. $\text{Fe}^{\text{II}}(\text{OAc})_2^{36}$ and $[\text{Fe}^{\text{III}}\text{Cp}_2]\text{BF}_4^{37}$ were synthesized following literature procedures and stored under Ar atmosphere at room temperature. Potassium hydride as a 30% suspension in mineral oil was filtered with a medium pore size glass fritted funnel and washed with 10 mL pentane and 10 mL Et_2O five times or until the powder is white, then dried under vacuum and stored under Ar atmosphere at room temperature. NH_3 was purchased from Sigma-Aldrich as 0.4 M THF solution and used without further purification. [2.2.2]-cryptand was purchased from Sigma-Aldrich and dried under vacuum with gentle heat (40-50 °C) for more than 24 hours and stored under Ar atmosphere at room temperature. 1,5,7-triazobicyclo[4.4.0]dec-5-ene and *p*-toluidine was purchased from Sigma-Aldrich and used without further purification. *N,N',N''*-(nitrilotris(ethane-2,1-

diyl))tris(P,P-diphenylphosphinicamide) (H₃poat), {K[Fe^{II}poat]}₂·3THF, {K[Fe^{III}poat]}₂[BF₄], and Na[Fe^{II}MST(NH₃)] were synthesized following our established procedures.^{15,24,25}

Physical methods

All electronic absorption spectra were collected in a 1 cm quartz cuvette with a magnetic spin bar inside. Room temperature electronic absorption spectra for determining extinction coefficients were recorded on a Cary 50 spectrometer. Temperature controlled time dependent electronic absorption spectra were recorded either on a Cary 60 spectrometer equipped with Quantum Northwest TC1 temperature controller and stirrer, or on an 8453E Agilent UV-vis spectrometer equipped with an Unisoku Unispeks cryostat. Cyclic voltammetry was performed using a CHI600C electrochemical analyzer under Ar atmosphere with 0.1 M tetrabutylammonium hexafluorophosphate as the supporting electrolyte. A 2.0 mm glassy carbon electrode was used as working electrode; a Pt wire was used as counter electrode; a Ag wire was used as references electrode with ferrocenium/ferrocene(FeCp₂⁺⁰) couple as internal standard. All potentials are referenced to the FeCp₂⁺⁰ couple. Solid-state IR spectra were collected on a Thermo Scientific Nicolet iS5 FT-IR spectrometer equipped with an iD5 ATR accessory. X-band EPR spectra were recorded as frozen solutions using a Bruker EMX spectrometer equipped with an ER041XG microwave bridge, an Oxford Instrument liquid-helium quartz cryostat, and a dual-mode cavity (ER4116DM).

X-ray crystallography

K(crypt)[Fe^{II}poat(NH₃)]. A yellow crystal of approximate dimensions 0.393 x 0.391 x 0.178 mm was mounted on a glass fiber and transferred to a Bruker SMART APEX II diffractometer. The APEX2³⁸ program package was used to determine the unit-cell parameters and for data collection (20 sec/frame scan

time for a sphere of diffraction data). The raw frame data was processed using SAINT³⁹ and SADABS⁴⁰ to yield the reflection data file. Subsequent calculations were carried out using the SHELXTL⁴¹ program. There were no systematic absences nor any diffraction symmetry other than the Friedel condition. The centrosymmetric triclinic space group $P\bar{1}$ was assigned and later determined to be correct.

The structure was solved by direct methods and refined on F^2 by full-matrix least-squares techniques. The analytical scattering factors⁴² for neutral atoms were used throughout the analysis. Hydrogen atoms on ammonia ligand (N5) were located from a difference-Fourier map and refined (x,y,z and U_{iso}). The remaining hydrogen atoms were included using a riding model. There were two molecules of dichloromethane solvent present. One solvent molecule was disordered and included using multiple components with partial site-occupancy-factors.

Least-squares analysis yielded $wR2 = 0.0943$ and $Goof = 1.023$ for 804 variables refined against 14722 data (0.78 Å), $R1 = 0.0365$ for those 13000 data with $I > 2.0\sigma(I)$.

[Fe^{III}poat(NH₃)]. A violet crystal of approximate dimensions 0.222 x 0.254 x 0.307 mm was mounted on a glass fiber and transferred to a Bruker SMART APEX II diffractometer. The APEX2³⁸ program package was used to determine the unit-cell parameters and for data collection (20 sec/frame scan time for a sphere of diffraction data). The raw frame data was processed using SAINT³⁹ and SADABS⁴⁰ to yield the reflection data file. The systematic absences were consistent with the trigonal space groups $P3$ and $P\bar{3}$. The non-centrosymmetric space group $P3$ was assigned and later determined to be correct.

The structure was solved by direct methods and refined on F^2 by full-matrix least-squares techniques⁴¹. The analytical scattering factors⁴² for neutral

atoms were used throughout the analysis. Hydrogen atoms H(5) and H(10) were located from a difference-Fourier map and refined (x,y,z and U_{iso}). The remaining hydrogen atoms were included using a riding model. There were two molecules of the formula-unit present. Each molecule was located on a three-fold rotation axis. There was one-half molecule of tetrahydrofuran solvent per formula-unit. The solvent was located on a three-fold rotation axis and was disordered. Hydrogen atoms associated with the disordered solvent were not included in the refinement.

Least-squares analysis yielded $wR2 = 0.0630$ and $Goof = 1.050$ for 347 variables refined against 7144 data (0.73 \AA), $R1 = 0.0237$ for those 7061 data with $I > 2.0\sigma(I)$. The absolute structure was assigned by refinement of the Flack parameter⁴³.

K[Fe^{III}poat](NHtol)]. A black crystal of approximate dimensions $0.186 \times 0.223 \times 0.323 \text{ mm}$ was mounted in a cryoloop and transferred to a Bruker SMART APEX II diffractometer. The APEX2³⁸ program package was used to determine the unit-cell parameters and for data collection (25 sec/frame scan time for a sphere of diffraction data). The raw frame data was processed using SAINT³⁹ and SADABS⁴⁰ to yield the reflection data file. Subsequent calculations were carried out using the SHELXTL⁴¹ program. The diffraction symmetry was *mmm* and the systematic absences were consistent with the orthorhombic space group $P2_12_12_1$ that was later determined to be correct.

The structure was solved by direct methods and refined on F^2 by full-matrix least-squares techniques. The analytical scattering factors⁴² for neutral atoms were used throughout the analysis. The amide hydrogen atoms (H5) were located from a difference-Fourier map and refined (x,y,z and U_{iso}) with fixed length. The remaining hydrogen atoms were included using a riding model. Disordered atoms were included as isotropic atoms using multiple components with partial site-occupancy factors.

Least-squares analysis yielded $wR2 = 0.0994$ and $Goof = 1.036$ for 550 variables refined against 12304 data (0.75 Å), $R1 = 0.0426$ for those 10451 data with $I > 2.0\sigma(I)$. The structure was refined as a two-component twin. The absolute structure was assigned by refinement of the Flack⁴³ parameter. There were several high residuals present in the final difference-Fourier map. It was not possible to determine the nature of the residuals although it was probable that dichloromethane was present. The SQUEEZE⁴⁴ routine in the PLATON⁴⁵ program package was used to account for the electrons in the solvent accessible voids.

Table 3-S1. Metric parameters for $K(\text{crypt})[\text{Fe}^{\text{II}}\text{poat}(\text{NH}_3)]$, $[\text{Fe}^{\text{II}}\text{poat}(\text{NH}_3)]$, and $K[\text{Fe}^{\text{II}}\text{poat}(\text{NHtol})]$.

Complex	$K(\text{crypt})[\text{Fe}^{\text{II}}\text{poat}(\text{NH}_3)]$	$[\text{Fe}^{\text{II}}\text{poat}(\text{NH}_3)]$	$K[\text{Fe}^{\text{II}}\text{poat}(\text{NHtol})]$
Empirical Formula	$\text{C}_{60}\text{H}_{79}\text{FeKN}_7\text{O}_9\text{P}_3 \cdot 2(\text{CH}_2\text{Cl}_2)$	$\text{C}_{42}\text{H}_{45}\text{FeN}_5\text{O}_3\text{P}_3 \cdot \frac{1}{2}(\text{C}_4\text{H}_8\text{O})$	$\text{C}_{49}\text{H}_{49}\text{FeKN}_5\text{O}_3\text{P}_3$
Fw	1402.03	852.64	943.79
T (K)	133(2)	88(2)	133(2)
Crystal system	Triclinic	Trigonal	Orthorhombic
Space group	$P\bar{1}$	$P3$	$P2_12_12_1$
a (Å)	14.6635(7)	17.2520(6)	14.8454(10)
b (Å)	14.8610(7)	17.2520(6)	17.4775(11)
c (Å)	18.8343(9)	8.2626(3)	19.4608(13)
α (°)	101.9506(7)	90	90
β (°)	98.9294(7)	90	90
γ (°)	118.7866(7)	120	90
V (Å ³)	3359.9(3)	2129.74(17)	5049.3(6)
Z	2	2	4
δ_{calcd} (Mg/m ³)	1.386	1.330	1.242
GOF on F ²	1.023	1.050	1.036
R1	0.0365	0.0237	0.0426
wR2	0.0943	0.0630	0.0994
CCDC#	2053479	2053478	2053481

Synthesis of $K[Fe^{II}poat]$

To a clear colorless solution of H_3poat (0.200 g, 0.268 mmol) in 4 mL THF, KH (33.4 mg, 0.833 mmol) was added and stirred for 30 minutes until gas evolution ceased. $Fe(OAc)_2$ (47.8 mg, 0.275 mmol) was added to the reaction mixture, resulting in immediate change to a yellow heterogeneous solution. After stirring for 20 minutes, insoluble salt ($KOAc$) was filtered off through a medium pore size frit, and the resulting clear yellow solution was layered under Et_2O . Yellow x-ray quality crystals were obtained on the following day (217.2 mg, 96.5%). Note that the reaction time of this experiment is crucial for a good yield due to solubility of the product. Elemental analysis calcd for $C_{42}H_{42}FeKN_4O_3P_3$: C, 60.15; H, 5.05; N, 6.7 %, found: C, 60.2; H, 4.91; N, 6.7 %. FT-IR (diamond ATR, cm^{-1}): 3066, 3045, 3004, 2952, 2896, 2831, 2805, 1977, 1890, 1824, 1774, 1673, 1612, 1589, 1571, 1482, 1462, 1443, 1432, 1364, 1346, 1334, 1292, 1271, 1264, 1234, 1181, 1153, 1136, 1130, 1115, 1101, 1066, 1041, 1027, 1020, 998, 966, 951, 919, 910, 852, 802, 785, 746, 716, 695, 619, 578, 571, 569, 561, 554. EPR (X-band, \parallel -mode, 1:1 DMF:THF, 10K): $g = 9.10$.

Synthesis of $\{K[Fe^{III}poat]_2\}[BF_4]$

$K[Fe^{II}poat]$ (0.446 g, 0.532 mmol) was suspended in 4 mL THF. In a separate vial, $FcBF_4$ (0.146 g, 0.536 mmol) was dissolved in 0.5 mL MeCN and added to the suspension to yield an immediate color change to clear red solution. As the reaction was stirred for 2 hours, orange precipitate formed over time. The orange solid was collected through a medium pore size frit and dried under vacuum (0.393 g, 92.3%). Crystals can be obtained by redissolving the complex in MeCN and layering under Et_2O , or by redissolving the complex in DCM and layering under pentane. Elemental analysis calcd for $C_{42}H_{42}FeN_4O_3P_3 \cdot 2KBF_4$: C, 48.0; H, 4.0; N, 5.3 %, found: C, 47.90; H, 4.0; N, 5.3 %. FT-IR (diamond ATR, cm^{-1}): 3073, 3052, 2961, 2893, 2853, 1977, 1897, 1821, 1779, 1676, 1615, 1591, 1571, 1483, 1447, 1435, 1306, 1278, 1194, 1180, 1121, 1090, 1050,

1034, 1025, 996, 979, 958, 950, 913, 618, 591, 589, 583, 574, 569, 565, 558, 556. EPR (X-band, \perp -mode, MeCN, 77K): $g = 7.01, 5.52, 3.27, 1.90$. UV-vis $\lambda_{\max}(\text{MeCN})/\text{nm}$ ($\epsilon, \text{M}^{-1}\text{cm}^{-1}$): 335 (4900), 385 (5800).

Synthesis of K(crypt)[Fe^{II}poat(NH₃)]

To K[Fe^{II}poat] (0.462 g, 0.551 mmol), 11 mL (excess) of 0.4 M NH₃ in THF was added via syringe and stirred for 5 minutes, resulting a clear intense yellow solution. After all crystals were dissolved, [2.2.2]-cryptand (0.219 g, 0.582 mmol) was added to slowly precipitate yellow solid product. The solid was collected through a medium pore size frit, washed with 2 mL THF, dried under vacuum, redissolved in DCM, and layer under pentane. Dark yellow polygon shaped x-ray quality crystals (0.616 g, 90.7 %) were obtained the following day. Elemental analysis calcd for C₆₀H₈₁FeKN₇O₉P₃·2DCM: C, 53.1; H, 6.1; N, 7.0 %, found: C, 53.1; H, 6.2; N, 6.8 %. FT-IR (diamond ATR, cm⁻¹): 3310 (NH), 3066, 3002, 2965, 2952, 2871, 2820, 2801, 1980, 1909, 1821, 1811, 1774, 1674, 1635, 1614, 1589, 1572, 1490, 1480, 1474, 1458, 1445, 1431, 1363, 1353, 1301, 1286, 1276, 1258, 1241, 1235, 1226, 1180, 1166, 1151, 1111, 1097, 1084, 1066, 1049, 998, 971, 945, 934, 851, 833, 812, 746, 730, 721, 715, 703, 696, 618, 602, 594, 584, 578, 573, 569, 563, 557, 554. EPR (X-band, \parallel -mode, 1:1 DMF:THF, 10K): $g = 9.11$.

Synthesis of [Fe^{III}poat(NH₃)]

K(crypt)[Fe^{II}poat(NH₃)] (0.201 g, 0.163 mmol) was suspended in 4 mL THF. In a separate vial, FcBF₄ (45.3 mg, 0.166 mmol) was dissolved in 0.5 mL MeCN and added to the suspension, resulting in immediate color change to red and clear solution. As the reaction was stirred for 2 hours, red precipitate formed over time. 10 drops of Et₂O were added and stirred for an additional hour to help precipitate more of the red solid product. The red solid was collected through a medium pore size frit, washed with 2 mL THF, 10 mL pentane, and

10 mL Et₂O, then dried under vacuum (99.6 mg, 74.7 %). Red needle shaped x-ray quality crystals were obtained by redissolving the red solid in DCM and layering under pentane. Elemental analysis calcd for C₄₂H₄₅FeN₅O₃P₃·2.5DCM: C, 51.95; H, 4.9; N, 6.8 %, found: C, 52.4; H, 4.8; N, 7.0 %. FT-IR (diamond ATR, cm⁻¹): 3182 (NH), 3072 (NH), 3108, 3050, 2977, 2910, 2890, 2858, 2848, 1980, 1900, 1830, 1819, 1783, 1688, 1671, 1617, 1590, 1572, 1482, 1471, 1465, 1446, 1441, 1434, 1356, 1347, 1313, 1307, 1289, 1273, 1232, 1182, 1172, 1157, 1146, 1118, 1107, 1101, 1067, 1028, 998, 995, 964, 932, 882, 849, 824, 801, 763, 757, 747, 720, 700, 696, 620, 614, 587, 577, 568, 562, 559, 553. EPR (X-band, ⊥-mode, 1:1 DCM:THF, 77K): g = 5.58, 2.00. UV-vis λ_{max}(DCM)/nm (ε, M⁻¹cm⁻¹): 382(4300), 513(sh).

Synthesis of K[Fe^{III}poat(NHtol)]

p-toluidine (13.7 mg, 0.128 mmol) was dissolved in 2 mL THF and KH (5.4 mg, 0.13 mmol) was added to the solution, resulting in immediate formation of bubble. After stirring for an hour or until all bubble ease, the pale yellow reaction solution was filtered and added into orange solid of {K[Fe^{III}poat]₂}[BF₄] (0.100 g, 0.125 mmol), resulting in immediate color change to a dark green solution. After stirring for two hours, the reaction solution was dried under vacuum to obtain green solid product (0.111 g, 94.1%). X-ray quality crystals were obtained by redissolving the green solid in DCM and layering under pentane. Elemental analysis calcd for C₄₉H₅₀FeKN₅O₃P₃·DCM: C, 58.3; H, 5.1; N, 6.8%, found: C, 58.0; H, 4.8; N, 6.6%. FT-IR (diamond ATR, cm⁻¹): 3049 (NH), 2841, 1603, 1516, 1500, 1481, 1435, 1284, 1171, 1114, 1065, 1026, 958, 819, 793, 748, 717, 694. EPR (X-band, ⊥-mode, 1:2 DMF:THF, 3.9K): g = 8.82, 5.20, 3.47. UV-vis λ_{max}(DCM)/nm (ε, M⁻¹cm⁻¹): 363(5210), 672(2040).

Deprotonation of [Fe^{III}poat(NH₃)]

Triazabicyclodecene (TBD, $pK_a = 21$ in THF) was used as base to deprotonate the complex. To monitor the absorption feature changes during the deprotonation process, a ~ 0.2 mM stock solution of [Fe^{III}poat(NH₃)] was prepared in DCM. 3 mL of above complex solution was transferred into a 1 cm pathlength cuvette with stir bar using syringe. The cuvette was sealed with a rubber septum and brought outside the glovebox to spectrometer. Stock solution of TBD was prepared with concentration of ~ 75 mM. 100 μ L of base stock solution (10 equiv.) was injected using a 250 μ L airtight locking syringe with constant stirring.

To monitor the EPR signal changes during the deprotonation process, a ~ 10 mM stock solution of [Fe^{III}poat(NH₃)] was prepared in DCM:THF. Two samples for comparing before and after addition of base were prepared using the same complex stock solution. First, 250 μ L of complex stock solution was transferred into an EPR tube using syringe. The tube was sealed with a rubber septum and brought outside the glovebox to spectrometer. Second, 600 μ L of complex stock solution was added into 10 equivalents of TBD solid and stirred for 1 hour. 250 μ L of reaction solution was transferred into an EPR tube using syringe. The tube was sealed with a rubber septum and brought outside the glovebox to spectrometer.

References

- (1) O'Brien, J. R.; Schuller, D. J.; Yang, V. S.; Dillard, B. D.; Lanzilotta, W. N. *Biochemistry* **2003**, *42* (19), 5547–5554.
- (2) Vojtěchovský, J.; Chu, K.; Berendzen, J.; Sweet, R. M.; Schlichting, I. *Biophys. J.* **1999**, *77* (4), 2153–2174.
- (3) Gordon, Z.; Drummond, M. J.; Matson, E. M.; Bogart, J. A.; Schelter, E. J.; Lord, R. L.; Fout, A. R. *Inorg. Chem.* **2017**, *56* (9), 4852–4863.
- (4) Moore, C. M.; Szymczak, N. K. *Chem. Sci.* **2015**, *6* (6), 3373–3377.
- (5) Jones, J. R.; Ziller, J. W.; Borovik, A. S. *Inorg. Chem.* **2017**, *56* (3), 1112–1120.

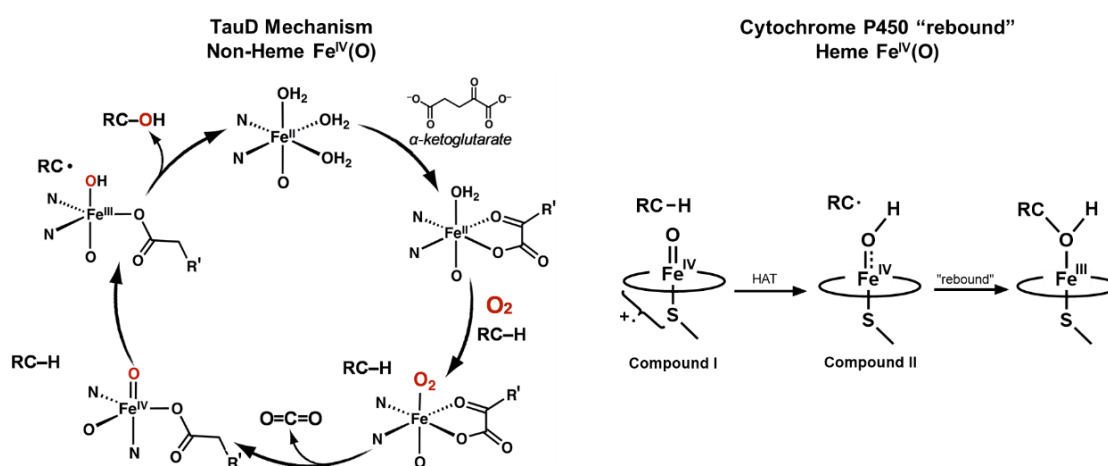
- (6) Cook, S. A.; Borovik, A. S. *Acc. Chem. Res.* **2015**, *48* (8), 2407–2414.
- (7) Shook, R. L.; Borovik, A. S. *Inorg. Chem.* **2010**, *49* (8), 3646–3660.
- (8) Borovik, A. S. *Acc. Chem. Res.* **2005**, *38* (1), 54–61.
- (9) MacBeth, C. E.; Gupta, R.; Mitchell-Koch, K. R.; Young, V. G.; Lushington, G. H.; Thompson, W. H.; Hendrich, M. P.; Borovik, A. S. *J. Am. Chem. Soc.* **2004**, *126* (8), 2556–2567.
- (10) Schwarz, A. D.; Herbert, K. R.; Paniagua, C.; Mountford, P. *Organometallics* **2010**, *29* (18), 4171–4188.
- (11) Schwarz, A. D.; Chu, Z.; Mountford, P. *Organometallics* **2010**, *29* (5), 1246–1260.
- (12) Park, Y. J.; Ziller, J. W.; Borovik, A. S. *J. Am. Chem. Soc.* **2011**, *133* (24), 9258–9261.
- (13) Park, Y. J.; Cook, S. A.; Sickerman, N. S.; Sano, Y.; Ziller, J. W.; Borovik, A. S. *Chem. Sci.* **2013**, *4* (2), 717–726.
- (14) Cook, S. A.; Ziller, J. W.; Borovik, A. S. *Inorg. Chem.* **2014**, *53* (20), 11029–11035.
- (15) Oswald, V. F.; Lee, J. L.; Biswas, S.; Weitz, A. C.; Mittra, K.; Fan, R.; Li, J.; Zhao, J.; Hu, M. Y.; Alp, E. E.; Bominaar, E. L.; Guo, Y.; Green, M. T.; Hendrich, M. P.; Borovik, A. S. *J. Am. Chem. Soc.* **2020**, *142* (27), 11804–11817.
- (16) Olmstead, M. M.; Sigel, G.; Hope, H.; Xu, X.; Power, P. P. *J. Am. Chem. Soc.* **1985**, *107* (26), 8087–8091.
- (17) Chetcuti, P. A.; Liégard, A.; Rihs, G.; Rist, G.; Schweiger, A. *Helv. Chim. Acta* **1991**, *74* (7), 1591–1599.
- (18) Sellmann, D.; Soglowek, W.; Knoch, F.; Ritter, G.; Dengler, J. *Inorg. Chem.* **1992**, *31* (18), 3711–3717.
- (19) Fox, D. J.; Bergman, R. G. *J. Am. Chem. Soc.* **2003**, *125* (30), 8984–8985.
- (20) Bowman, A. C.; Bart, S. C.; Heinemann, F. W.; Meyer, K.; Chirik, P. J. *Inorg. Chem.* **2009**, *48* (13), 5587–5589.
- (21) Lee, Y.; Mankad, N. P.; Peters, J. C. *Nat Chem* **2010**, *2* (7), 558–565.
- (22) Yu, Y.; Brennessel, W. W.; Holland, P. L. *Organometallics* **2007**, *26* (13), 3217–3226.
- (23) Saouma, C. T.; Moore, C. E.; Rheingold, A. L.; Peters, J. C. *Inorg. Chem.* **2011**, *50* (22), 11285–11287.
- (24) Sickerman, N. S.; Peterson, S. M.; Ziller, J. W.; Borovik, A. S. *Chem. Commun.* **2014**, *50* (19), 2515–2517.
- (25) Sun, C.; Oswald, V. F.; Hill, E. A.; Ziller, J. W.; Borovik, A. S. *Dalt. Trans.* **2021**, Just accepted.
- (26) Spasyuk, D. M.; Carpenter, S. H.; Kefalidis, C. E.; Piers, W. E.; Neidig, M. L.; Maron, L. *Chem. Sci.* **2016**, *7* (9), 5939–5944.
- (27) Iovan, D. A.; Betley, T. A. *J. Am. Chem. Soc.* **2016**, *138* (6), 1983–1993.
- (28) Eckert, N. A.; Smith, J. M.; Lachicotte, R. J.; Holland, P. L. *Inorg. Chem.* **2004**, *43* (10), 3306–3321.

- (29) Nieto, I.; Ding, F.; Bontchev, R. P.; Wang, H.; Smith, J. M. *J. Am. Chem. Soc.* **2008**, *130* (Copyright (C) 2011 American Chemical Society (ACS). All Rights Reserved.), 2716–2717.
- (30) Lucas, R. L.; Powell, D. R.; Borovik, A. S. *J. Am. Chem. Soc.* **2005**, *127* (33), 11596–11597.
- (31) Saouma, C. T.; Muller, P.; Peters, J. C.; Müller, P.; Peters, J. C. *J. Am. Chem. Soc.* **2009**, *131* (30), 10358–10359.
- (32) Leeladee, P.; Jameson, G. N. L.; Siegler, M. A.; Kumar, D.; De Visser, S. P.; Goldberg, D. P. *Inorg. Chem.* **2013**, *52* (8), 4668–4682.
- (33) Klinker, E. J.; Jackson, T. A.; Jensen, M. P.; Stubna, A.; Juhasz, G.; Bominaar, E. L.; Muenck, E.; Que, L. J. **2006**, *45* (44), 7394–7397.
- (34) Wilding, M. J. T.; Iovan, D. A.; Betley, T. A. *J. Am. Chem. Soc.* **2017**, *139* (34), 12043–12049.
- (35) Verma, A. K.; Nazif, T. N.; Achim, C.; Lee, S. C. **2000**, No. 10, 11013–11014.
- (36) Rhoda, R. N.; Fraioli, A. V.; Talor, W. L.; Kleinberg, J. *Inorg. Synth.* **1953**, *4*, 159–161.
- (37) Connelly, N. G.; Geiger, W. E. *Chem. Rev.* **1996**, *96* (2), 877–910.
- (38) APEX3 Version 2014.1-1, Bruker AXS Inc: Madison, WI 2014.
- (39) SAINT Version 8.34a, Bruker AXS Inc: Madison, WI 2013.
- (40) Sheldrick, G. M. SADABS Version 2014/5, Bruker AXS, Inc: Madison 2014.
- (41) Sheldrick, G. M. SHELXTL Version 2014/7, Bruker AXS, Inc: Madison 2014.
- (42) Wilson, A. J. C.; Geist, V. *Cryst. Res. Technol.* **1993**, *28* (1), 110.
- (43) Parson, S.; Flack, H. D.; Wagner, T. *Acta Crystallogr. Sect. B Struct. Crystallogr. Cryst. Chem.* **2013**, *69*, 249–259.
- (44) Spek, A. L. *Acta Crystallogr. Sect. C Struct. Chem.* **2015**, *71* (1), 9–18.
- (45) Spek, A. L. *Acta Crystallogr. Sect. D Biol. Crystallogr.* **2009**, *65* (2), 148–155.

Chapter 4 – Reactivity of Fe^{IV}-oxido complex in C₃-symmetric phosphoryl amido tripodal framework

Introduction

High-valent metal-oxido units in the active sites of proteins are important intermediates in C–H bond activation. For example, an Fe^{IV}-oxido moiety is identified as the key intermediate responsible for cleaving strong C–H bonds (>100 kcal/mol) of substrates in heme (e.g. cytochrome P450^{1–4}) and non-heme (e.g. taurine dioxygenase (TauD)^{5–8}) enzymes (Scheme 4-1). An important property of the non-heme Fe dioxygenase intermediate is its S = 2 spin ground state.^{5,8–10} Although there are now examples of synthetic Fe^{IV}-oxido complexes for better understanding of the responsible intermediates, most of these complexes have S = 1 spin ground states,^{11–13} with only very few examples of S = 2 spin ground states Fe^{IV}-oxido complexes.^{14–21} Therefore, study of synthetic high spin Fe^{IV}-oxido complexes and exploration of their properties and reactivities are still needed.



Scheme 4-1. Mechanism of TauD (left) and Cytochrome P450 "rebound" (right).

The microenvironment (or secondary coordination sphere) within the protein active sites is now known to have significant effects on modulating

function.^{22–24} Non-covalent interactions are the dominant forces that modulate the microenvironment.^{25–33} Biomimetic small-molecule metal complexes are often designed to investigate the effects of the covalent interactions (primary coordination sphere) on function. However, interactions within the secondary coordination sphere, such as hydrogen bonds (H-bonds), also contribute to the overall properties of metal complexes. Much less is known about secondary coordination sphere effects than primary coordination sphere ones. The Borovik lab specializes in using C_3 -symmetric tripodal ligand frameworks to regulate non-covalent interactions within the secondary coordination sphere that allow for modulation of the properties and reactivities of metal complexes.^{34–40}

Development of $Fe^{IV}(O)$ complexes in the Borovik lab

There are several examples in the Borovik lab that demonstrate the power of C_3 -symmetric tripodal ligand frameworks. For instance, the $[H_3buea]^{3-}$ ligand framework that has three N–H in urea arms can serve as H-bond donors and facilitate stabilization of high-valent metal-oxido complexes;^{17,41–43} the $[poat]^{3-}$ ligand framework has three P=O unit in phosphinic amido arms that can serve as H-bond acceptors or create an axillary metal binding site (Figure 4-1).³⁹ Both of these two ligand frameworks are tri-anionic and have illustrated their capability to support an Fe^{IV} -oxido moiety (Figure 4-2).

However, when looking into the reactivity of these Fe^{IV} -oxido complexes, their ability to perform C–H bond activation does not resemble their biological counterparts. $[Fe^{IV}H_3buea(O)]^-$ was relatively stable that allowed isolation of single crystals for structural characterization. This complex was observed to be room temperature stable for months in DMSO, and the solid can be stored for years under Ar atmosphere at room temperature.^{17,44} In addition, it is unreactive towards 9,10-dihydroanthracene.⁴⁵ Although $[Fe^{IV}poat(O)]^-$ was less stable, it still lacked reactivity toward external substrates. We argue that this is due to the steric congestion of $[poat]^{3-}$, as the space fill model of the $[Fe^{II}poat(H_2O)]^-$

complex illustrates (Figure 4-2). The phenyl rings of phosphinic amido groups surround the Fe^{II}-aqua moiety and could potentially prevent substrates from readily approaching the Fe center. Therefore, a different ligand, [pop]³⁻, that has phosphoryl amido arms was designed and investigated (Figure 4-1).

The phosphoryl amido groups in [pop]³⁻ have similar P=O units as [poat]³⁻ that can serve as H-bond acceptors, but the additional oxygen linkages allow more flexibility in the phosphoryl amido arms. This could potentially provide a more exposed metal center to allow substrates to approach and promote reactivity. This chapter focuses on the characterization of the new [Fe^{IV}POP(O)]⁻ complex and discusses its reactivity in comparison to previous Fe^{IV}-oxido complexes.

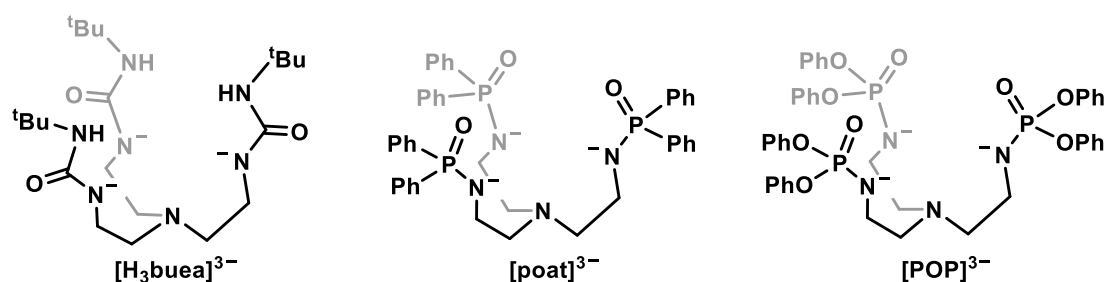


Figure 4-1. Three C₃-symmetric tripodal ligand frameworks developed in the Borovik lab: [H₃buea]³⁻, [poat]³⁻, and [POP]³⁻.

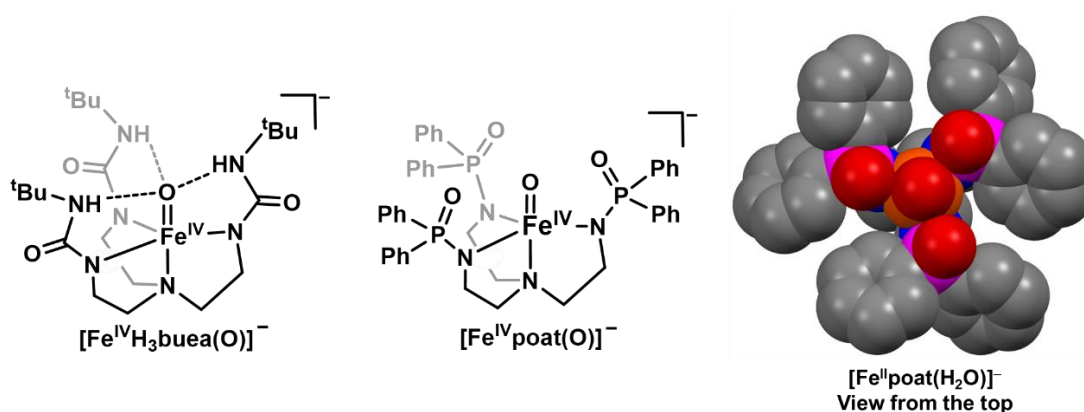


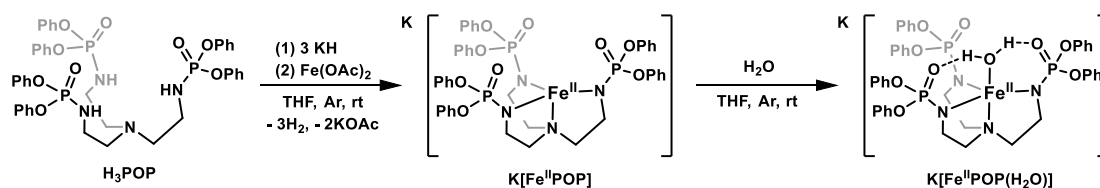
Figure 4-2. Illustration of [Fe^{IV}H₃buea(O)]⁻, [Fe^{IV}poat(O)]⁻, and space fill model of [Fe^{II}poat(H₂O)]⁻ (View from the top).

Result and Discussion

Preparations of Fe^{II} complexes

The K[Fe^{II}POP] complex was prepared by treating the precursor ligand H₃POP with 3 equiv. of KH in tetrahydrofuran (THF) for 1 hour, and then allowing the resulting mixture to react with Fe^{II}(OAc)₂ for another hour (Scheme 4-2). After filtration, the solvent was removed under reduced pressure to produce a white powder in yields >80 %. The parallel-mode electron paramagnetic resonance (EPR) spectrum of K[Fe^{II}POP] in the presence of 2 equiv. 18-crown-6 (18C6) had a valley shaped signal with a g-value of 9.3 that is indicative of an S = 2 spin ground state, consistent with a high spin Fe^{II} center (Figure 4-4, B).

Unlike the K[Fe^{II}poat] complex described in Chapter 3, K[Fe^{II}POP] complex could not be cleanly isolated, possibly due to long recrystallization time that lead to partial coordination of adventitious water to form K[Fe^{II}POP(H₂O)]. Multiple attempts to crystallize K[Fe^{II}POP] in different combinations of THF, dichloromethane (DCM), acetonitrile (MeCN), benzene, diethyl ether (Et₂O), and pentane all resulted in K[Fe^{II}POP(H₂O)] as the crystalline product. Therefore, K[Fe^{II}POP(H₂O)] was independently prepared and used as the starting synthon for further studies. The synthesis of K[Fe^{II}POP(H₂O)] was performed in a similar manner as the K[Fe^{II}POP] complex with the following modifications: after reacting H₃POP with 3 equiv. of KH and Fe^{II}(OAc)₂, H₂O was added into the reaction mixture and stirred for 10 min (Scheme 4-2). The mixture was filtered, and the filtrate was layered under pentane to obtain X-ray quality crystals (>70%). Unlike the K[Fe^{II}POP] complex, EPR measurements of K[Fe^{II}POP(H₂O)] showed no observable feature.



Scheme 4-2. Synthesis of K[Fe^{II}POP] and K[Fe^{II}POP(H₂O)].

Structural Properties of K[Fe^{II}POP(H₂O)]

The molecular structure of K[Fe^{II}POP(H₂O)] was investigated using X-ray diffraction (XRD) methods. In crystalline phase, K[Fe^{II}POP(H₂O)] aggregates as the cluster {K[Fe^{II}POP(H₂O)]}₂ with $P\bar{1}$ space group (Figure 4-3). Similar to complexes in the [poat]³⁻ ligand framework, interactions between the potassium ion and P=O unit of [POP]³⁻ ligand were observed. The two [Fe^{II}POP(H₂O)]⁻ complexes are linked through two potassium ions via the oxygen atoms in phosphoryl amido arms and the aqua ligands. Each Fe^{II} center is five-coordinate in trigonal bipyramidal geometry. The Fe1–N1 and average Fe1–N_{equatorial} bond lengths are 2.214(2) and 2.063(2) Å, and the average N1–Fe1–N_{equatorial} angle is 81.25(6)°. The Fe^{II} center is displaced 0.313 Å from the plane formed by the deprotonated phosphoryl nitrogen atoms toward the aqua ligand. The aqua ligand is bound to the Fe^{II} center in the axial position with an Fe1–O1 bond length of 2.205(1) Å, which is relatively longer than other reported Fe^{II}-aqua complexes in trigonal bipyramidal geometry.^{46,47} This elongation could possibly be due to the interaction between the potassium counter ion and the aqua ligand, which could weaken the Fe1–O1 bond resulting in longer bond length. The P=O units in the phosphoryl amido groups of [POP]³⁻ were designed to promote intramolecular H-bonding interactions in the secondary coordination sphere around the metal center by serving as H-bond acceptors. The molecular structure of K[Fe^{II}POP(H₂O)] demonstrated that two intramolecular H-bonds are formed between the aqua ligand and P=O units in two of the three phosphoryl amido arms with O1...O2 distance of 2.649(2) and O1...O3 distance of 2.728(2).

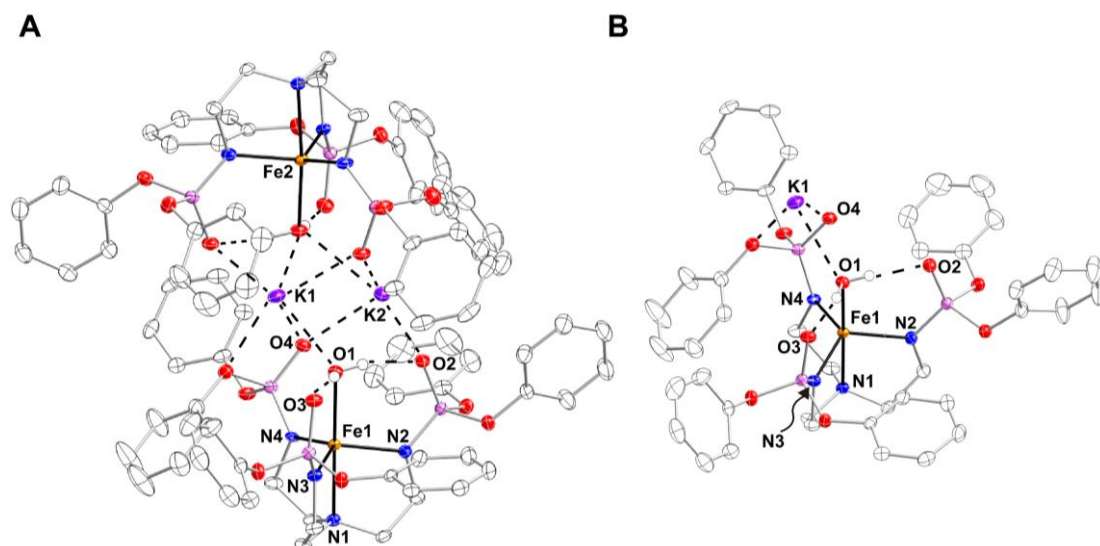


Figure 4-3. Molecular structure of (A) $\{K[Fe^{II}POP(H_2O)]\}_2$ as the aggregate and (B) view of $K[Fe^{II}POP(H_2O)]$ fragment determined by XRD methods. Only hydrogen atoms on H_2O ligand are shown. Ellipsoids are drawn at 50% probability.

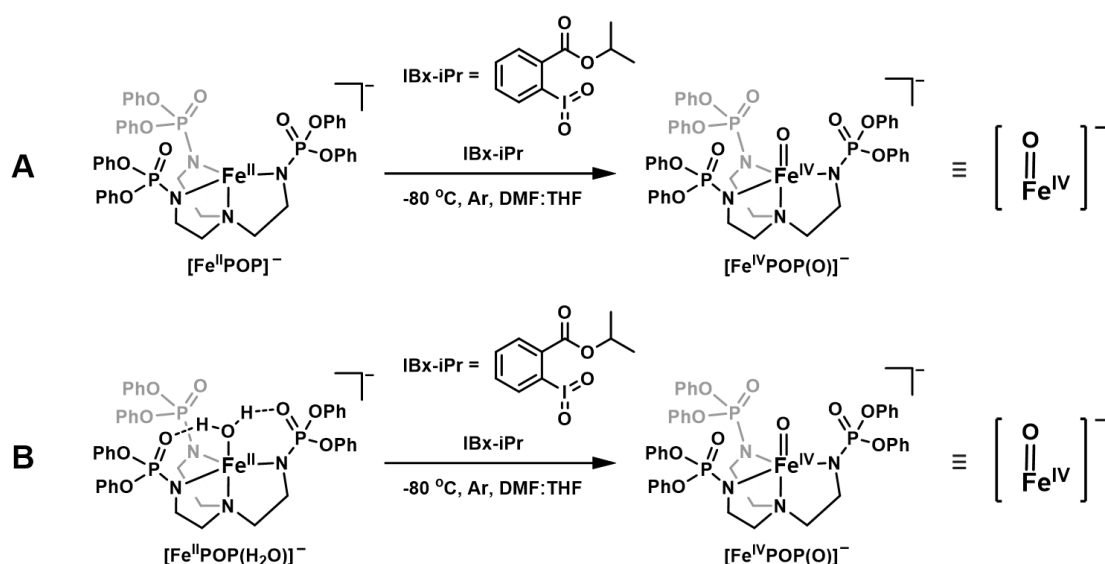
Table 4-1. Selected Distances (\AA) and angles ($^\circ$) for $K[Fe^{II}POP(H_2O)]$.

Complex	$K[Fe^{II}POP(H_2O)]$
<i>Distances (\AA)</i>	
Fe1–N1	2.214(2)
Fe1–N2	2.068(2)
Fe1–N3	2.064(2)
Fe1–N4	2.058(2)
Fe1–O1	2.205(1)
O1...O2	2.649(2)
O1...O3	2.728(2)
K1...O1	2.785(2)
K1...O4	2.664(1)
<i>Bond Angles ($^\circ$)</i>	
N1–Fe1–N2	81.60(6)
N1–Fe1–N3	80.74(6)
N1–Fe1–N4	81.40(6)
N2–Fe1–N3	116.79(6)
N2–Fe1–N4	126.76(6)
N3–Fe1–N4	109.58(6)

Preparation and Properties of $[Fe^{IV}POP(O)]^-$

The initial studies were performed using a similar procedures previously reported for $[Fe^{IV}poat(O)]^-$.³⁹ The $[Fe^{IV}POP(O)]^-$ complex was generated by adding 1.2 equiv. of IBX-iPr to $K[Fe^{II}POP]$ in the presence of 2.5 equiv. of 18-

crown-6 (18C6) (Scheme 4-3A). The reaction was monitored using UV-vis and EPR spectroscopies (Figure 4-4A1). The UV-vis spectrum of the reaction product has $\lambda_{\text{max}}/\text{nm}$ ($\epsilon/\text{M}^{-1}\text{cm}^{-1}$) = 360 (2500), 500 (sh), and 900 (90), where the low energy 900 nm feature is consistent with the signature d-d transitions observed in synthetic non-heme Fe^{IV} -oxido species.^{16,17,19,39,48} The parallel-mode EPR spectrum of the reaction contains a $g = 8.2$ feature corresponding to an $S = 2$ Fe^{IV} oxido species (Figure 4-4B). However, as discussed before, due to the undetermined purity of $\text{K}[\text{Fe}^{\text{II}}\text{POP}]$, $\text{K}[\text{Fe}^{\text{II}}\text{POP}(\text{H}_2\text{O})]$ was used instead as the starting complex for generation of $[\text{Fe}^{\text{IV}}\text{POP}(\text{O})]^-$ in all further studies (Scheme 4-3B). To verify that the aqua ligand does not affect the formation or properties of $[\text{Fe}^{\text{IV}}\text{POP}(\text{O})]^-$, UV-vis and EPR measurements were performed to confirm the identical species was produced from either Fe^{II} complex. The only difference observed when using $\text{K}[\text{Fe}^{\text{II}}\text{POP}(\text{H}_2\text{O})]$ instead of $\text{K}[\text{Fe}^{\text{II}}\text{POP}]$ as the starting complex is the extinction coefficient determined for generated $[\text{Fe}^{\text{IV}}\text{POP}(\text{O})]^-$ is higher, consistent with the undetermined purity of $\text{K}[\text{Fe}^{\text{II}}\text{POP}]$ (Figure 4-4A2).



Scheme 4-3. Generation of $[\text{Fe}^{\text{IV}}\text{POP}(\text{O})]^-$ using $[\text{Fe}^{\text{II}}\text{POP}]^-$ as the starting complex. Identical UV-vis and EPR results were observed when using $[\text{Fe}^{\text{II}}\text{POP}(\text{H}_2\text{O})]^-$ as the starting complex.

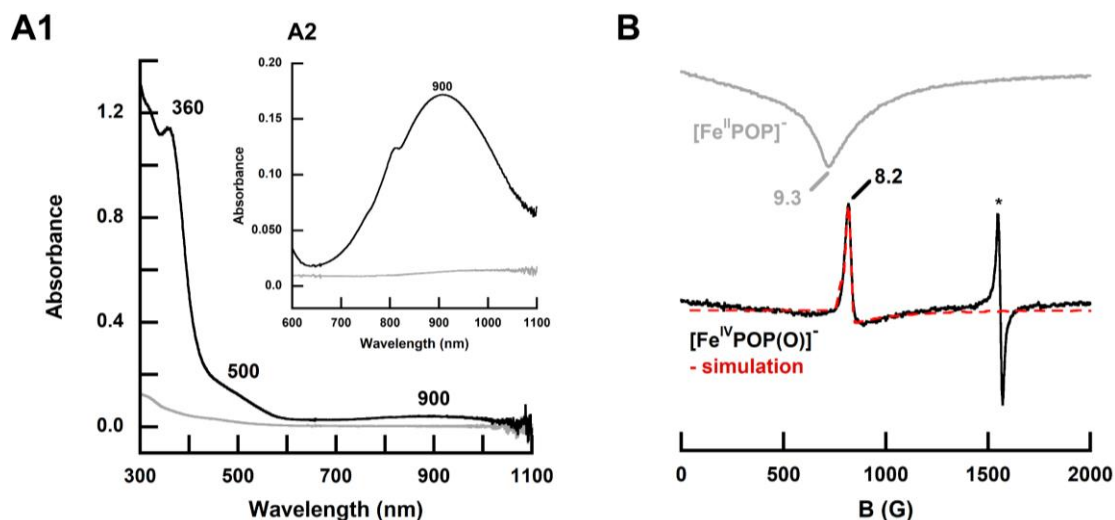


Figure 4-4. (A1) Electronic absorption spectra of 0.39 mM $\text{K}[\text{Fe}^{\text{II}}\text{POP}]$ (grey) in the presence of 2 equiv. 18C6 and after addition of IBX-iPr (black) in dimethylformamide (DMF):THF at $-80\text{ }^{\circ}\text{C}$. (A2) zoomed in view of the 900 nm transition for $[\text{Fe}^{\text{IV}}\text{POP}(\text{O})]^-$ when generated using 1.9 mM $\text{K}[\text{Fe}^{\text{II}}\text{POP}(\text{H}_2\text{O})]$ as the starting complex. (B) EPR spectra ($//$ -mode, 12.3 K, DMF:THF) of 15.8 mM $\text{K}[\text{Fe}^{\text{II}}\text{POP}]$ (grey) and after addition of IBX-iPr (black) at $-80\text{ }^{\circ}\text{C}$. Asterisks in panel B indicate signals from small amounts of ferric impurities.

In addition, the stability $[\text{Fe}^{\text{IV}}\text{POP}(\text{O})]^-$ was monitored optically at higher temperature such as $-20\text{ }^{\circ}\text{C}$, and a self-decay rate of the high-valent complex was measured. The k_{obs} values measured using $\text{K}[\text{Fe}^{\text{II}}\text{POP}]$ or $\text{K}[\text{Fe}^{\text{II}}\text{POP}(\text{H}_2\text{O})]$ as the starting complex were within experimental error of each other (Figure 4-5, Table 4-2). This further supports that the aqua ligand does not affect the properties of the $[\text{Fe}^{\text{IV}}\text{POP}(\text{O})]^-$ complex.

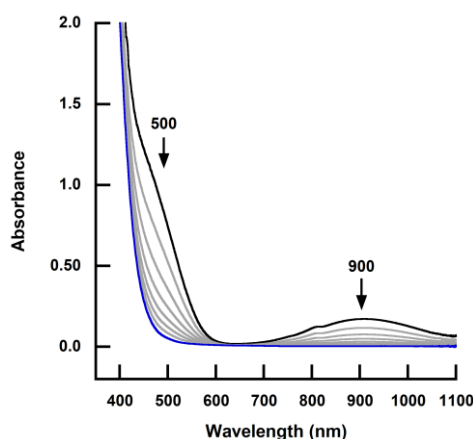


Table 4-2. The self-decay k_{obs} (900nm) of $[\text{Fe}^{\text{IV}}\text{POP}(\text{O})]^-$ complex at $-20\text{ }^{\circ}\text{C}$ in DMF.

Starting Complex	k_{obs} (s^{-1})
$\text{K}[\text{Fe}^{\text{II}}\text{POP}]$	0.0117 ± 0.0008
$\text{K}[\text{Fe}^{\text{II}}\text{POP}(\text{H}_2\text{O})]$	0.0122 ± 0.0005

Figure 4-5. The UV-vis spectra of monitoring self-decay of $[\text{Fe}^{\text{IV}}\text{POP}(\text{O})]^-$ (2 mM) at $-20\text{ }^{\circ}\text{C}$ in DMF. The starting complex for formation of $[\text{Fe}^{\text{IV}}\text{POP}(\text{O})]^-$ is either $\text{K}[\text{Fe}^{\text{II}}\text{POP}]$ or $\text{K}[\text{Fe}^{\text{II}}\text{POP}(\text{H}_2\text{O})]$. Determination of k_{obs} was done using absorbances monitored at 900 nm.

Reactivity of Fe^{IV}(O)

One important parameter obtained from the EPR spectroscopy is the rhombicity (E/D) value for [Fe^{IV}POP(O)]⁻ of 0.04, whereas the E/D value of [Fe^{IV}poat(O)]⁻ is 0.014(2).³⁹ This difference suggests [Fe^{IV}POP(O)]⁻ is more rhombic than [Fe^{IV}poat(O)]⁻, which is consistent with our hypothesis that the -OPh groups in the phosphoryl amide arms could be more flexible and lower the symmetry of the complex due to extra oxygen atom linkages. This result is encouraging for further exploration of reactivity of [Fe^{IV}POP(O)]⁻. However, no reactivity was observed in preliminary examination with various substrates, including fluorene, 9-(4-methoxyphenol)-fluorene, indene, cyclooctene, cyclohexene, cyclopentene, cumene, and ethylbenzene.

The lack of reactivity with these hydrocarbon substrates lead to the hypothesis that if we introduce intermolecular H-bonding interactions between the substrate and the complex, reactivity may be promoted. This has been observed in the active site of TauD, in which the substrate taurine is anchored in close proximity to the metal active site by H-bonding to a nearby amino acid residue (Figure 4-6A).

To test this hypothesis, benzyl alcohol was used to compare with two structurally similar but unreactive substrates---cumene and ethylbenzene (Figure 4-6B). Unlike cumene and ethylbenzene, the OH of benzyl alcohol could serve as an H-bond donor to the oxygen atoms of the P=O units in phosphoryl amido arms (Figure 4-6C). The H-bond interaction could bring the benzyl alcohol in close proximity to the Fe^{IV} moiety and possibly promote reactivity of the complex.

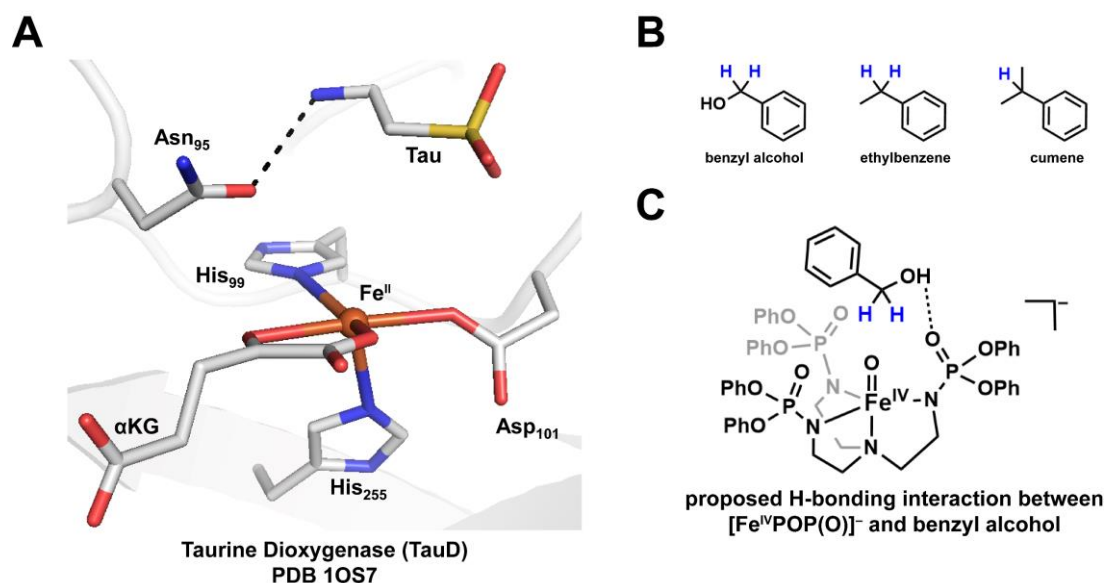


Figure 4-6. (A) Example of TauD (PDB:1OS7) having taurine anchored within the active site by H-bonding between Asn₉₅ and Tau. (B) Three substrates used for comparing reactivity. (C) Proposed H-bonding interaction between benzyl alcohol and the [Fe^{IV}POP(O)]⁻ complex.

Unlike cumene and ethylbenzene, reactivity of [Fe^{IV}POP(O)]⁻ towards benzyl alcohol was observed. The organic product of this reaction was characterized by GC-MS and ¹H NMR (Figure 4-7), whereas the inorganic product was characterized by EPR spectroscopy (Figure 4-8).

The organic product was produced from a stoichiometric bulk reaction (1 equiv. with respect to complex) at -20 °C and extracted using pentane. GC-MS confirmed the organic product to be benzaldehyde as the retention time of 3.36 min and the corresponding mass spectrum of the reaction solution had m/z peaks that matched with a benzaldehyde reference; the ¹H NMR spectrum of the extracted reaction mixture further showed a 10.02 ppm feature diagnostic of a benzaldehyde proton. However, both methods showed that there was still a significant amount of benzyl alcohol remaining in the reaction mixture. Through quantification studies using GC-MS and ¹H NMR, the ratio of leftover benzyl alcohol to benzaldehyde produced is approximately 1:1, suggesting the stoichiometry of the reaction to be 2 [Fe^{IV}POP(O)]⁻ complexes to 1 benzyl alcohol molecule. The stoichiometry is reasonable because it is possible that the O–H bond in benzyl alcohol also needs to be cleaved for the formation of

benzaldehyde. Therefore, for the oxidation of each benzyl alcohol molecule to benzaldehyde, one equiv. of $[\text{Fe}^{\text{IV}}\text{POP}(\text{O})]^-$ complex is required for activating the C–H bond, and a second equivalent is needed for cleaving the O–H bond.

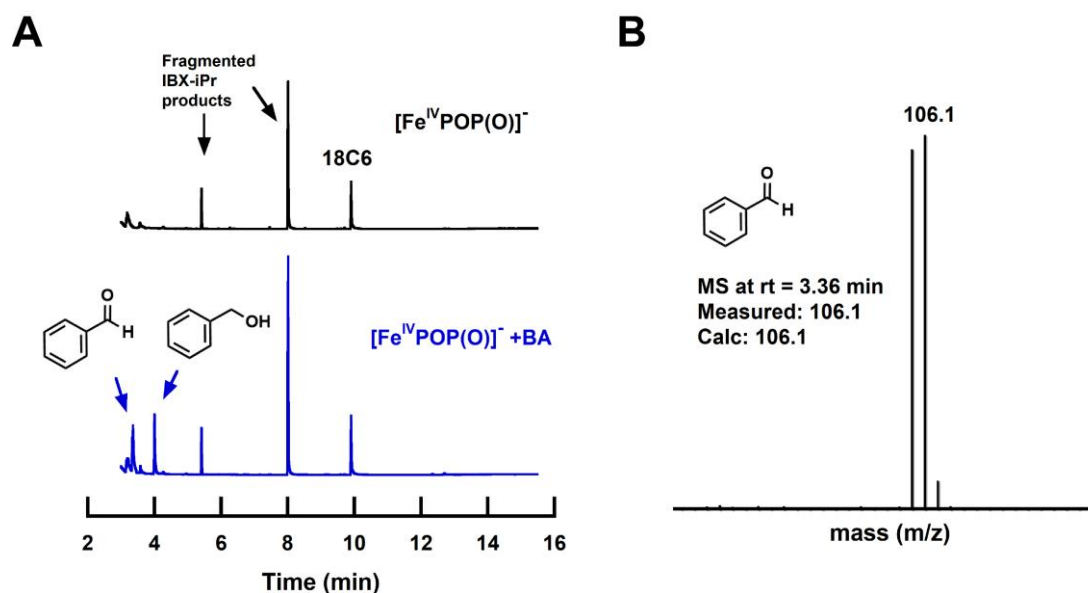


Figure 4-7. (A) Gas chromatogram and (B) mass spectrum at retention time = 3.36 min from the GC-MS measurement in DCM for the extracted organic product from the bulk reaction.

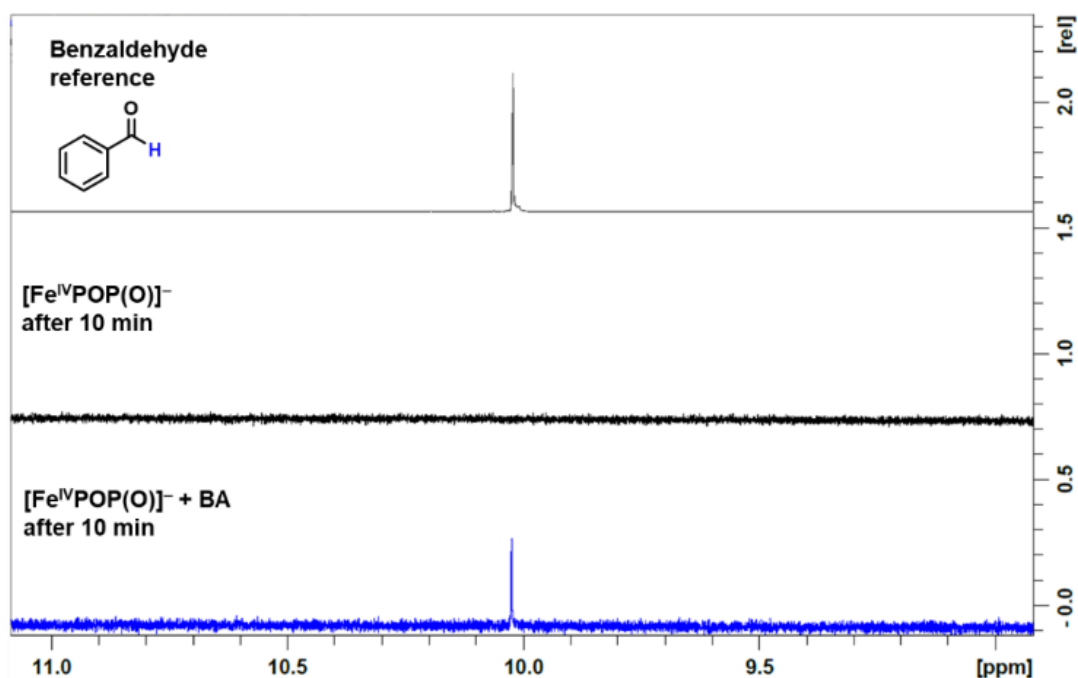


Figure 4-8. ^1H NMR measurement in d_6 -DMSO of benzaldehyde reference (grey), the extracted organic product from the controlled experiment without substrate as reference (black), and the extracted organic product from the reaction with benzyl alcohol (blue).

The inorganic product was produced via bulk reaction with excess substrate present. The perpendicular(\perp)-mode EPR spectrum showed $g = 4.3$ and 9.6 signals that are consistent with a rhombic $S = 5/2$ Fe^{III} center (Figure 4-9). The spectrum is very similar to the previously characterized $[\text{Fe}^{\text{III}}\text{poat}(\text{OH})]^-$, suggesting the possible inorganic product to be $[\text{Fe}^{\text{III}}\text{POP}(\text{OH})]^-$. From the characterization of organic and inorganic product, the overall reaction can be represented as in Scheme 4-4.

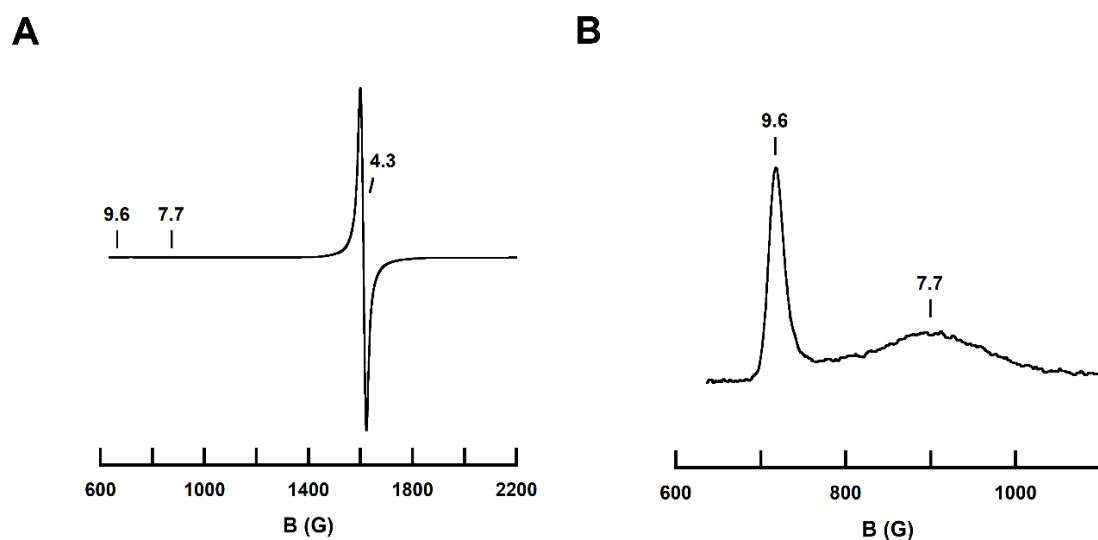
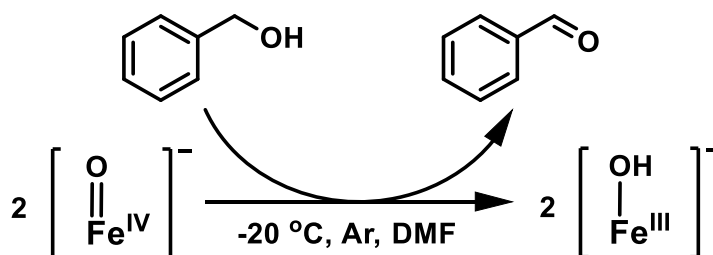


Figure 4-9. (A) EPR spectrum (\perp -mode, 8.2 K, DMF:THF) of the inorganic product prepared as bulk synthesis of $[\text{Fe}^{\text{IV}}\text{POP}(\text{O})]^-$ + benzyl alcohol in an EPR tube. (B) zoomed in view of the low field region.



Scheme 4-4. Reactivity between $[\text{Fe}^{\text{IV}}\text{POP}(\text{O})]^-$ and benzyl alcohol.

To optimize the conditions for accurate measurements of reaction rates, temperature and solvent were adjusted for the stability and reactivity of the $[\text{Fe}^{\text{IV}}\text{POP}(\text{O})]^-$ complex: (1) the complex was found to be more stable in DMF compare to DMF:THF (Figure 4-10); and (2) the self-decay k_{obs} at $-20\text{ }^\circ\text{C}$ was

found to be high enough for possible substrate reactivity while still providing long enough time ($t_{1/2} = 57.75$ s) for experimental measurements. Therefore, all further reactivities with benzyl alcohol were performed in DMF at -20 °C.

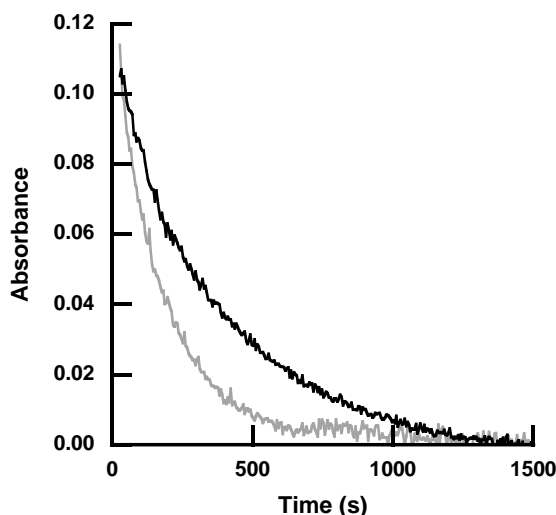


Figure 4-10. Comparison of the self-decay rate monitored via electronic absorption spectra at 900 nm band of $[\text{Fe}^{\text{IV}}\text{POP}(\text{O})]^-$ complex in DMF vs. in DMF:THF at -40 °C.

Once the reactivity conditions were determined, all kinetic measurements were performed using excess substrates (>10 equiv.) to obtain pseudo-first order rate constant (k_{obs}) in DMF at -20 °C. The k_{obs} of each experiment was measured by monitoring the rate of decrease in intensity of the 900 nm d-d transition in the electronic absorption spectra of $[\text{Fe}^{\text{IV}}\text{POP}(\text{O})]^-$ complex and plotting the change of absorbance versus time (Figure 4-11).

To further probe the reactivity of $[\text{Fe}^{\text{IV}}\text{POP}(\text{O})]^-$ towards benzyl alcohol, *para*-substituted benzyl alcohols were investigated (Figure 4-12). The k_{obs} of each substrate increased when concentration of the substrate increased as expected. Plotting the linear relationship between k_{obs} and concentration allowed the determination of the second order rate constant (k_2) for each *para*-substituted benzyl alcohols. A Hammett plot obtained using these k_2 values revealed that substrates with electron withdrawing groups have faster reaction rates than the ones with electron donating groups (Figure 4-13, Table 4-3).

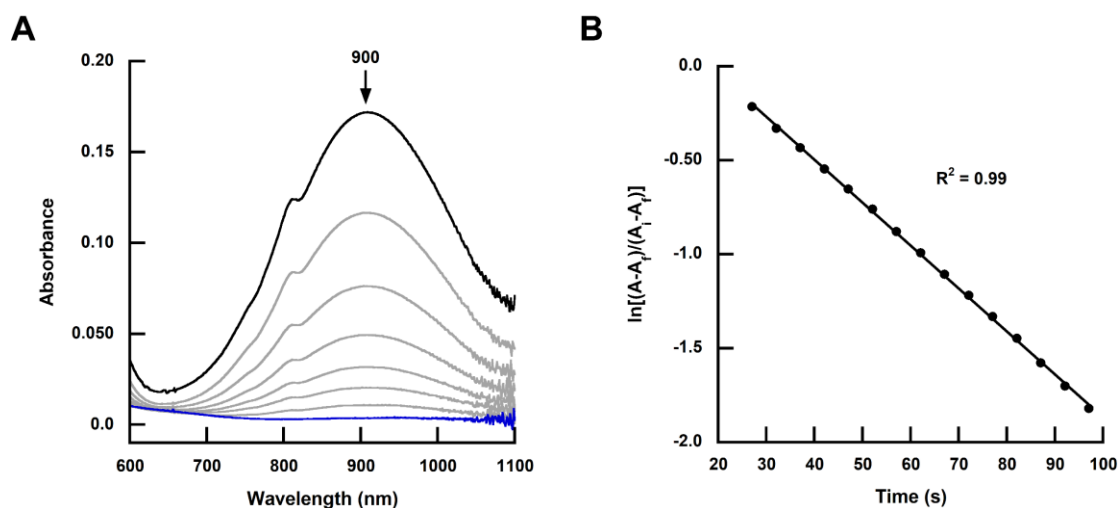


Figure 4-11. (A) The electronic absorption spectra of 1.9 mM $[\text{Fe}^{\text{IV}}\text{POP}(\text{O})]^-$ complex monitored at 900 nm during reaction with benzyl alcohol as substrate in DMF at $-20\text{ }^\circ\text{C}$. (B) Plot of $\ln\left(\frac{A-A_f}{A_i-A_f}\right)$ vs. time corresponding to the change of intensity at 900 nm band for determination of pseudo-first order rate constant (k_{obs}).

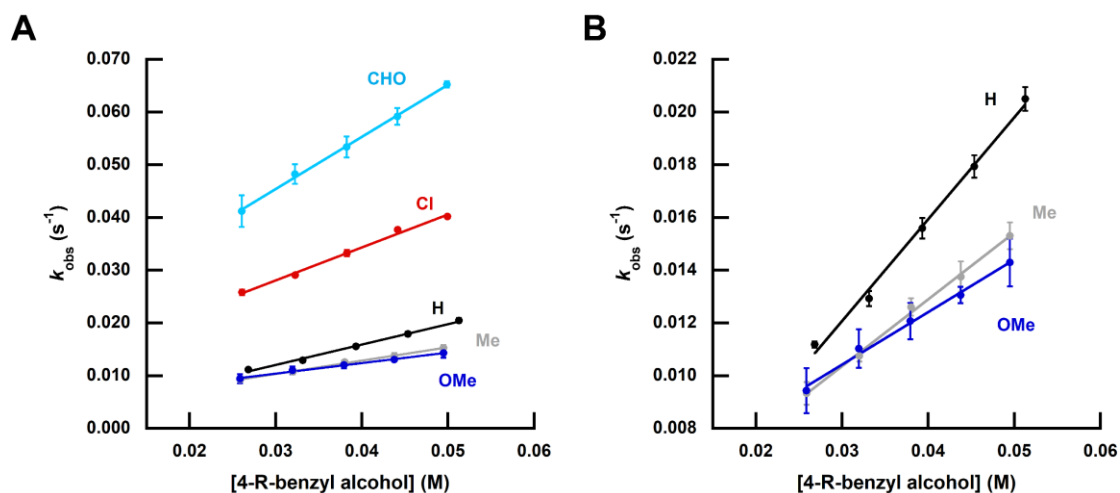


Figure 4-12. (A) Plot of k_{obs} vs. concentration of 4-R-benzyl alcohol in DMF at $-20\text{ }^\circ\text{C}$ and (B) a zoomed-in version for substrates with $\text{R} = \text{H}$, Me, and OMe. The slopes of these linear equations are used for determining second order rate constant of the reaction between $[\text{Fe}^{\text{IV}}\text{POP}(\text{O})]^-$ complex and substrates.

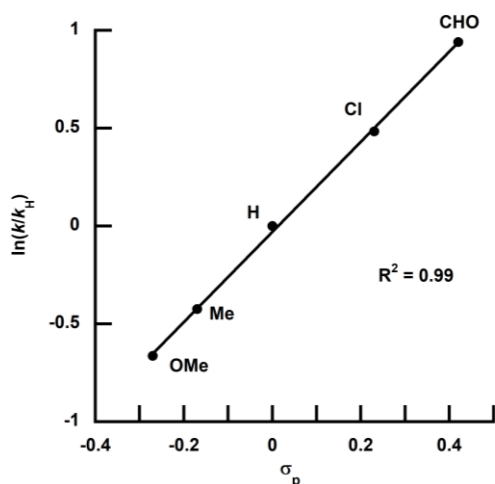


Table 4-3. Second order rate constants.

R	k ($M^{-1}s^{-1}$)	σ
OMe	0.100(5)	-0.27
Me	0.127(4)	-0.17
H	0.193(8)	0
Cl	0.314(14)	0.23
CHO	0.495(12)	0.42

Figure 4-13. Hammett plot for reactivity of $[Fe^{IV}POP(O)]^-$ complex with *para*-substituted benzyl alcohols as substrates in DMF at -20 °C.

Additional mechanistic information about the reaction between $[Fe^{IV}POP(O)]^-$ and benzyl alcohol was obtained from kinetic isotope effect (KIE) measured using benzyl alcohols deuterated at different positions as substrates. When the α,α - d_2 -benzyl alcohol with deuteration at the benzylic carbon position was used as substrate (Figure 4-14), a large KIE of 15 was determined, suggesting the C–H bond cleavage is involved in the rate determining step. KIE experiments measured using the d_1 -benzyl alcohol deuterated at the OH position was performed by current graduate student Jennifer L. Jaimes. Using d_1 -benzyl alcohol as substrate, the determined k_D value was statistically the same as k_H value. This resulted in KIE ~ 1 , suggesting the O–H bond cleavage is not involved in the rate determining step.

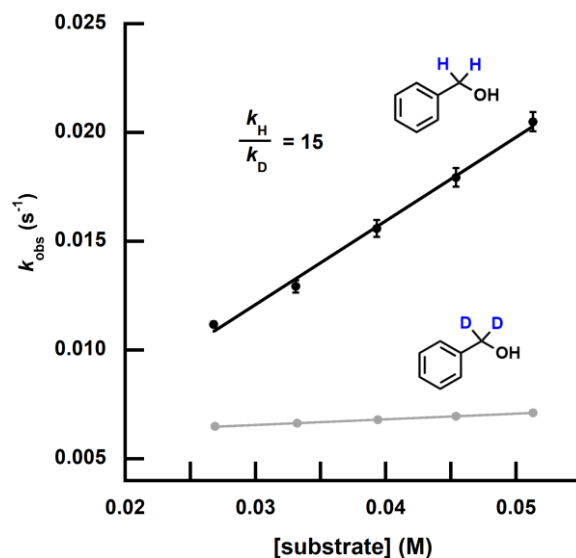


Figure 4-14. Plot for reactivity of $[\text{Fe}^{\text{IV}}\text{POP}(\text{O})]^-$ complex with benzyl alcohols and d_2 -benzyl alcohol as substrates in DMF at $-20\text{ }^\circ\text{C}$. The ratio of the measured k_{obs} for the two reactions is used to determine a KIE of 15.

Investigation of H-bond effects

The most challenging aspect of this project is to demonstrate whether the H-bonding interactions between the complex and 4-R-benzyl alcohol facilitates reactivity. One possible method is to investigate the mixture of $\text{K}[\text{Fe}^{\text{II}}\text{POP}(\text{H}_2\text{O})]$ complex and 4-R-benzyl alcohol using ^1H NMR spectroscopy to observe possible shift or broadening of the 4-R-benzyl alcohol O–H proton resonance. However, the $\text{K}[\text{Fe}^{\text{II}}\text{POP}(\text{H}_2\text{O})]$ complex is paramagnetic and can cause difficult analysis in the ^1H NMR measurements. Therefore, an analogous complex $\text{K}[\text{Zn}^{\text{II}}\text{POP}(\text{H}_2\text{O})]$ was synthesized for NMR studies and its molecular structure was determined to be isomorphous to $\text{K}[\text{Fe}^{\text{II}}\text{POP}(\text{H}_2\text{O})]$ by XRD method (Table 4-S1).

Using the $\text{K}[\text{Zn}^{\text{II}}\text{POP}(\text{H}_2\text{O})]$ complex, NMR studies was performed to shed light on possible H-bonding interactions between complex and 4-R-benzyl alcohol. When ^1H NMR measurement was performed for a mixture of $\text{K}[\text{Zn}^{\text{II}}\text{POP}(\text{H}_2\text{O})] + 2$ equiv. 18C6 + 4-R-benzyl alcohol in d_6 -DMSO, shifts in the O–H protons for both 4-R-benzyl alcohol and the Zn^{II} -aqua complex were observed (Figure 4-15, Table 4-4). This suggests the complex indeed have the

ability to H-bond to the substrate in the solution state as proposed, and the possible orientation of the molecules can be illustrated by Figure 4-16. It is known that when a hydrogen atom is part of an H-bond, the ^1H NMR signal should shift downfield due to larger proton deshielding.^{49–52} However, the chemical shift of the protons on aquo ligand is shifted upfield, and the reason for this observation remains unclear.

In addition, the same ^1H NMR measurement was done using ethylbenzene as the control experiment to ensure the shift of the peaks is not due to other possible non-covalent interactions. The resultant NMR spectrum showed significantly smaller deviation in chemical shift of -0.0167 ppm, and further support that the H-bonding interaction between $\text{K}[\text{Zn}^{\text{II}}\text{POP}(\text{H}_2\text{O})]^-$ complex and 4-R-benzyl alcohol are possible.

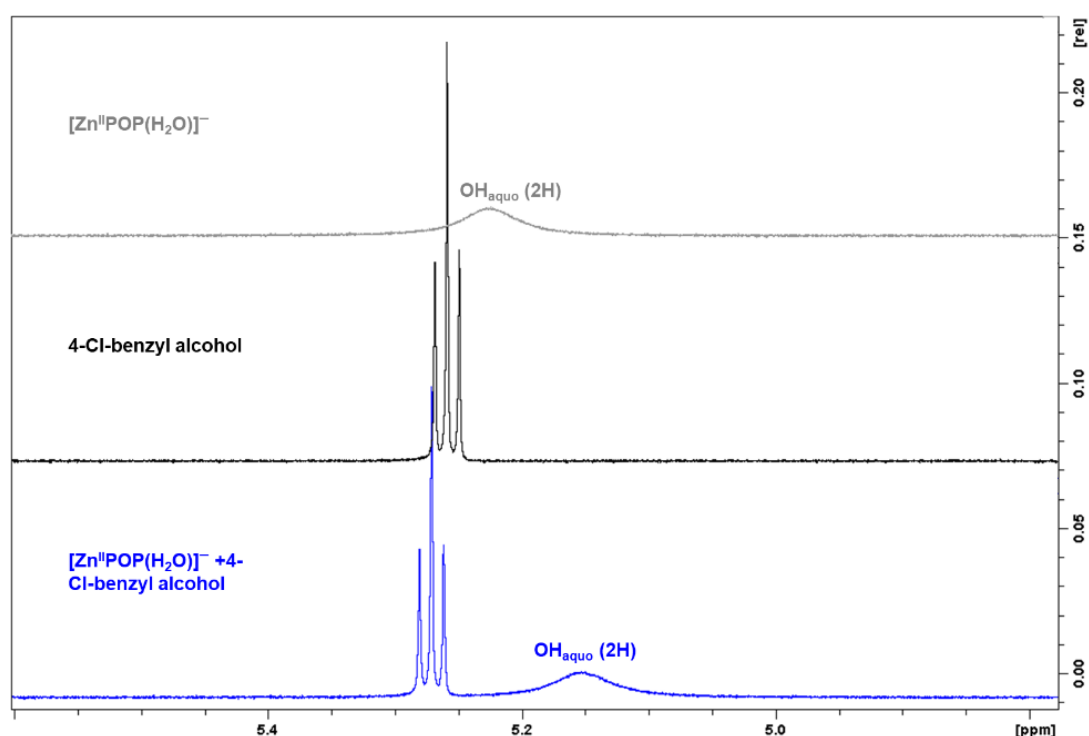


Figure 4-15. ^1H NMR studies of $[\text{Zn}^{\text{II}}\text{POP}(\text{H}_2\text{O})]^- + 4\text{-Cl-benzyl alcohol}$ in $d_6\text{-DMSO}$. Chemical shift also observed when same experiment was done using 4-Me-benzyl alcohol and 4-OMe-benzyl alcohol. Shift of $[\text{Zn}^{\text{II}}\text{POP}(\text{H}_2\text{O})]^-$ aquo ligand in experiments with 4-OMe-benzyl alcohol resulted in overlap with the substrate O–H peak and is reported in approximate value.

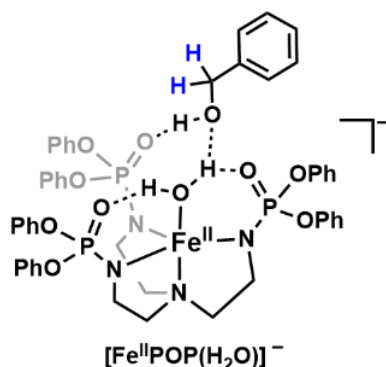


Table 4-4. chemical shifts (ppm) for 4-R-benzyl alcohol and the Zn^{II}-aqua complex.

substrates	substrates O-H	Zn ^{II} -aqua (H ₂ O)
4-OMe-benzyl alcohol	0.0101	Approx. -0.2
4-Me-benzyl alcohol	0.0088	-0.1973
4-Cl-benzyl alcohol	0.0122	-0.0730
Ethylbenzene	-	-0.0167

Figure 4-16. Proposed docking of 4-R-benzyl alcohol to the [Fe^{II}POP(H₂O)]⁻ complex in solution state based on ¹H NMR studies of [Zn^{II}POP(H₂O)]⁻ + 4-R-benzyl alcohol in *d*₆-DMSO.

The possible H-bonding interaction between the aqua ligand of Zn^{II}-aqua complex and the 4-R-benzyl alcohol raises the question: when [Fe^{IV}POP(O)]⁻ was formed, can the 4-R-benzyl alcohol also H-bond to the oxido moiety of the complex? Our lab has previously demonstrated the ability of an Fe^{IV}-oxido moiety to participate in H-bonding in spite of its decreased Lewis basicity by monitoring the energy of the diagnostic d-d transition.³⁹ UV-vis and EPR measurement of [Fe^{IV}POP(O)]⁻ + 4-R-benzyl alcohol may provide a possible answer to this question, but it is difficult to trap the pre-reaction stage as the addition of 4-R-benzyl alcohol to [Fe^{IV}POP(O)]⁻ immediately initiates the reaction. To overcome this challenge, *d*₂-benzyl alcohol was used as the substrate because of its slow reactivity observed during KIE experiments, and the reaction temperature was lowered to -60 °C to further mitigate reactivity.

Addition of *d*₂-benzyl alcohol to [Fe^{IV}POP(O)]⁻ at -60 °C showed no shift of the 900 nm d-d band in the electronic absorption spectra and no observable change of the *g* = 8.2 signal in EPR spectra (Figure 4-17). One possible explanation for this observation is that the benzyl alcohol is only H-bonded to the P=O, while the oxido moiety of [Fe^{IV}POP(O)]⁻ is unaffected, but additional experiments are needed to support this hypothesis.

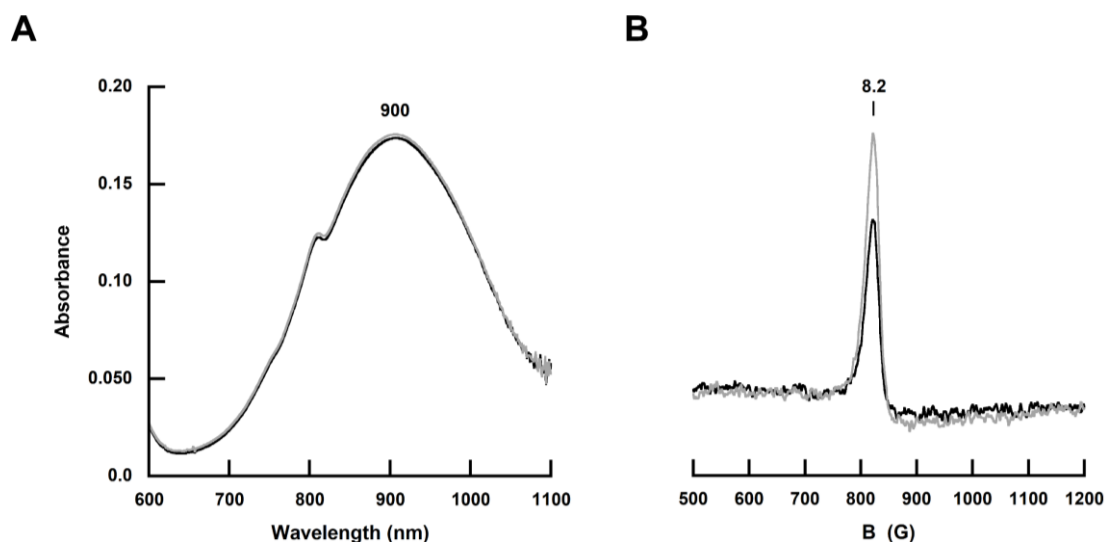


Figure 4-17. (A) Electronic absorption spectra of 2 mM $[\text{Fe}^{\text{IV}}\text{POP}(\text{O})]^-$ (black) and after adding d_2 -benzyl alcohol to it (grey) at $-60\text{ }^\circ\text{C}$ in DMF. (B) EPR spectra ($//$ -mode, DMF:THF) of 15 mM $[\text{Fe}^{\text{IV}}\text{POP}(\text{O})]^-$ (black, 6.6 K) and after adding d_2 -benzyl alcohol (grey, 8.9 K) at $-80\text{ }^\circ\text{C}$.

Comparing reactivity between $[\text{Fe}^{\text{IV}}\text{POP}(\text{O})]^-$ and $[\text{Fe}^{\text{IV}}\text{poat}(\text{O})]^-$

To explore the hypothesis that the $[\text{POP}]^{3-}$ ligand framework is more flexible and accessible than the $[\text{poat}]^{3-}$ ligand framework and promotes reactivity, the same kinetic experiments were performed with the $[\text{Fe}^{\text{IV}}\text{poat}(\text{O})]^-$ complex. When benzyl alcohol was used as a substrate for $[\text{Fe}^{\text{IV}}\text{poat}(\text{O})]^-$ in DMF at $-20\text{ }^\circ\text{C}$, minimal reactivity was observed (Figure 4-18B). In comparison to the reactivity with $[\text{Fe}^{\text{IV}}\text{POP}(\text{O})]^-$ complex discussed before, there is a significant difference between the two systems. Although the two complexes have the same geometry around the metal center and a similar tri-anionic N donor environment with appended $\text{P}=\text{O}$ units serving as H-bond acceptors (Figure 4-18A), there is still a 100-fold difference in their second order rate constant. This large difference emphasizes that the local environment around the Fe^{IV} -oxido moiety can influence its properties and reactivity.

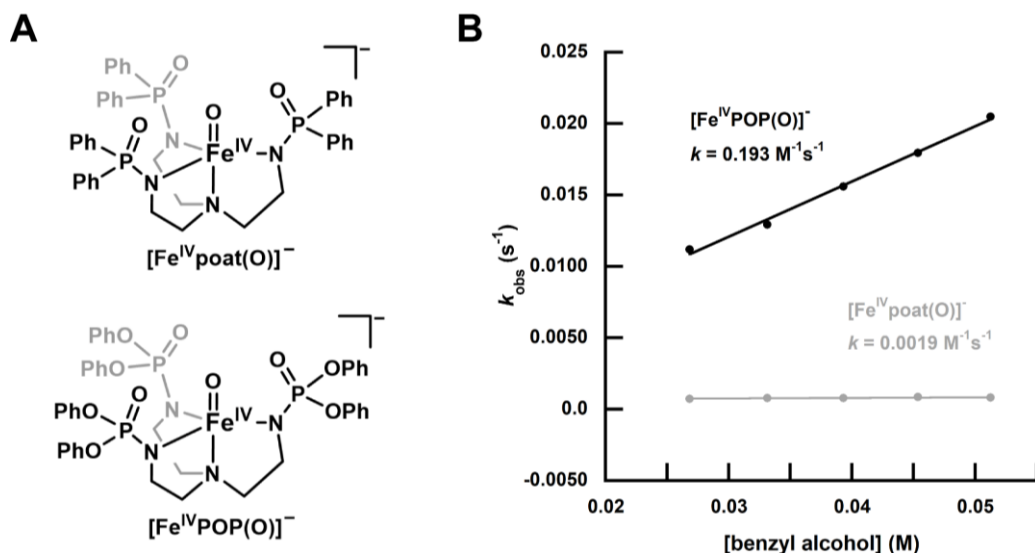


Figure 4-18. (A) $[\text{Fe}^{\text{IV}}\text{poat}(\text{O})]^-$ and $[\text{Fe}^{\text{IV}}\text{POP}(\text{O})]^-$. (B) Plot of k_{obs} vs. concentration of benzyl alcohol in DMF at $-20\text{ }^\circ\text{C}$ for $[\text{Fe}^{\text{IV}}\text{POP}(\text{O})]^-$ (black) and $[\text{Fe}^{\text{IV}}\text{poat}(\text{O})]^-$ (grey).

Summary and Conclusion

Two Fe^{II} complexes in $[\text{POP}]^{3-}$ ligand framework, $\text{K}[\text{Fe}^{\text{II}}\text{POP}]$ and $\text{K}[\text{Fe}^{\text{II}}\text{POP}(\text{H}_2\text{O})]$ were synthesized and characterized. Using these Fe^{II} complexes as synthon, a high spin $[\text{Fe}^{\text{IV}}\text{POP}(\text{O})]^-$ complex was generated and characterized using UV-vis and EPR spectroscopies. The $[\text{Fe}^{\text{IV}}\text{POP}(\text{O})]^-$ complex has the ability to perform C–H bond cleavage with series of 4-R-benzyl alcohol to form corresponding benzaldehyde product, while no reactivity towards a variety of hydrocarbons, especially two structurally similar substrates, ethylbenzene (82.4 kcal/mol⁵³) and cumene (80.2 kcal/mol⁵³) was observed. The $\text{BDFE}_{\text{C-H}}$ for some of the unreactive hydrocarbons such as fluorene (77.4 kcal/mol⁵⁴), indene (76.7 kcal/mol⁵⁴), and 9-(4-methoxyphenol)-fluorene (<75 kcal/mol^{55,56}) are lower than that of benzyl alcohol (79-81 kcal/mol^{57,58}), which suggests that the different reactivities observed for different substrates is not entirely dependent on $\text{BDFE}_{\text{C-H}}$.

The H-bonding interaction between the $\text{K}[\text{Zn}^{\text{II}}\text{POP}(\text{H}_2\text{O})]$ complex and benzyl alcohol was probed by ^1H NMR and indicated H-bonding interactions are possible. These results support the hypothesis that introducing H-bonding interactions between the complex and substrates in similar manner to TauD

anchoring taurine in close proximity may promote reactivities.

The comparison between the $[\text{Fe}^{\text{IV}}\text{POP}(\text{O})]^-$ and $[\text{Fe}^{\text{IV}}\text{poat}(\text{O})]^-$ complexes illustrated that two complexes with similar primary coordination sphere and same geometry around the metal center can have a 100-fold differences in their reactivities via differences in their local environment. The higher E/D value and better reactivity of $[\text{Fe}^{\text{IV}}\text{POP}(\text{O})]^-$ than $[\text{Fe}^{\text{IV}}\text{poat}(\text{O})]^-$ complex is consistent with the proposal that the of $[\text{POP}]^{3-}$ ligand framework is more flexible, which can allow substrates to better approach the Fe^{IV} -oxido unit and promote reactivity.

Experimental

General procedure

Unless otherwise stated, all reactions were performed under an argon atmosphere in a Vacuum Atmospheres Co dry box. Solvents were sparged with argon and dried over columns containing Q-5 and molecular sieves. $\text{Fe}^{\text{II}}(\text{OAc})_2$ ⁵⁹ and IBX-*i*Pr^{60,61} were synthesized following literature procedures and stored under Ar atmosphere at room temperature. Potassium hydride as a 30% suspension in mineral oil was filtered with a medium pore size glass fritted funnel and washed with 10 mL pentane and 10 mL Et_2O five times or until the powder is white, then dried under vacuum and stored under Ar atmosphere at room temperature. 4-OMe-benzylalcohol was purchased from Acros Organics and used without further purification. 4-CHO-benzylalcohol was purchased from Oakwood Chemicals and used without further purification. Tris(2-aminoethyl) amine (tren), diphenyl phosphoryl chloride, 18-crown-6 (18C6), benzylalcohol, and benzylalcohol- $\alpha,\alpha\text{-}d_2$ were purchased from Sigma-Aldrich and used without further purification. Triethylamine was distilled under reduced pressure and gentle heat. 4-Cl-benzylalcohol and 4-Me-benzylalcohol were purchased from Sigma-Aldrich and recrystallized with ethanol multiple times.

Physical methods

All electronic absorption spectra were collected in a 1 cm quartz cuvette with a magnetic spin bar inside. Kinetic measurements were recorded on an 8453E Agilent UV-vis spectrometer equipped with a Unisoku Unispeks cryostat. X-band EPR spectra were recorded as frozen solutions either using a Bruker EMX spectrometer equipped with an ER041XG microwave bridge, an Oxford Instrument liquid-helium quartz cryostat, and a dual-mode cavity (ER4116DM), or using a Bruker ELEXSYS spectrometer equipped with an Oxford ESR-910 liquid helium cryostat and a Bruker bimodal cavity for the generation of microwave fields parallel and transverse to the applied magnetic field. The quantification of all signals was performed relative to a CuEDTA spin standard prepared from a copper atomic absorption standard (Sigma-Aldrich). The microwave frequency was calibrated with a frequency counter, and the magnetic field was measured with an NMR gaussmeter. The sample temperature was calibrated against a calibrated cernox sensor (Lakeshore CX-1050) mounted inside an EPR tube. A modulation frequency of 100 kHz was used for all EPR spectra. The simulation software SpinCount was written by Professor Michael Hendrich at Carnegie Mellon University. NMR experiments were measured either on 600 MHz Bruker AVANCE spectrometer with BBFO (broadband, including fluorine, observe) cryoprobe as standard, 500 MHz Bruker DRX spectrometer with TCI (three channel inverse) cryoprobe as standard, or 400 MHz Bruker DRX spectrometer with switchable QNP (quad nucleus probe) probe as standard. GC-MS was measured on a Waters Micromass GCT Premier mass spectrometer with DB-5 30 m x 0.25 mm x 0.25 μ film column, helium as carrier gas, and positive CI (ammonia reagent gas) mode for ionization.

X-ray crystallography

{K[Fe^{II}POP(H₂O)]}₂

A colorless crystal of approximate dimensions 0.379 x 0.338 x 0.152 mm was mounted in a cryoloop and transferred to a Bruker SMART APEX II diffractometer. The APEX2⁶² program package was used to determine the unit-cell parameters and for data collection (30 sec/frame scan time for a sphere of diffraction data). The raw frame data was processed using SAINT⁶³ and SADABS⁶⁴ to yield the reflection data file. Subsequent calculations were carried out using the SHELXTL⁶⁵ program. There were no systematic absences nor any diffraction symmetry other than the Friedel condition. The centrosymmetric triclinic space group $P\bar{1}$ was assigned and later determined to be correct.

The structure was solved by direct methods and refined on F^2 by full-matrix least-squares techniques. The analytical scattering factors⁶⁶ for neutral atoms were used throughout the analysis. Hydrogen atoms (H1A, H1B, H11A, H11B) on O1 and O11 of the aqua ligand were located from a difference-Fourier map and refined (x, y, z and U_{iso}). The rest of the hydrogen atoms were included using a riding model.

Least-squares analysis yielded $wR2 = 0.1080$ and $Goof = 1.038$ for 1115 variables refined against 20941 data (0.74 Å), $R1 = 0.0392$ for those 16759 data with $I > 2.0\sigma(I)$.

{K[Zn^{II}POP(H₂O)]}₂

A colorless crystal of approximate dimensions 0.170 x 0.192 x 0.294 mm was mounted in a cryoloop and transferred to a Bruker SMART APEX II diffractometer system. The APEX2⁶² program package was used to determine the unit-cell parameters and for data collection (25 sec/frame scan time). The raw frame data was processed using SAINT⁶³ and SADABS⁶⁴ to yield the reflection data file. Subsequent calculations were carried out using the

SHELXTL⁶⁵ program package. There were no systematic absences nor any diffraction symmetry other than the Friedel condition. The centrosymmetric triclinic space group $P\bar{1}$ was assigned and later determined to be correct.

The structure was solved by direct methods and refined on F^2 by full-matrix least-squares techniques. The analytical scattering factors⁶⁶ for neutral atoms were used throughout the analysis. Hydrogen atoms associated with O(1) and O(11) were located from a difference-Fourier map and refined (x, y, z and U_{iso}). The remaining hydrogen atoms were included using a riding model.

Least-squares analysis yielded $wR2 = 0.1143$ and $Goof = 1.032$ for 1115 variables refined against 21475 data (0.75\AA), $R1 = 0.0478$ for those 14143 data with $I > 2.0\sigma(I)$.

Table 4-S1. Metric parameters for $\{K[Fe^IIPOP(H_2O)]\}_2$ and $\{K[Zn^IIPOP(H_2O)]\}_2$.

Complex	$\{K[Fe^IIPOP(H_2O)]\}_2$	$\{K[Zn^IIPOP(H_2O)]\}_2$
Empirical Formula	$C_{84}H_{86}Fe_2K_2N_8O_{20}P_6$	$C_{84}H_{88}K_2N_8O_{20}P_6Zn_2$
Fw	1903.32	1924.38
T (K)	133(2) K	93(2) K
Crystal system	Triclinic	Triclinic
Space group	$P\bar{1}$	$P\bar{1}$
a (\AA)	14.427(3)	14.412(1)
b (\AA)	16.428(3)	16.336(1)
c (\AA)	20.699(4)	20.664(2)
α ($^\circ$)	99.145(2)	98.842(2)
β ($^\circ$)	98.055(2)	98.020(2)
γ ($^\circ$)	111.423(2)	111.392 (2)
V (\AA^3)	4402.8(13)	4373.7(6)
Z	2	2
δ_{calcd} (Mg/m^3)	1.436	1.461
GOF on F^2	1.038	1.032
R1	0.0392	0.0478
wR2	0.1080	0.1143

Synthesis of H_3POP ⁶⁷

To a clear colorless solution of tris(2-aminoethyl) amine (tren) (4.525 g, 30.94 mmol) and triethylamine (46.84 g, 462.9 mmol) in 200 mL of tetrahydrofuran (THF), diphenyl phosphoryl chloride (25.0 g, 93.1 mmol) in 80 mL of THF was

added dropwise while stirring. The reaction solution immediately turned to white cloudy heterogeneous mixture. Once the addition was complete, 20 mL of THF was added to rinse the addition funnel. After the addition funnel was removed, the round bottom flask was covered with a glass stopper and left to stir overnight. The flask was brought into ambient condition the next day for workup. After filtering off the white precipitate (Et_3NHCl), the solvent was removed until a thick oil was obtained. Diethyl ether (Et_2O ; 200 mL) was added to the resulting oil and stirred vigorously over 30-60 min to slowly precipitate out a white powder (24.72 g, 94.70 %), which was collected on a medium porosity glass-fritted funnel, washed five times with 20 mL ether, and dried for several hours under vacuum. The dried white solid was brought into glovebox and stored under Ar atmosphere. ^1H NMR (500 MHz, DMSO, ppm): 2.50 (t, 6H), 3.11 (q, 6H), 6.13 (q, 3H), 7.45 (t, 12H), 7.50 (d, 6H), 7.61 (t, 12H); ^{13}C NMR (125 MHz, DMSO, ppm): 151.0, 130.3, 125.2, 120.5, 56.5, 47.2; ^{31}P NMR (162 MHz, CDCl_3 , ppm): 21.9; FTIR (Diamond ATR, cm^{-1}): 3300 (N–H, sh), 3231 (N–H), 3064, 3042, 2945, 2877, 2833, 2805, 2600, 1588, 1485, 1455, 1440, 1263, 1240, 1213, 1188, 1162, 1108, 1070, 1053, 1024, 1007, 975, 917, 830, 807, 759, 725, 688, 616. HRMS (ES+, m/z): Exact mass calculated for $\text{NaC}_{42}\text{H}_{45}\text{N}_4\text{O}_9\text{P}_3$ [M + Na]: 865.23, Found: 865.2297.

Synthesis of $\text{K}[\text{Fe}^{\text{II}}\text{POP}]$

To a clear colorless solution of H_3POP (199.7 mg, 0.2370 mmol) in 4 mL THF, KH (28.7 mg, 0.716 mmol) was added and stirred for 1 hour or until gas evolution ceased. $\text{Fe}(\text{OAc})_2$ (41.6 mg, 0.239 mmol) was added to the reaction mixture, resulting in immediate change to an orange heterogeneous solution. After stirring for 1 hour, insoluble solids (KOAc) was filtered off through a medium pore size frit, and the solvent was removed under reduced pressure resulting in a beige solid (221.1 mg, 99.83 %). EPR (X-band, // -mode, 1:1 DMF:THF, 12.3 K): $g = 9.3$. Multiple attempts to crystallize the complex resulted

in $\text{K}[\text{Fe}^{\text{II}}\text{POP}(\text{H}_2\text{O})]$ crystals possibly due to adventitious H_2O from long crystallization period.

Synthesis of $\text{K}[\text{Fe}^{\text{II}}\text{POP}(\text{H}_2\text{O})]$

To a clear colorless solution of H_3POP (400.9 mg, 0.4757 mmol) in 6 mL THF, KH (57.5 mg, 1.43 mmol) was added and stirred for 1 hour or until gas evolution ceased. $\text{Fe}(\text{OAc})_2$ (82.8 mg, 0.476 mmol) was added to the reaction mixture, resulting in immediate change to orange heterogeneous solution. After stirring for 1 hour, 10 μL (0.55 mmol) of H_2O was added via syringe, resulting in immediate change to off white heterogeneous solution. After stirring an additional 10 min, insoluble salt of KOAc (79.3 mg, 84.92%) was filtered off through a medium pore size frit, and the resulting clear pale-yellow solution was layered under pentane. Colorless x-ray quality crystals of the desired product were obtained after 1-2 days (384 mg, 85.0 %) and the dried product was stored in $-35\text{ }^\circ\text{C}$ freezer. UV-vis (DMF:THF, $-80\text{ }^\circ\text{C}$): $\lambda_{\text{max}}/\text{nm}(\epsilon/\text{M}^{-1}\text{cm}^{-1}) = 960 (4.7)$. FTIR (Diamond ATR, cm^{-1}): 3226 (O–H), 3064, 3042, 2955, 2892, 2852, 2683, 1588, 1485, 1455, 1263, 1240, 1229, 1195, 1154, 1123, 1070, 1045, 1024, 1004, 987, 908, 882, 819, 761, 738, 688. Elemental analysis calcd for $\text{C}_{42}\text{H}_{44}\text{FeKN}_4\text{O}_{10}\text{P}_3 \cdot 0.5\text{H}_2\text{O}$: C, 52.46; H, 4.72; N, 5.83 %, found: C, 52.30; H, 4.77; N, 5.76 %.

Synthesis of $\text{K}[\text{Zn}^{\text{II}}\text{POP}(\text{H}_2\text{O})]$

This salt was prepared following the same procedure as the synthesis for $\text{K}[\text{Fe}^{\text{II}}\text{POP}(\text{H}_2\text{O})]$ using $\text{Zn}(\text{OAc})_2$ instead of $\text{Fe}(\text{OAc})_2$. The amounts of each reagent used were H_3POP (199.3 g, 0.2365 mmol) in 3 mL THF, KH (28.6 mg, 0.713 mmol), $\text{Zn}(\text{OAc})_2$ (57.1 g, 0.311 mmol), and 5 μL (0.28 mmol) of H_2O . layering of product solution under pentane resulted colorless x-ray quality crystals the following day (144.0 mg, 63.28 %). ^1H NMR (with 2 equiv. 18C_6 , 600 MHz, d_6 -DMSO, ppm): 7.3 (d, 12H); 7.2 (t, 12H); 7.0 (t, 12H); 5.2 (OH, s,

2H); 3.5 (18C6, s) 2.8 (dt, 6H); 2.0(t, 6H). FTIR (Diamond ATR, cm^{-1}): 3210 (O–H), 3064, 3042, 2958, 2892, 2852, 2688, 1588, 1485, 1455, 1263, 1240, 1229, 1195, 1159, 1127, 1070, 1049, 1024, 1004, 991, 908, 882, 819, 761, 738, 688. Elemental analysis calcd for $\text{C}_{42}\text{H}_{44}\text{KN}_4\text{O}_{10}\text{P}_3\text{Zn}\cdot 0.5\text{H}_2\text{O}$: C, 51.94; H, 4.67; N, 5.77 %, found: C, 51.92; H, 4.64; N, 5.74 %.

Low temperature solution studies of $[\text{Fe}^{\text{IV}}\text{POP}(\text{O})]^-$

In a typical experiment, the generation of $[\text{Fe}^{\text{IV}}\text{POP}(\text{O})]^-$ was performed at -80°C using 1:1 DMF:THF as solvent. The $[\text{Fe}^{\text{II}}\text{POP}(\text{H}_2\text{O})]^-$ stock solution was prepared by dissolving solid $\text{K}[\text{Fe}^{\text{II}}\text{POP}(\text{H}_2\text{O})]$ in the presence of 2.5 equiv. 18C6. Different sets of stock solutions (20-70 mM) were prepared for monitoring electronic absorption spectrum of $[\text{Fe}^{\text{IV}}\text{POP}(\text{O})]^-$ due to large differences in extinction coefficient of the features. A cuvette filled with 2 mL 1:1 DMF:THF solution was sealed with a rubber septum and transferred into the cryostat in spectrometer to equilibrate with the temperature for ~ 15 min. A 60 μL aliquot of the $[\text{Fe}^{\text{II}}\text{POP}(\text{H}_2\text{O})]^-$ stock solution was injected into the cuvette via airtight syringe and mixed for 150-200 sec to give the desired concentration (0.2, 2, or 10 mM). Then, 80 μL aliquot (1.2 equiv.) of IBX-iPr stock solution was injected to produce the $[\text{Fe}^{\text{IV}}\text{POP}(\text{O})]^-$ spectrum.

Samples for EPR studies were prepared at the same temperature and in the same solvent. In an EPR tube with 40 μL of 1:1 DMF:THF solvent, 160 μL of IBX-iPr (24.5 mM, 1.2 equiv.) was added. The EPR tube was sealed with a rubber septum and transferred into a -80°C bath to pre-chill for ~ 15 min. Then, 60 μL of $[\text{Fe}^{\text{II}}\text{POP}(\text{H}_2\text{O})]^-$ (64.8 mM) was injected into the EPR tube and let react for 20 min before freezing the sample. The solution started as clear colorless and ended with an intense orange red color. The final sample concentration was 15.0 mM.

Kinetic measurements

All kinetic experiments were measured in DMF at -20 °C in a cuvette (containing a magnetic stirbar) with 1 cm pathlength. ~68 mM of (K[Fe^{II}POP(H₂O)] + 2.5 equiv. 18C6) stock solution, ~53 mM of IBX-iPr stock solution, and ~580 mM of substrate stock solution were prepared at room temperature. All stock solution except IBX-iPr stock solution were stored at -35 °C for the duration of the experiment and warmed back to room temperature for 10 min prior to use. A cuvette filled with 2 mL DMF solvent was sealed with a rubber septum and transferred into the cryostat of the spectrophotometer to equilibrate with the temperature for ~15 min. First, 60 μL of the [Fe^{II}POP(H₂O)]⁻ stock solution was injected into the cuvette via airtight syringe and mixed for 150-200 sec to give the desired concentration (2 mM). Then, the reaction was initiated with injecting 80 μL (1 equiv.) of the IBX-iPr stock solution into the cuvette via airtight syringe while closely monitoring the formation of the 900 nm d-d transition that is indicative of formation of [Fe^{IV}POP(O)]⁻. Immediately after the 900 nm band reached maxima (t = 20-30 sec), 100-200 μL of the substrate stock solution (>10 equiv.) was injected into the cuvette via airtight syringe. The progress of the reaction was monitored by following the decrease in absorbance at 900 nm. The [Fe^{IV}POP(O)]⁻ complex has a self-decay rate and was measured at the same condition. After reaction was completed, the mixture in the cuvette ended as clear yellow solution.

Experiments for reaction at each concentration of substrate and determination of self-decay rate was repeated at least three times. Under these conditions, the substrate concentration was in excess compared to the complex concentration to provide pseudo first-order reaction conditions. The expression, $\ln[(A_t - A_f)/(A_i - A_f)]$, was plotted against the reaction time for the first three half-lives of any reaction to provide linear plots. Here, A_i is the initial absorbance, A_t is the absorbance at time t , and A_f is the absorbance at the endpoint of the reaction at 900 nm. The observed pseudo first-order rate constants (k_{obs} , s⁻¹)

for each reaction was determined from the slope/2 of the above-mentioned linear plots. The factor of 2 is necessary to account for the stoichiometry of the reaction: for the oxidation of one benzyl alcohol molecule, two equivalents of complexes were consumed.

Experiments where the substrate concentration was constant while varying the $[\text{Fe}^{\text{IV}}\text{POP}(\text{O})]^-$ complex concentration were performed to confirm the rate of the reaction is second order (Figure 4-S1). Therefore, the second-order rate law can be utilized (eq. 4-S1)

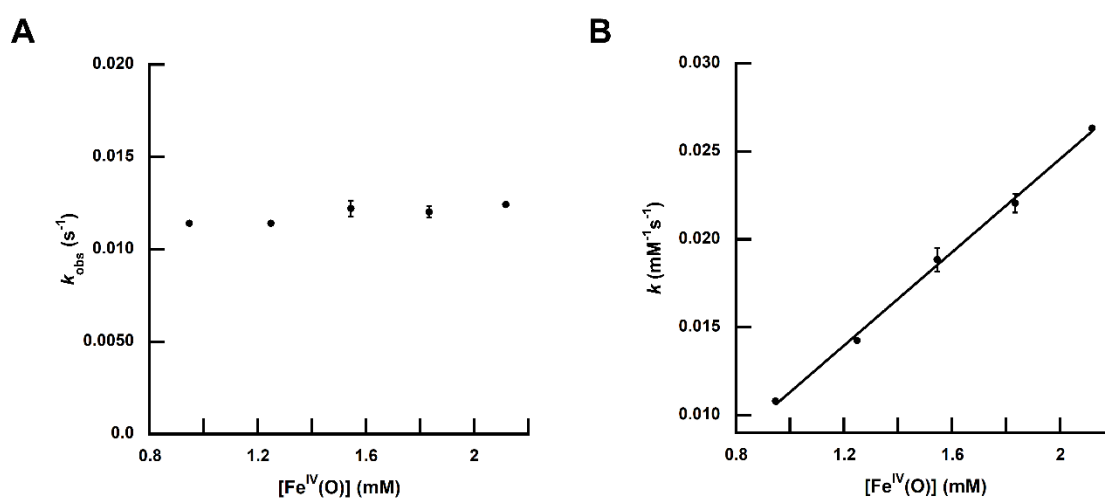


Figure 4-S1. Plot of k_{obs} vs. concentration of $[\text{Fe}^{\text{IV}}\text{POP}(\text{O})]^-$ complex and rate vs. concentration of $[\text{Fe}^{\text{IV}}\text{POP}(\text{O})]^-$ complex during the reaction of $[\text{Fe}^{\text{IV}}\text{POP}(\text{O})]^-$ complex with benzyl alcohol under pseudo-first order condition.



When k_{obs} for various concentrations of benzyl alcohol at $-20\text{ }^\circ\text{C}$ were plotted against the concentrations of benzyl alcohol, a linear dependence was observed. This is consistent with pseudo first-order reaction conditions as k_{obs} is expected to follow $k_{\text{obs}} = k_2[\text{DHA}]$, where k_2 is the second-order rate constant. The second-order rate constants were divided by 2 to normalize for the 2 chemically equivalent reactive C–H bonds per benzyl alcohol molecule to provide the corrected second-order rate constant k ($k = k_2/2$).

Correction for BDFE

For consistent comparison between reactivities with different substrates, reported BDE_{C-H} values of the substrates are corrected to $BDFE_{C-H}$ using equation (4-S2).⁵⁴

$$BDE_{\text{sol}(X-H)} = BDFE_{\text{sol}(X-H)} + (C_{H,\text{sol}} - C_{G,\text{sol}}) \quad \text{eq.(4-S2)}$$

Where $C_{H,\text{sol}}$ and $C_{G,\text{sol}}$ are constants that account for the thermodynamic properties of the hydrogen atom in a given solvent.

Preparation for GC-MS experiments

In a 20 mL vial, IBX-iPr (10.6 mg, 0.0329 mmol) was dissolved in 2 mL DMF and pre-chilled in an aluminum block in freezer at -20 °C for 30 min. The vial was taken out of the freezer while remained in the aluminum block to maintain the temperature when adding a pre-chilled mixture of $K[\text{Fe}^{\text{II}}\text{POP}]$ (33.8 mg, 0.0362 mmol) and 18C6 (16.7 mg, 0.0632 mmol) in 100 μL . The reaction solution was reacted for 10 min as the solution first turned red and ended as orange color. The organic compound in the reaction mixture was extracted with 2-3 mL pentane three times and solvent was removed under reduced pressure to result a colorless liquid. Half of the product was dissolved into 750 μL d_6 -DMSO for NMR measurements; the other half of the product was dissolved into 1 mL DCM as the stock solution and diluted by 30-fold for GC-MS measurements.

References

- (1) Groves, J. T.; McClusky, G. A. *J. Am. Chem. Soc.* **1976**, *98* (3), 859–861.
- (2) Groves, J. T. *J. Am. Chem. Soc.* **1985**, *62* (11), 924–927.
- (3) Green, M. T.; Dawson, J. H.; Gray, H. B. *Science (80-)*. **2004**, *304* (5677), 1653–1656.
- (4) Rittle, J.; Green, M. T. *Science (80-)*. **2010**, *330*, 933–937.
- (5) Price, J. C.; Barr, E. W.; Tirupati, B.; Bollinger, J. M.; Krebs, C. *Biochemistry* **2003**, *43* (4), 1134.
- (6) Price, J. C.; Barr, E. W.; Hoffart, L. M.; Krebs, C.; Bollinger, J. M. *Biochemistry* **2005**, *44* (22), 8138–8147.
- (7) Price, J. C.; Barr, E. W.; Glass, T. E.; Krebs, C.; Bollinger, J. M. *J. Am. Chem. Soc.* **2003**, *125* (43), 13008–13009.
- (8) Krebs, C.; Galonić Fujimori, D.; Walsh, C. T.; Bollinger, J. M. *Acc. Chem. Res.* **2007**, *40* (7), 484–492.
- (9) Decker, A.; Clay, M. D.; Solomon, E. I. *J. Inorg. Biochem.* **2006**, *100* (4), 697–706.
- (10) Fujimori, D. G.; Barr, E. W.; Matthews, M. L.; Koch, G. M.; Yonce, J. R.; Walsh, C. T.; Bollinger, J. M.; Krebs, C.; Riggs-Gelasco, P. J. *J. Am. Chem. Soc.* **2007**, *129* (44), 13408–13409.
- (11) Cook, S. A.; Borovik, A. S. *Acc. Chem. Res.* **2015**, *48* (8), 2407–2414.
- (12) Puri, M.; Que, L. *Acc. Chem. Res.* **2015**, *48* (8), 2443–2452.
- (13) Wang, D.; Ray, K.; Collins, M. J.; Farquhar, E. R.; Frisch, J. R.; Gómez, L.; Jackson, T. A.; Kerscher, M.; Waleska, A.; Comba, P.; Costas, M.; Que, L. *Chem. Sci.* **2013**, *4* (1), 282–291.
- (14) Pestovsky, O.; Stoian, S.; Bominaar, E. L.; Shan, X.; Münck, E.; Que, L.; Bakac, A. *Angew. Chemie - Int. Ed.* **2005**, *44* (42), 6871–6874.
- (15) England, J.; Guo, Y.; Farquhar, E. R.; Young, V. G.; Münck, E.; Que, L. *J. Am. Chem. Soc.* **2010**, *132* (25), 8635–8644.
- (16) England, J.; Martinho, M.; Farquhar, E. R.; Frisch, J. R.; Bominaar, E. L.; Münck, E.; Que, L. *Angew. Chemie - Int. Ed.* **2009**, *48* (20), 3622–3626.
- (17) Lacy, D. C.; Gupta, R.; Stone, K. L.; Greaves, J.; Ziller, J. W.; Hendrich, M. P.; Borovik, A. S. *J. Am. Chem. Soc.* **2010**, *132* (35), 12188–12190.
- (18) Gupta, R.; Lacy, D. C.; Bominaar, E. L.; Borovik, A. S.; Hendrich, M. P. *J. Am. Chem. Soc.* **2012**, *134* (23), 9775–9784.
- (19) Bigi, J. P.; Harman, W. H.; Lassalle-Kaiser, B.; Robles, D. M.; Stich, T. A.; Yano, J.; Britt, R. D.; Chang, C. J. *J. Am. Chem. Soc.* **2012**, *134* (3), 1536–1542.
- (20) England, J.; Guo, Y.; Van Heuvelen, K. M.; Cranswick, M. A.; Rohde, G. T.; Bominaar, E. L.; Münck, E.; Que, L. *J. Am. Chem. Soc.* **2011**, *133* (31), 11880–11883.
- (21) Biswas, A. N.; Puri, M.; Meier, K. K.; Oloo, W. N.; Rohde, G. T.; Bominaar, E. L.; Münck, E.; Que, L. *J. Am. Chem. Soc.* **2015**, *137* (7), 2428–2431.
- (22) Solomon, E. I.; Light, K. M.; Liu, L. V.; Srncic, M.; Wong, S. D. *Acc. Chem. Res.* **2013**, *46* (11), 2725–2739.
- (23) Que, L. J.; Ho, R. Y. N. *Chem. Rev.* **1996**, *96* (7), 2607–2624.
- (24) Dawson, J. H. *Science (80-)*. **1988**, *240* (4851), 433–439.
- (25) Shaw, W. J. *Catal. Rev. - Sci. Eng.* **2012**, *54* (4), 489–550.
- (26) Walsh, A. P.; Laureanti, J. A.; Katipamula, S.; Chambers, G. M.; Priyadarshani, N.; Lense, S.; Bays, J. T.; Linehan, J. C.; Shaw, W. J. *Faraday Discuss.* **2019**, *215*, 123–140.
- (27) Costas, M.; Mehn, M. P.; Jensen, M. P.; Que, L. *Chem. Rev.* **2004**, *104* (2), 939–986.
- (28) Casadei, C. M.; Gumiero, A.; Metcalfe, C. L.; Murphy, E. J.; Basran, J.; Concilio, M. G.; Teixeira, S. C. M.; Schrader, T. E.; Fielding, A. J.; Ostermann, A.; Blakeley, M. P.; Raven, E. L.; Moody, P. C. E. *Science (80-)*. **2014**, *345* (6193), 193–197.

- (29) Berggren, G.; Adamska, A.; Lambertz, C.; Simmons, T. R.; Esselborn, J.; Atta, M.; Gambarelli, S.; J-M., M.; Reijerse, E.; Lubitz, W.; Happe, T.; Artero, V.; Fontecave, M. *Nature* **2013**, *499*, 66–69.
- (30) Blasiak, L. C.; Vaillancourt, F. H.; Walsh, C. T.; Drennan, C. L. *Nature* **2006**, *440*, 368–371.
- (31) Groves, J. T. *J. Inorg. Biochem.* **2006**, *100* (4), 434–447.
- (32) Ono, T. A.; Rompel, A.; Mino, H.; Chiba, N. *Biophys. J.* **2001**, *81* (4), 1831–1840.
- (33) Boussac, A.; Rappaport, F.; Carrier, P.; Verbavatz, J. M.; Gobin, R.; Kirilovsky, D.; Rutherford, A. W.; Sugiura, M. *J. Biol. Chem.* **2004**, *279* (22), 22809–22819.
- (34) Borovik, A. S. *Acc. Chem. Res.* **2005**, *38* (1), 54–61.
- (35) Stone, K. L.; Borovik, A. S. *Curr. Opin. Chem. Biol.* **2009**, *13*, 114–118.
- (36) Cook, S. A.; Hill, E. A.; Borovik, A. S. *Biochemistry* **2015**, *54* (27), 4167–4180.
- (37) Taguchi, T.; Stone, K. L.; Gupta, R.; Kaiser-Lassalle, B.; Yano, J.; Hendrich, M. P.; Borovik, A. S. *Chem. Sci.* **2014**, *5* (8), 3064–3071.
- (38) Lacy, D. C.; Park, Y. J.; Ziller, J. W.; Yano, J.; Borovik, A. S. *J. Am. Chem. Soc.* **2012**, *134* (Chart 1), 17526–17535.
- (39) Oswald, V. F.; Lee, J. L.; Biswas, S.; Weitz, A. C.; Mittra, K.; Fan, R.; Li, J.; Zhao, J.; Hu, M. Y.; Alp, E. E.; Bominaar, E. L.; Guo, Y.; Green, M. T.; Hendrich, M. P.; Borovik, A. S. *J. Am. Chem. Soc.* **2020**, *142* (27), 11804–11817.
- (40) Weitz, A. C.; Hill, E. A.; Oswald, V. F.; Bominaar, E. L.; Borovik, A. S.; Hendrich, M. P.; Guo, Y. *Angew. Chemie - Int. Ed.* **2018**, *57* (49), 16010–16014.
- (41) MacBeth, C. E.; Golombek, A. P.; Young, J.; Yang, C.; Kuczera, K.; Hendrich, M. P.; Borovik, A. S. *Science* (80-.). **2000**, *289* (5481), 938–941.
- (42) Gupta, R.; Taguchi, T.; Lassalle-Kaiser, B.; Bominaar, E. L.; Yano, J.; Hendrich, M. P.; Borovik, A. S. *Proc. Natl. Acad. Sci. U. S. A.* **2015**, *112* (17), 5319–5324.
- (43) Shirin, Z.; Young, V. G.; Borovik, A. S. **1997**, *036* (1), 1967–1968.
- (44) Lacy, D. C. Dissertation, University of California-Irvine, 2012.
- (45) Usharani, D.; Lacy, D. C.; Borovik, A. S.; Shaik, S. *J. Am. Chem. Soc.* **2013**, *135* (45), 17090–17104.
- (46) Lau, N.; Ziller, J. W.; Borovik, A. S. *Polyhedron* **2015**, *85*, 777–782.
- (47) Matson, E. M.; Bertke, J. A.; Fout, A. R. *Inorg. Chem.* **2014**, *53* (9), 4450–4458.
- (48) Martinho, M.; Banse, F.; Bartoli, J. F.; Mattioli, T. A.; Battioni, P.; Horner, O.; Bourcier, S.; Girerd, J. J. *Inorg. Chem.* **2005**, *44* (25), 9592–9596.
- (49) Zarycz, M. N. C.; Fonseca Guerra, C. *J. Phys. Chem. Lett.* **2018**, *9* (13), 3720–3724.
- (50) Siskos, M. G.; Tzakos, A. G.; Gerothanassis, I. P. *Org. Biomol. Chem.* **2015**, *13* (33), 8852–8868.
- (51) Thomas, S. *Angew. Chemie Int. Ed.* **2002**, *41* (1), 48–76.
- (52) Dingley, A. J.; Cordier, F.; Grzesiek, S. *Concepts Magn. Reson.* **2001**, *13* (2), 103–127.
- (53) Bryant, J. R.; Mayer, J. M. *J. Am. Chem. Soc.* **2003**, *125* (34), 10351–10361.
- (54) Warren, J. J.; Tronic, T. A.; Mayer, J. M. *Chem. Rev.* **2010**, *110* (12), 6961–7001.
- (55) Markle, T. F.; Darcy, J. W.; Mayer, J. M. *Sci. Adv.* **2018**, *4* (7), 1–8.
- (56) Goetz, M. K.; Anderson, J. S. *J. Am. Chem. Soc.* **2019**, *141* (9), 4051–4062.
- (57) Brandi, P.; Galli, C.; Gentili, P. *J. Org. Chem.* **2005**, *70* (23), 9521–9528.
- (58) Koshino, N.; Cai, Y.; Espenson, J. H. *J. Phys. Chem. A* **2003**, *107* (21), 4262–4267.

- (59) Rhoda, R. N.; Fraioli, A. V.; Talor, W. L.; Kleinberg, J. *Inorg. Synth.* **1953**, *4*, 159–161.
- (60) Zhdankin, V. V.; Litvinov, D. N.; Kopusov, A. Y.; Luu, T.; Ferguson, M. J.; McDonald, R.; Tykwinski, R. R. *Chem. Commun.* **2004**, *4* (1), 106–107.
- (61) Zhdankin, V. V.; Kopusov, A. Y.; Litvinov, D. N.; Ferguson, M. J.; McDonald, R.; Luu, T.; Tykwinski, R. R. *J. Org. Chem.* **2005**, *70* (16), 6484–6491.
- (62) APEX3 Version 2014.1-1, Bruker AXS Inc: Madison, WI 2014.
- (63) SAINT Version 8.34a, Bruker AXS Inc: Madison, WI 2013.
- (64) Sheldrick, G. M. SADABS Version 2014/5, Bruker AXS, Inc: Madison 2014.
- (65) Sheldrick, G. M. SHELXTL Version 2014/7, Bruker AXS, Inc: Madison 2014.
- (66) Wilson, A. J. C.; Geist, V. *Cryst. Res. Technol.* **1993**, *28* (1), 110.
- (67) Oswald, V. F. Dissertation, University of California-Irvine, 2018.

Chapter 5 – Binding of α -keto Acids with Tripodal Iron Complexes

Introduction

α -Ketoglutarate (α -KG)-dependent dioxygenases is a class of non-heme iron enzymes that require α KG and O_2 for numerous catalysis such as hydroxylation, halogenation, epoxidation, etc.¹⁻⁸ For example, taurine dioxygenase (TauD), which was introduced in the previous chapter, contains an α KG bound Fe^{II} active site that can catalyze the hydroxylation of taurine in the presence of O_2 (Figure 5-1).¹⁻⁴ The α KG cofactor serves as a sacrificial reductant that drives the O_2 activation by the exothermic release of CO_2 . There are now several structural characterizations of α KG-dependent Fe enzymes that demonstrate that the α KG is coordinated to the Fe^{II} centers in a κ_2 manner.^{9,10}

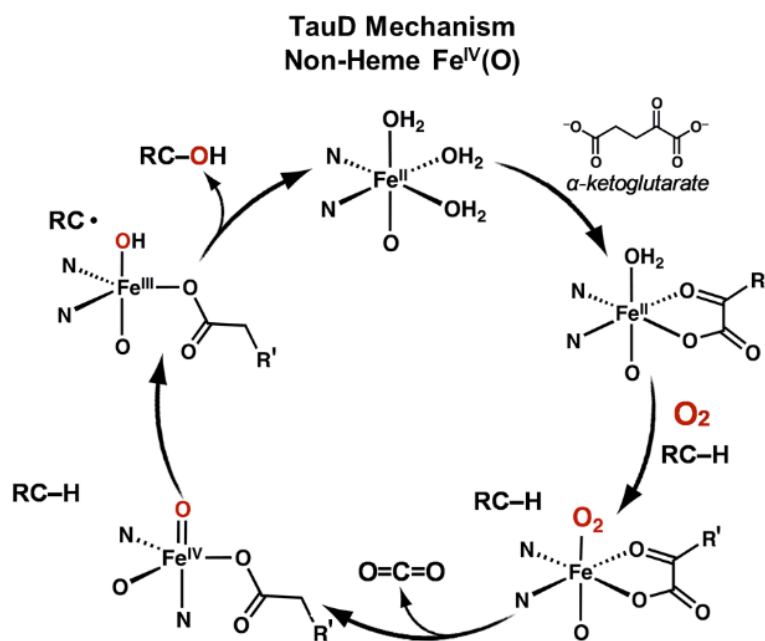


Figure 5-1. Mechanism of Taurine Dioxygenase (TauD).

Several synthetic Fe systems have been reported with bound α -keto acids, and their reactivities in the presence of O_2 were studied.¹¹⁻¹⁴ Work by Que¹¹

and Paine¹² (Figure 5-2) showed the abilities of these complexes to perform O₂ activation and substrate hydroxylation. The competent species for these reactions has been postulated to be an Fe^{IV}-oxido intermediate, which has yet to be experimentally identified in synthetic α -keto acid-bound Fe systems.

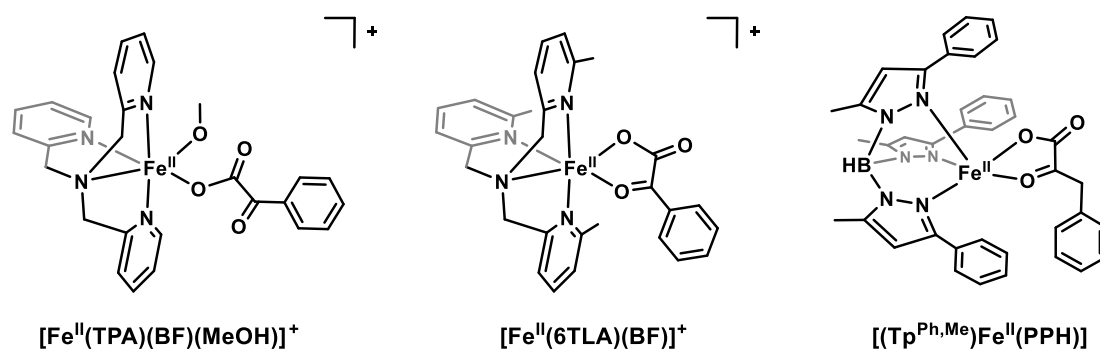


Figure 5-2. Examples of structurally characterized α -keto acids bound Fe^{II} complexes.

As introduced in Chapter 4, several C₃-symmetric tripodal ligand frameworks were developed in the Borovik lab with different design purposes and are capable of supporting an Fe^{IV}-oxido moiety (Figure 5-3).^{15,16} While the reactivity of [Fe^{IV}POP(O)]⁻ towards C-H bonds was discussed Chapter 4, further exploration for binding of α -keto acids to the iron complexes in these tripodal ligands and their effect on O₂ activation are of interest. In this chapter, several Fe^{II} complexes containing α -keto acid as exogenous ligands are characterized, and preliminary results of their reactivity towards O₂ are discussed.

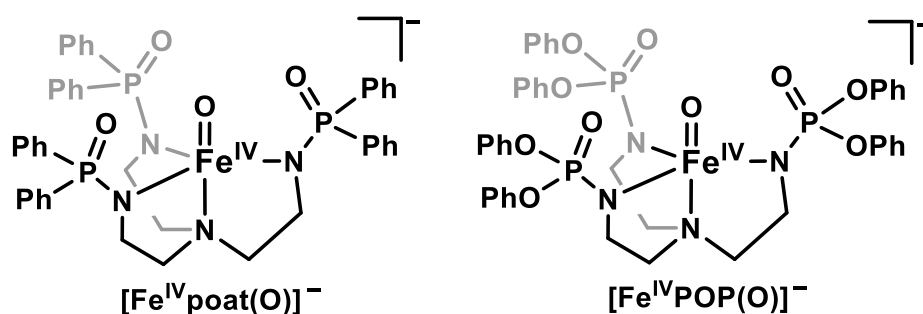


Figure 5-3. C₃-symmetric tripodal ligand frameworks developed in the Borovik lab hosting Fe^{IV}-oxido moiety: [Fe^{IV}poat(O)]⁻ and [Fe^{IV}POP(O)]⁻.

Result and Discussion

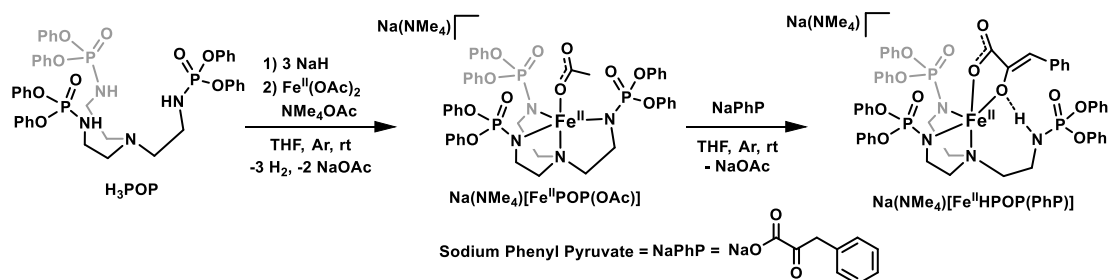
Preparations of Fe^{II}-OAc and Fe^{II}-PhP complexes

The Na(NMe₄)[Fe^{II}POP(OAc)] salt was synthesized serendipitously in an attempt to metathesize Na[Fe^{II}POP] with tetramethylammonium acetate (NMe₄OAc). This salt was synthesized by treating the precursor ligand H₃POP with 3 equiv. of NaH in tetrahydrofuran (THF) for 1 hour, and then allowing the resulting mixture to react with Fe^{II}(OAc)₂ and 1 equiv. of NMe₄OAc for another hour (Scheme 5-1). The insoluble salt (NaOAc) was removed via filtration, and the clear pale-yellow filtrate was layered under 2:1 pentane:diethyl ether (Et₂O) to obtain x-ray quality single crystals (>60%). Addition of >2 equiv. of NMe₄OAc produced identical product, which underscores the difficulty in removing the sodium counter ion due to its strong interactions with the P=O unit of the phosphoryl amido arms and the acetate ligand.

Amongst many Fe^{II} complexes developed within the Borovik lab, only two other Fe^{II}-OAc complexes¹⁷ have been structurally characterized (Figure 5-4): in both cases, steric hindrance is decreased in order to accommodate the binding of an acetate ligand. Similarly, the isolation of [Fe^{II}POP(OAc)]²⁻ complex supports the notion that the [POP]³⁻ ligand framework is flexible enough to allow an acetate ligand to access the iron center for coordination. Therefore, the presence of an acetate ligand bound to the iron center in the [POP]³⁻ ligand framework led to the exploration of other biologically relevant but bulkier exogenous ligand, such as α -keto acids.

The Na(NMe₄)[Fe^{II}HPOP(PhP)] salt was prepared using a similar procedure as the Na(NMe₄)[Fe^{II}POP(OAc)] salt with the following modifications: after the Na(NMe₄)[Fe^{II}POP(OAc)] salt was generated *in situ* as the clear pale-yellow solution as described above, 1 equiv. of sodium phenylpyruvate (NaPhP) was added. The reaction was stirred overnight which resulted in a heterogeneous dark red mixture. The mixture was filtered and solvent was

removed to produce a red solid (>70%). X-ray quality single crystals were obtained by redissolving the solid in THF and layering under 2:1 pentane:Et₂O.



Scheme 5-1. Synthesis of Na(NMe₄)[Fe^{II}POP(OAc)] and Na(NMe₄)[Fe^{II}HPOP(PhP)].

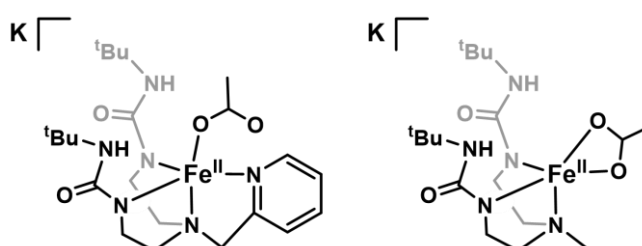


Figure 5-4. Two Fe^{II}-OAc complexes isolated in less sterically hindered ligand frameworks developed in the Borovik lab.

Structural Properties of Na(NMe₄)[Fe^{II}POP(OAc)] and Na(NMe₄)[Fe^{II}HPOP(PhP)]

{Na(NMe₄)[Fe^{II}POP(OAc)]₂}

The molecular structure of Na(NMe₄)[Fe^{II}POP(OAc)] was investigated using X-ray diffraction (XRD) methods. Similar to the K[Fe^{II}POP(H₂O)] complex described in Chapter 4, Na(NMe₄)[Fe^{II}POP(OAc)] recrystallizes as the cluster {Na(NMe₄)[Fe^{II}POP(OAc)]₂} with *C2/c* space group (Figure 5-5). Two [Fe^{II}POP(OAc)]²⁻ complexes are linked through two sodium ions via the oxygen atoms of the phosphoryl amido arms and the acetate ligand. The two (NMe₄)⁺ counter ions do not interact with the cluster. Each Fe^{II} center is five-coordinate having trigonal bipyramidal geometry. The Fe1–N1 and average Fe1–N_{equatorial} bond lengths are 2.278(2) and 2.086(2) Å, respectively; the average N1–Fe1–N_{equatorial} angle is 79.19(6)°. The Fe^{II} center is displaced 0.391 Å from the plane formed by the deprotonated phosphoryl nitrogen atoms toward the acetate

ligand. The acetate ligand is bound in a κ_1 -fashion to the Fe^{II} center in an axial coordination site with an Fe1-O1 bond length of 2.079(1) Å, which is consistent with other Fe^{II} -acetate complexes in trigonal bipyramidal geometry.^{14,17–19} For example, the Fe^{II} -acetate complex reported by Zart (Figure 5-4) with acetate ligand bound in a similar κ_1 -fashion to the Fe^{II} center has an Fe1-O1 bond lengths of 2.072(5) Å.¹⁷

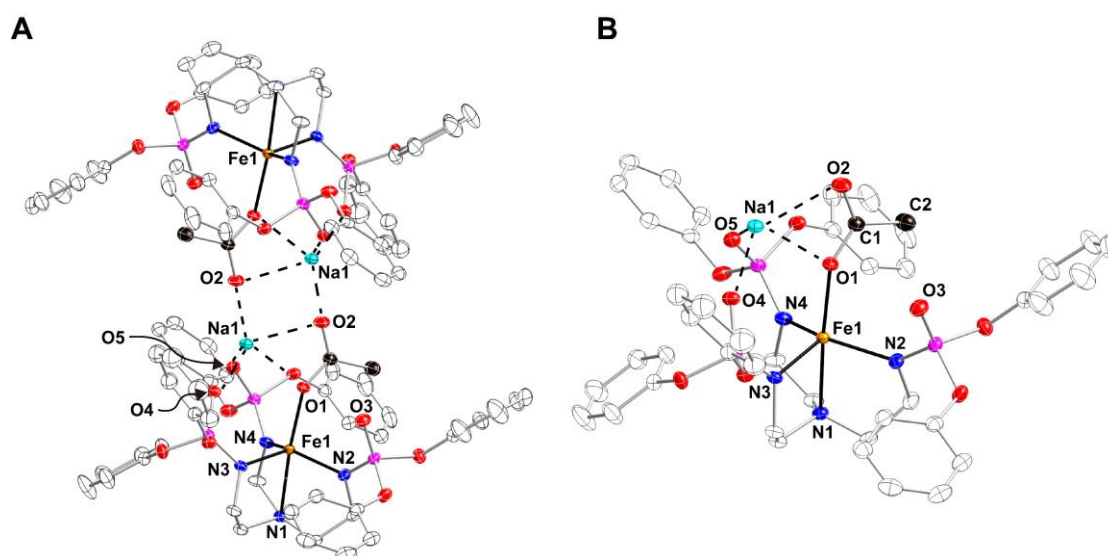


Figure 5-5. (A) Molecular structure of $\{\text{Na}(\text{NMe}_4)[\text{Fe}^{\text{II}}\text{POP}(\text{OAc})]\}_2$ and (B) view of $\text{Na}(\text{NMe}_4)[\text{Fe}^{\text{II}}\text{POP}(\text{OAc})]$ fragment determined by XRD methods. The carbon atoms on acetate ligand (C1 and C2) are highlighted to distinguish from other carbon atoms. Hydrogen atoms and $(\text{NMe}_4)^+$ counter ions were omitted for clarity. Ellipsoids are drawn at 50% probability.

$\{\text{Na}(\text{NMe}_4)[\text{Fe}^{\text{II}}\text{HPOP}(\text{PhP})]\}_2$

The molecular structure of $\text{Na}(\text{NMe}_4)[\text{Fe}^{\text{II}}\text{HPOP}(\text{PhP})]$ was investigated using X-ray diffraction (XRD) methods. Aggregation in the crystalline phase was also observed for $\text{Na}(\text{NMe}_4)[\text{Fe}^{\text{II}}\text{HPOP}(\text{PhP})]$ as the cluster $\{\text{Na}(\text{NMe}_4)[\text{Fe}^{\text{II}}\text{HPOP}(\text{PhP})]\}_2$ with $P\bar{1}$ space group (Figure 5-6). Two $[\text{Fe}^{\text{II}}\text{HPOP}(\text{PhP})]^{2-}$ complexes are linked through two sodium ions via the oxygen atoms in phosphoryl amido arms and the pyruvate ligand, with two outer sphere $(\text{NMe}_4)^+$ counter ions for charge balance. Each Fe^{II} center is five-coordinate in trigonal bipyramidal geometry. There are two crystallographically

different, but chemically equivalent, $\{\text{Na}(\text{NMe}_4)[\text{Fe}^{\text{II}}\text{HPOP}(\text{PhP})]\}_2$ molecules in the asymmetric unit and the average of their metrical parameters will be discussed.

Notably, an unusual coordination mode for the tetradentate $[\text{POP}]^{3-}$ ligand was observed upon binding of the phenylpyruvate ligand to the metal center. The phenylpyruvate group is bound as a bidentate, di-anionic enolate ligand $[\text{PhP}]^{2-}$ through two oxygen atoms (O1 and O2). The $[\text{PhP}]^{2-}$ moiety contains C2–C3 and C2–O2 bonds with distances of 1.344(4) and 1.341(4) Å, which are consistent with C=C and C–O bonds, respectively, and support the formulation of the enolate form. Meanwhile, one of the phosphoryl amido arms is now protonated at the N-position: this tripodal arm is no longer bound to the Fe center, with the N–H group forming an H-bond to the O2 atom of $[\text{PhP}]^{2-}$ ($d(\text{N2}\cdots\text{O2}) = 2.755(4)$ Å). The protonation of a phosphoryl amido arm was further corroborated by solid-state FTIR measurements, for which a feature of $\nu(\text{N–H}) = 3208 \text{ cm}^{-1}$ was observed. This vibrational feature has been observed in all other one arm protonated tripodal complexes in the $[\text{poat}]^{3-}$ or $[\text{POP}]^{3-}$ frameworks that was synthesized by Justin L. Lee and I. These observations suggest that upon binding to the metal center, the enol tautomer form of the $[\text{PhP}]^{2-}$ ligand could have a lower pK_a value^{20,21} than a phosphoryl amide tripodal arm, which can lead to intramolecular proton transfer to form the final product (Scheme 5-2). In addition to H-bonding, another non-covalent interaction was also observed in the molecular structure: the phenyl ring of $[\text{PhP}]^{2-}$ ligand is π -stacked with one of the phenyl rings in the protonated phosphoryl amide arm, with a centroid-centroid distance of 4.299 Å. The $[\text{Fe}^{\text{II}}\text{HPOP}(\text{PhP})]^{2-}$ complex is the first structurally characterized mononuclear Fe^{II} complex with a bound phenyl pyruvate in its enolate form.

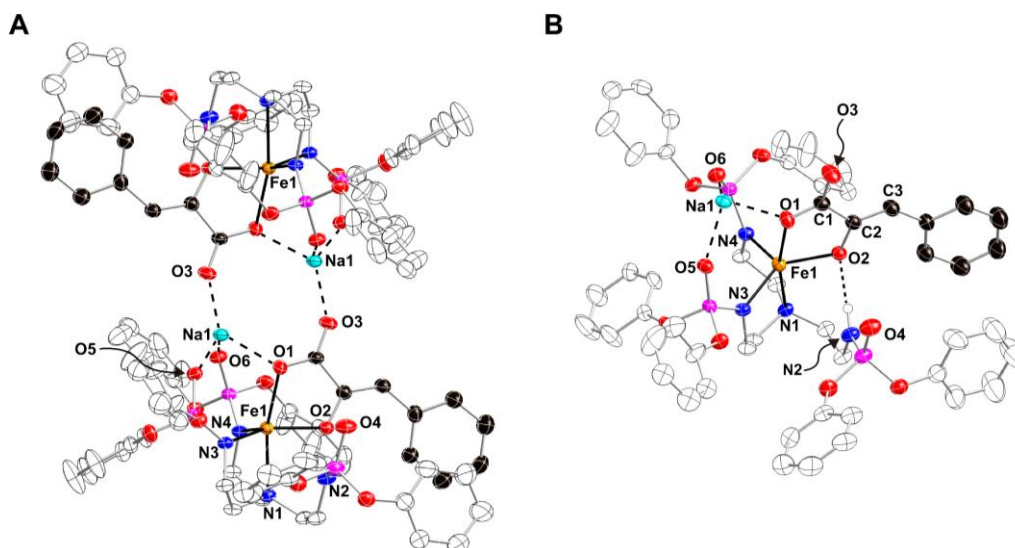
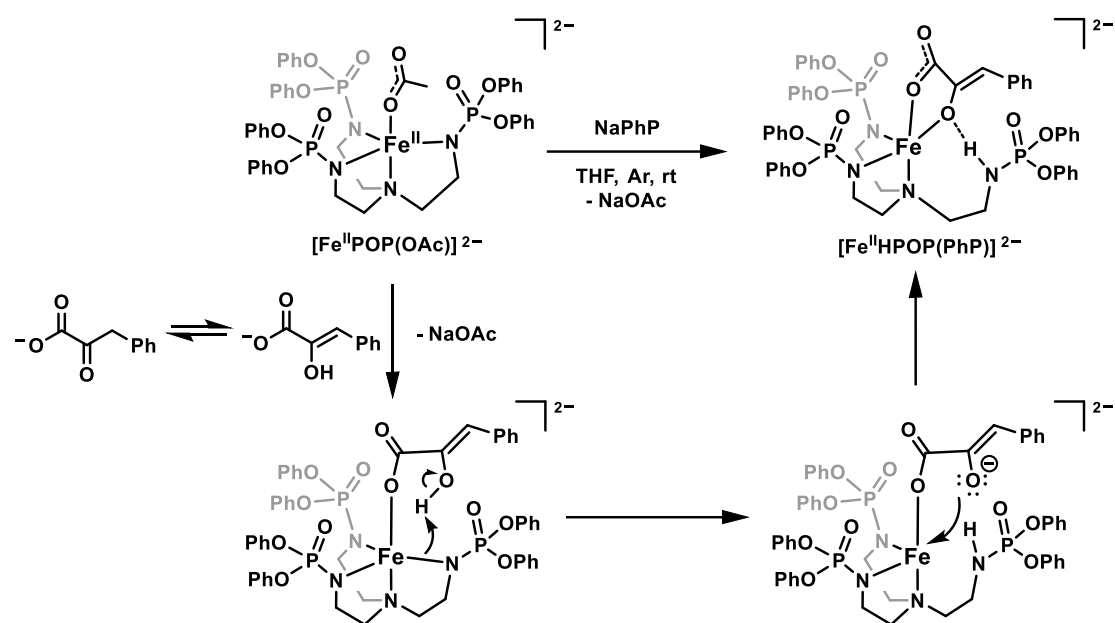


Figure 5-6. (A) Molecular structure of $\{\text{Na}(\text{NMe}_4)[\text{Fe}^{\text{II}}\text{HPOP}(\text{PhP})]\}_2$ and (B) view of $\text{Na}(\text{NMe}_4)[\text{Fe}^{\text{II}}\text{HPOP}(\text{PhP})]$ fragment determined by XRD methods. The carbon atoms on $[\text{PhP}]^{2-}$ ligand (C1, C2, C3, and the phenyl ring) are highlighted to distinguish from other carbon atoms. Hydrogen atoms and outer sphere $(\text{NMe}_4)^+$ counter ion were omitted for clarity. Ellipsoids are drawn at 50% probability. Only one orientation of the disordered components is shown. H-bonding in (A) is not shown due to congestion of the figure.

Table 5-1. Selected distances (\AA) and angles ($^\circ$) for $\text{Na}(\text{NMe}_4)[\text{Fe}^{\text{II}}\text{POP}(\text{OAc})]$ and $\text{Na}(\text{NMe}_4)[\text{Fe}^{\text{II}}\text{HPOP}(\text{PhP})]$.

Complex	$\{\text{Na}(\text{NMe}_4)[\text{Fe}^{\text{II}}\text{POP}(\text{OAc})]\}_2$	$\{\text{Na}(\text{NMe}_4)[\text{Fe}^{\text{II}}\text{HPOP}(\text{PhP})]\}_2^a$
<i>Distances (\AA)</i>		
Fe1–N1	2.278(2)	2.298(2)
Fe1–N2	2.073(2)	-
Fe1–N3	2.090(2)	2.061(2)
Fe1–N4	2.095(2)	2.050(2)
Fe1–O1	2.079(2)	2.109(2)
Fe1–O2	-	2.023(2)
C1–O1	1.267(2)	1.275(4)
C1–O2	1.253(2)	-
C1–O3	-	1.248(4)
C1–C2	1.506(3)	1.521(4)
C2–C3	-	1.344(4)
N2...O2	-	2.755(4)
Na1---O1	2.345(2)	2.283(2)
Na1---O2	2.242(2)	-
<i>Bond Angles ($^\circ$)</i>		
N1–Fe1–N2	79.08(6)	-
N1–Fe1–N3	79.32(6)	81.48(9)
N1–Fe1–N4	79.16(6)	80.95(9)

a. Distances (\AA) and angles ($^\circ$) are reported in average.



Scheme 5-2. Proposed intramolecular proton transfer to form the $[\text{Fe}^{\text{II}}\text{HPOP}(\text{PhP})]^{2-}$ complex.

Electronic Properties of $[\text{Fe}^{\text{II}}\text{POP}(\text{OAc})]^{2-}$ and $[\text{Fe}^{\text{II}}\text{HPOP}(\text{PhP})]^{2-}$

The $[\text{Fe}^{\text{II}}\text{POP}(\text{OAc})]^{2-}$ complex has no observable features in its UV-vis spectrum measured in DMF:THF. The parallel (//) - mode EPR spectrum of the $[\text{Fe}^{\text{II}}\text{POP}(\text{OAc})]^{2-}$ complex showed a $g = 9.20$ signal that is consistent with an $S = 2$ Fe^{II} complex (Figure 5-7).

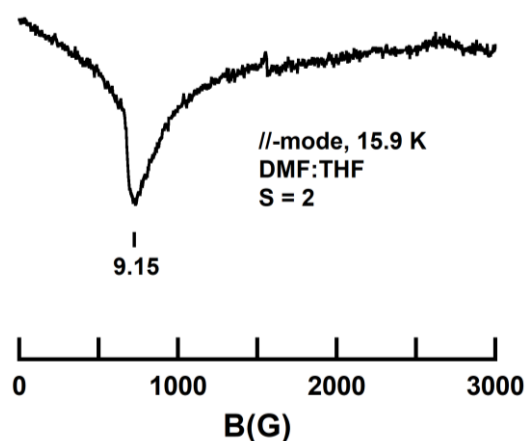


Figure 5-7. EPR spectrum (// - mode, 15.9 K, DMF:THF) of $[\text{Fe}^{\text{II}}\text{POP}(\text{OAc})]^{2-}$ complex (15.3 mM).

The $[\text{Fe}^{\text{II}}\text{HPOP}(\text{PhP})]^{2-}$ complex has electronic absorption features at $\lambda_{\text{max}}/\text{nm}$ ($\epsilon/\text{M}^{-1}\text{cm}^{-1}$) = 420 (360), 533 (110), 573 (75), 930 (8.2) (Figure 5-8A). These values are similar to what were reported for the synthetic examples by Que and Paine.¹¹⁻¹⁴ Most importantly, the 533 and 573 nm features are in the region characteristic of transitions arising from α -keto acids coordinating in a bidentate fashion to an Fe^{II} center in both synthetic and enzymatic systems. In the studies of clavamate synthase, Solomon and co-workers have assigned these absorption features as metal-to-ligand charge transfer (MLCT) transitions observed only when the α KG cofactor is bound bidentate to the metal center.²² Moreover, Solomon performed time-dependent density function theory (TD-DFT) calculation on Fe^{II} -keto and Fe^{II} -enolate forms of Fe^{II} phenylpyruvate complexes.²³ The TD-DFT results suggest that the Fe^{II} -enolate form is expected to have ligand-to-metal charge transfer (LMCT) transitions that are more red shifted compare to the Fe^{II} -keto form. This is supported by the experimental result of the $[\text{Fe}^{\text{II}}\text{HPOP}(\text{PhP})]^{2-}$ complex having absorption features with relatively higher energy, and the complex color is orange. Therefore, the absorption features of the $[\text{Fe}^{\text{II}}\text{HPOP}(\text{PhP})]^{2-}$ complex support the enolate binding in κ_2 -fashion, and are used for comparison in the later discussion of other complexes. In addition, the \parallel -mode EPR spectrum of the $[\text{Fe}^{\text{II}}\text{HPOP}(\text{PhP})]^{2-}$ complex showed a $g = 9.18$ signal that confirms the complex still contains an $S = 2$ Fe^{II} center (Figure 5-8B).

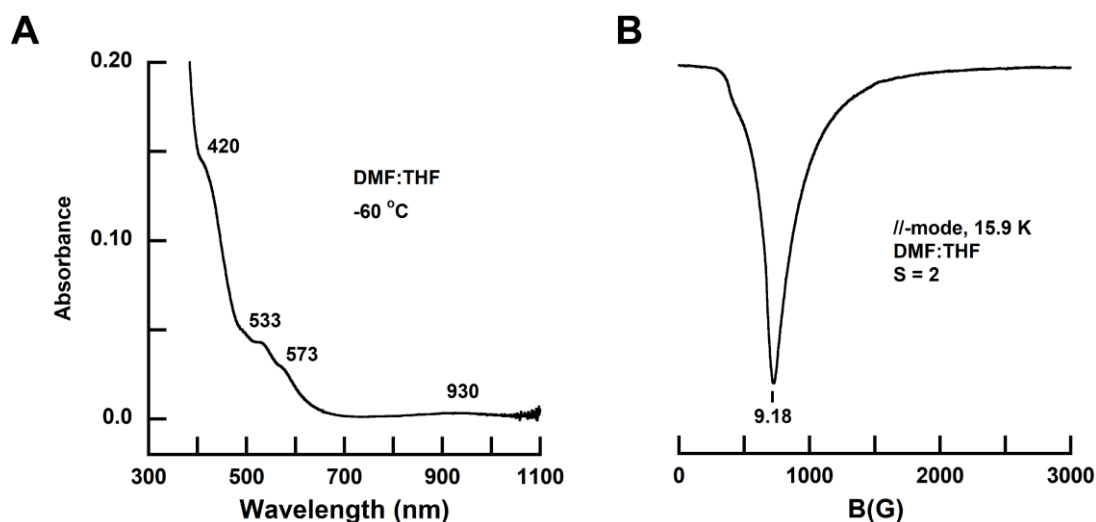
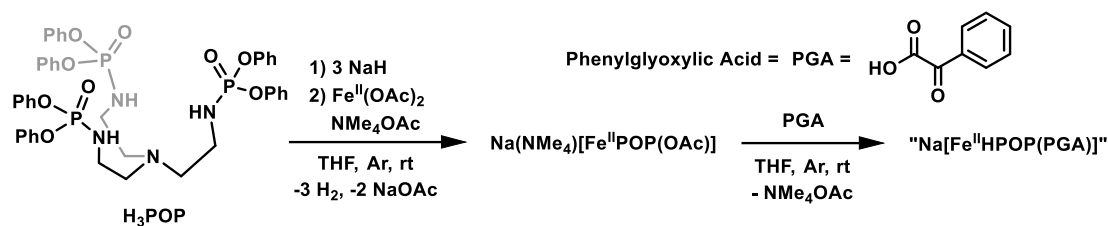


Figure 5-8. (A) Electronic absorption spectrum of $[\text{Fe}^{\text{II}}\text{POP}(\text{PhP})]^{2-}$ complex (0.39 mM) in DMF:THF at $-60\text{ }^{\circ}\text{C}$. (B) EPR spectrum (//-mode, 15.9 K, DMF:THF) of $[\text{Fe}^{\text{II}}\text{POP}(\text{PhP})]^{2-}$ complex (49.6 mM).

Binding of Phenylglyoxylic Acid (PGA)

To further investigate the binding of α -keto acids to the iron complex, phenylglyoxylic acid (PGA), which does not contain a benzylic $-\text{CH}_2-$ group and cannot tautomerize to an enolate form, was examined as an exogenous ligand. First, PGA was added instead of NaPhP in a similar synthetic route for $\text{Na}(\text{NMe}_4)[\text{Fe}^{\text{II}}\text{HPOP}(\text{PhP})]$ (Scheme 5-3). The resulting product contains similar optical features and EPR signal as the $[\text{Fe}^{\text{II}}\text{HPOP}(\text{PhP})]^{2-}$ complex (Figure 5-9). The UV-vis spectrum with $\lambda_{\text{max}} = 340, 564, 620\text{ nm}$ is consistent with bidentate coordination of an α -keto acid to the Fe^{II} center. Worth noting, the Fe^{II} -PGA complex is blue, and has 564 and 620 nm transitions that is lower energy than that of the $[\text{Fe}^{\text{II}}\text{HPOP}(\text{PhP})]^{2-}$ complex. This difference further supports the TD-DFT results from Solomon²³ because the PGA cannot tautomerize to enolate form, and therefore should have MLCT transitions attributed to binding of α -keto acids in κ_2 -fashion to Fe^{II} center at lower energy than the LMCT transitions of the $[\text{Fe}^{\text{II}}\text{HPOP}(\text{PhP})]^{2-}$ complex. The EPR spectrum showed a $g = 11.5$ signal, consistent with an $S = 2$ spin ground state. However, the significant differences in g values and signal shapes of the EPR

spectra between the Fe^{II} -PhP and Fe^{II} -PGA complexes suggest the two Fe^{II} complexes have different electronic structures.



Scheme 5-3. Synthesis of putative $[\text{Fe}^{\text{II}}\text{HPOP}(\text{PGA})]^-$ complex .

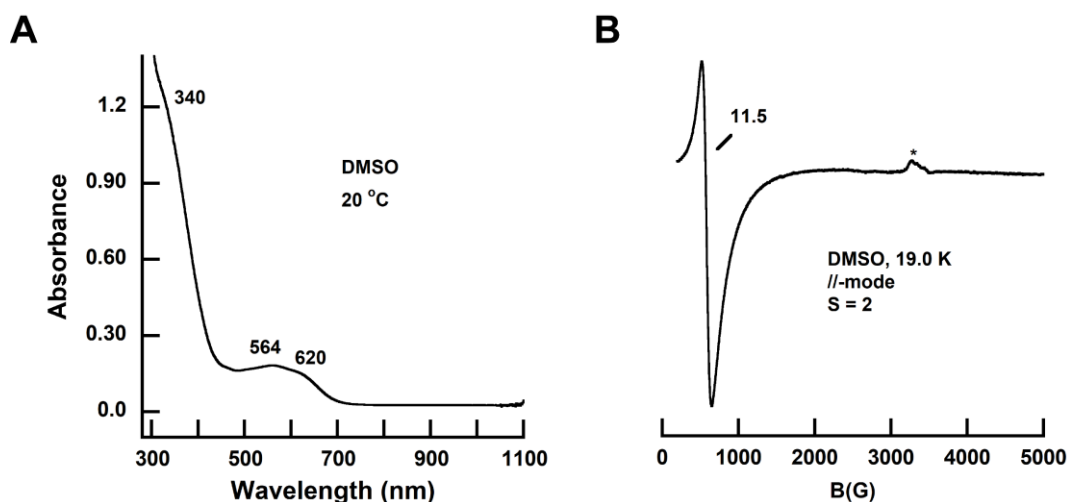


Figure 5-9. (A) Electronic absorption spectrum of putative Fe^{II} -PGA complex in DMSO at 20 °C (B) EPR spectrum ($//$ -mode, 19.0 K, DMSO) of Fe^{II} -PGA complex.

Attempts to grow single crystals of the putative Fe^{II} -PGA complex were unsuccessful. To gain structural insight of the Fe^{II} -PGA complex, the FTIR spectrum of the complex was measured. Similar to the $[\text{Fe}^{\text{II}}\text{HPOP}(\text{PhP})]^{2-}$ complex, the spectrum of Fe^{II} -PGA complex contains a $\nu(\text{N-H}) = 3208 \text{ cm}^{-1}$ (Figure 5-10) that suggests a phosphoryl amido arm was protonated. The protonation of anionic nitrogen is possibly due to PGA having a lower $\text{p}K_a$ value²⁴ than the conjugate acid of the $[\text{POP}]^{3-}$ ligand, which could result in intramolecular proton transfer as observed for $[\text{Fe}^{\text{II}}\text{HPOP}(\text{PhP})]^{2-}$. To examine this hypothesis, further experiments such as replacing PGA with sodium phenylglyoxylate (the conjugate base) during synthesis, or elemental analysis of the Fe^{II} -PGA complex are needed.

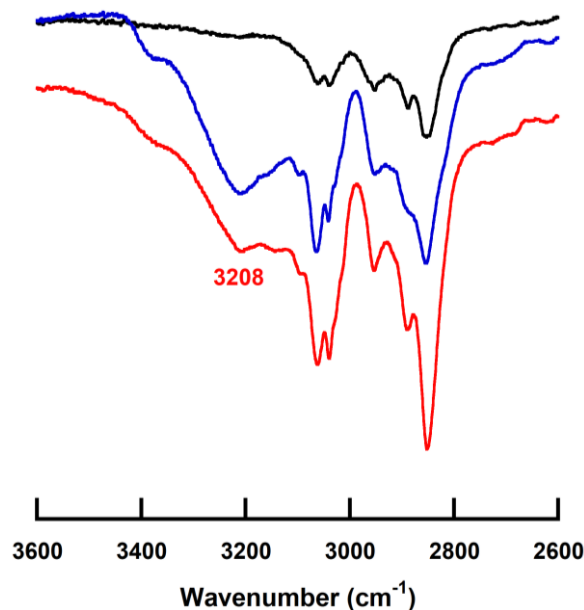


Figure 5-10. Solid state FTIR spectra of $\text{Na}(\text{NMe}_4)[\text{Fe}^{\text{II}}\text{POP}(\text{OAc})]$ (black), $\text{Na}(\text{NMe}_4)[\text{Fe}^{\text{II}}\text{HPOP}(\text{PhP})]$ (red), and the putative $[\text{Fe}^{\text{II}}\text{HPOP}(\text{PGA})]^-$ complex (blue).

For comparison, PGA was added to $\text{K}[\text{Fe}^{\text{II}}\text{poat}]$ (Chapter 2), and the reaction was monitored by UV-vis and EPR spectroscopies. The addition of PGA to a clear yellow solution of $\text{K}[\text{Fe}^{\text{II}}\text{POAT}]$ produced a blue precipitate. The blue precipitate was isolated and redissolved in DMSO to obtain a UV-vis spectrum with features at $\lambda_{\text{max}} = 377, 606, 670$ at 20 °C (Figure 5-11A). These features are similar in shape compared with the two α -keto acid bound Fe^{II} complexes in $[\text{POP}]^{3-}$ ligand framework, but the λ_{max} values of 606 and 670 nm correspond to binding of PGA are more blue shifted. The EPR spectrum of the blue product contains a signal with $g = 15.3$ (Figure 5-11B), which suggest possible aggregation of complexes in solution state. Similar to the Fe^{II} -PGA complex in the $[\text{POP}]^{3-}$ ligand framework, spectrophotometric changes after the addition of PGA to $[\text{Fe}^{\text{II}}\text{poat}]^-$ suggest possible binding of an α -keto acid to the iron center, but further synthesis and characterization (such as molecular structure, elemental analysis, and FTIR) are required to identify the putative $[\text{Fe}^{\text{II}}\text{Hpoat}(\text{PGA})]^-$ complex.

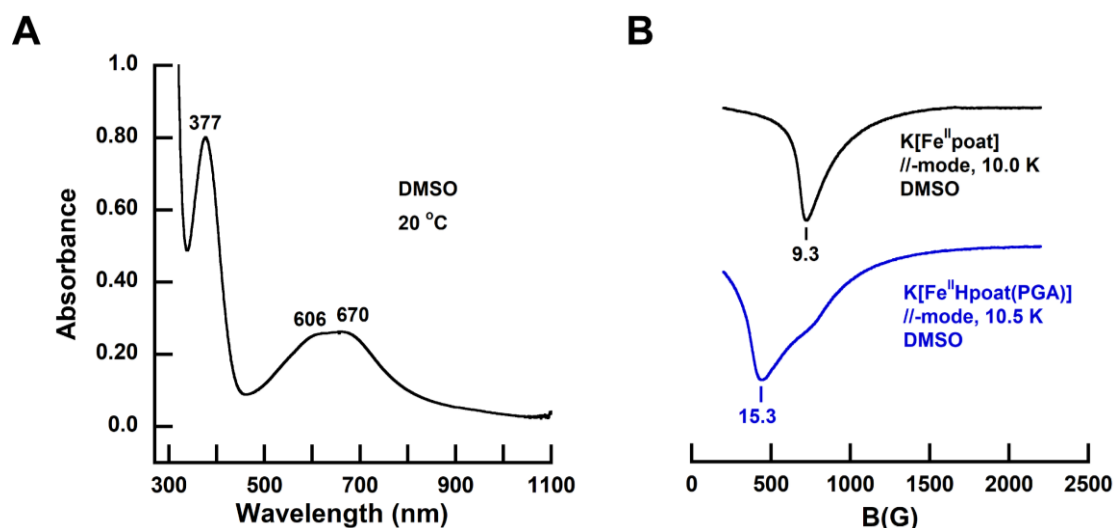


Figure 5-11. (A) Electronic absorption spectrum of the putative $[\text{Fe}^{\text{II}}\text{Hpoat}(\text{PGA})]^-$ complex collected in DMSO at 20 °C (B) EPR spectrum (//-mode, 19.0 K, DMSO) of the putative $[\text{Fe}^{\text{II}}\text{Hpoat}(\text{PGA})]^-$ complex.

Reactivity with O_2 and other oxidants

The reactivity of the $\text{Fe}^{\text{II}}\text{-}\alpha\text{-keto acid complexes}$ with dioxygen is of interest to model the O_2 binding and activation in TauD and other $\alpha\text{-KG}$ dependent enzymes. These reactions were monitored via UV-vis and EPR spectroscopies. First, O_2 was added to $[\text{Fe}^{\text{II}}\text{HPOP}(\text{PhP})]^{2-}$: the intensity of the two broad features at 537 and 578 nm increased while the feature at 930 nm decreased (Figure 5-12A). The EPR spectrum of the corresponding product showed no observable features in // -mode; the perpendicular(\perp)-mode EPR spectrum has g values of 4.3 and 9.3, which are consistent with a $S = 5/2$ Fe^{III} species (Figure 5-12B). When the same experiments were performed using the putative $[\text{Fe}^{\text{II}}\text{HPOP}(\text{PGA})]^-$ complex, the two broad optical features at 570 and 623 nm decreased slightly (Figure 5-13A), and spectrum with g values of 4.3 and 9.5 (corresponding to a $S = 5/2$ Fe^{III} species) in the \perp -mode EPR spectrum were observed (Figure 5-13B). Furthermore, addition of an oxygen atom transfer reagent, isopropyl 2-iodoxybenzoate (IBX-iPr), to both Fe^{II} complexes produced identical UV-vis spectra as the O_2 experiments, albeit with much longer reaction times.

The EPR spectra of both O₂ addition experiments suggest the generation of Fe^{III} species. However, the concentration of the Fe^{III} species has not been determined, and other experiments, such as temperature dependent EPR, Mössbauer, and resonance Raman spectroscopies, are required to probe the identity of the product(s).

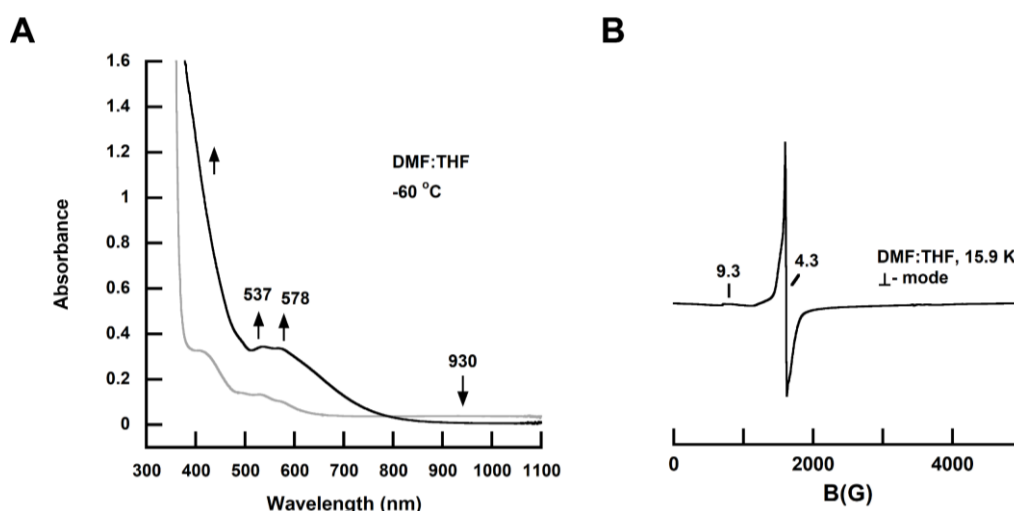


Figure 5-12. (A) Electronic absorption spectrum of [Fe^{II}HPOP(PhP)]²⁻ complex (grey) and 10 min after addition of 3 equiv. O₂ (black) in DMF:THF at -60 °C. (B) EPR spectrum (⊥-mode, 15.9 K, DMF:THF) after addition of 3 equiv. O₂ to the [Fe^{II}POP(PhP)]²⁻ complex.

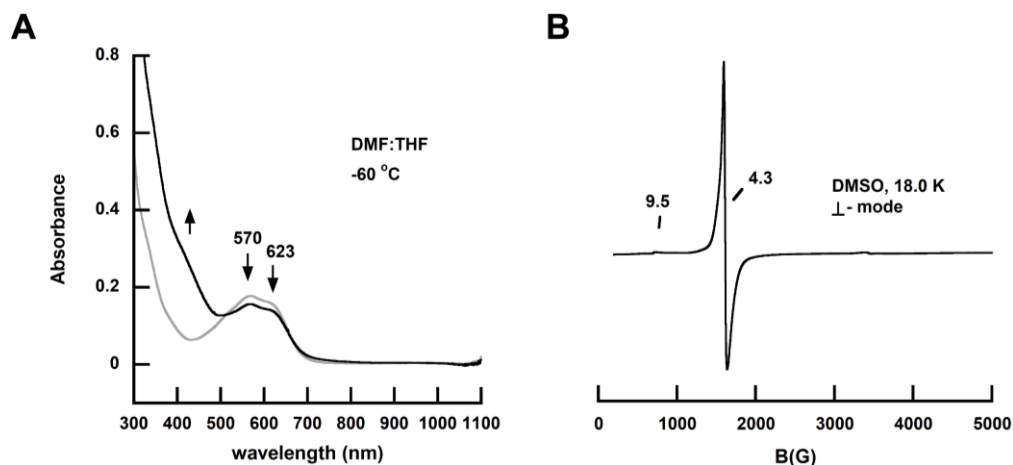


Figure 5-13. (A) Electronic absorption spectrum of the putative [Fe^{II}HPOP(PGA)]⁻ complex (grey) and 20 min after addition of 3 equiv. O₂ (black) in DMF:THF at -60 °C. (B) EPR spectrum (⊥-mode, 15.9 K, DMSO) after addition of 3 equiv. O₂ to the putative [Fe^{II}HPOP(PGA)]⁻ complex.

While dioxygen can bind to the Fe^{II} centers, O₂ can also serve as an outer sphere oxidant. In order to examine this possibility, ferrocenium tetrafluoroborate (FeCp₂BF₄) was used as the oxidant for comparison. After

addition of FeCp_2BF_4 to the $[\text{Fe}^{\text{II}}\text{HPOP}(\text{PhP})]^{2-}$ complex, similar features in the UV-vis spectrum were observed as O_2 addition (Figure 5-14A), except this reaction time was >10 times faster. After addition of FeCp_2BF_4 to the $[\text{Fe}^{\text{II}}\text{HPOP}(\text{PGA})]^-$ complex, a feature of $\lambda_{\text{max}} = 425$ nm was observed immediately with the concomitant disappearance of the 569 and 631 nm transitions (Figure 5-14B). Experiments (such as EPR spectroscopy) to monitor these oxidation reactions are needed for better understanding of the reaction.

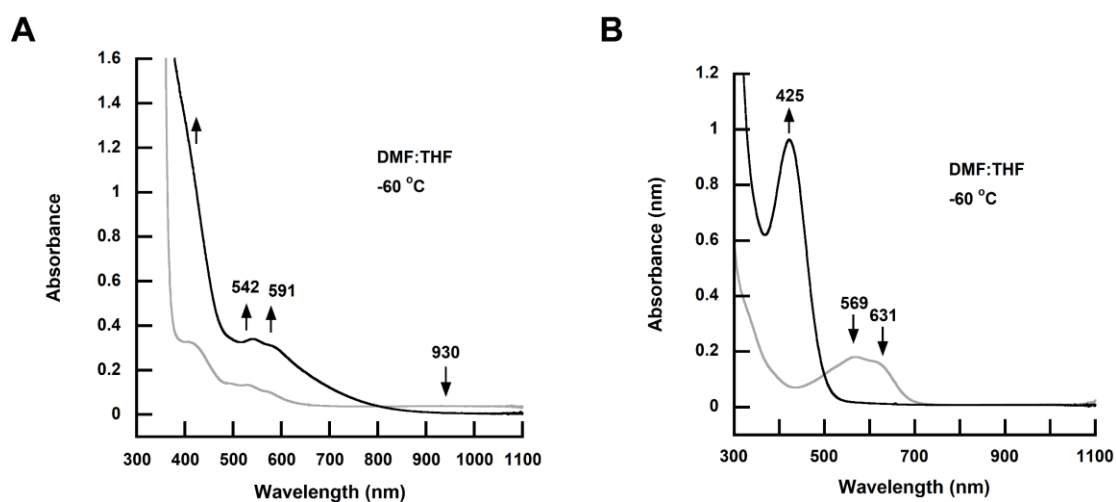


Figure 5-14. (A) Electronic absorption spectra of $[\text{Fe}^{\text{II}}\text{HPOP}(\text{PhP})]^{2-}$ complex (grey) and the reaction after addition of FeCp_2BF_4 (black) in DMF:THF at -60 °C. (B) Electronic absorption spectra of the putative $[\text{Fe}^{\text{II}}\text{HPOP}(\text{PGA})]^-$ complex (grey) and the reaction after addition of FeCp_2BF_4 (black) in DMF:THF at -60 °C.

When the putative $[\text{Fe}^{\text{II}}\text{Hpoat}(\text{PGA})]^-$ complex was treated with O_2 , the UV-vis spectrum of the reaction revealed new features at $\lambda_{\text{max}} = 466, 550, 755,$ and 1010 nm (Figure 5-15A). In particular, the low energy band at 1010 nm is often characteristic for the d-d transition observed in synthetic non-heme Fe^{IV} -oxido species. The EPR spectrum of the product revealed a signal at $g = 8.5$ (Figure 5-15B). Although it has a similar g value as high spin Fe^{IV} -oxido complexes in trigonal frameworks developed by the Borovik lab and other groups, the shape of the signal is significantly different. Further experiments are required to better identify the oxidation and spin state of the iron center.

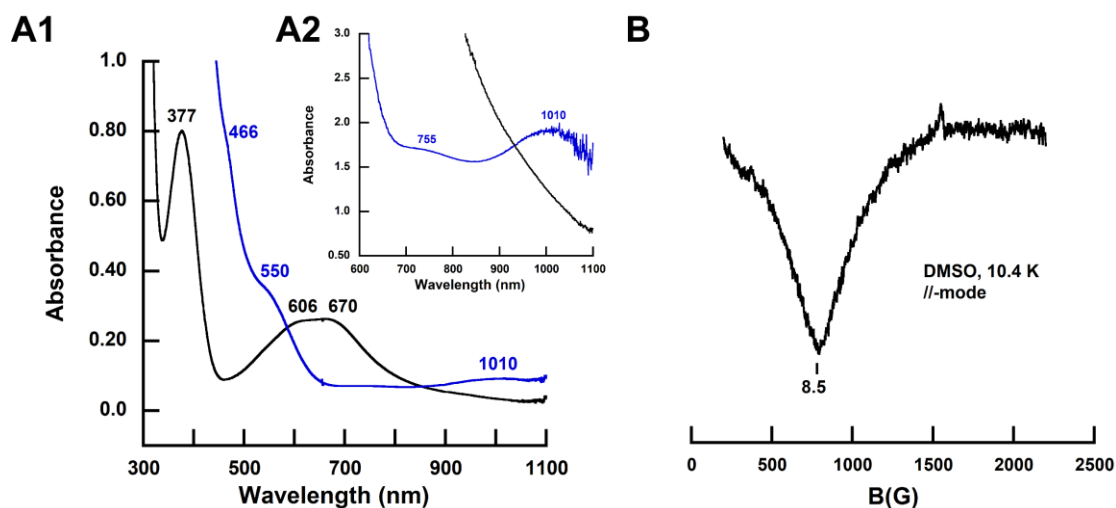


Figure 5-15. (A1) Electronic absorption spectra of the putative $[\text{Fe}^{\text{II}}\text{Hpoat}(\text{PGA})]^{1-}$ complex (black) and 33 min after addition of 3 equiv. O_2 (black) in DMSO at 20 °C. (A2) Electronic absorption spectra of the same reaction at 100 times higher concentration. (B) EPR spectrum (//-mode, 10.4 K, DMSO) of 33 min after addition of 3 equiv. O_2 to the putative $[\text{Fe}^{\text{II}}\text{Hpoat}(\text{PGA})]^{1-}$ complex.

Summary and Conclusion

In this chapter, synthesis and characterization of the $\text{Na}(\text{NMe}_4)[\text{Fe}^{\text{II}}\text{POP}(\text{OAc})]$ complex was described. The binding of an acetate ligand demonstrates the flexibility of the $[\text{POP}]^{3-}$ ligand framework to allow the iron center for coordination of sterically bulkier ligands. Therefore, the binding of α -keto acids to Fe^{II} metal center was investigated. The $\text{Na}(\text{NMe}_4)[\text{Fe}^{\text{II}}\text{HPOP}(\text{PhP})]$ complex was successfully synthesized and characterized using XRD methods, UV-vis, EPR, and FTIR spectroscopies. The structure of the $\text{Na}(\text{NMe}_4)[\text{Fe}^{\text{II}}\text{HPOP}(\text{PhP})]$ complex suggests intramolecular proton transfer resulted in the $[\text{PhP}]^{2-}$ ligand to bind in the enolate form, and one of the phosphoryl amido arm in $[\text{POP}]^{3-}$ ligand was protonated. Addition of PGA to Fe^{II} complexes in both $[\text{POP}]^{3-}$ and $[\text{poat}]^{3-}$ ligand frameworks showed possible binding, but additional experiments are still required to help identify the products. Reactivity of these complexes with O_2 and oxidants were examined, and the oxidation states of the metal center in these reactions are yet to be determined. Some important future experiments include monitoring the

production of CO₂, and determining the organic product(s) of these reactions: both are crucial to understand the role of the α-keto acid ligands in O₂ binding and activation. Addition of organic substrates should be investigated to detect possible hydroxylation or other reactivities.

Experimental

General procedure

Unless otherwise stated, all reactions were performed under an argon atmosphere in a Vacuum Atmospheres Co. dry box. Solvents were sparged with argon and dried over columns containing Q-5 and molecular sieves. Fe^{II}(OAc)₂²⁵ and FeCp₂BF₄²⁶ were synthesized following literature procedures and stored under Ar atmosphere at room temperature. Sodium hydride as a 57-63% suspension in mineral oil was filtered with a medium pore size glass fritted funnel and washed with 10 mL pentane and 10 mL Et₂O five times each or until the powder is white, then dried under vacuum and stored under Ar atmosphere at room temperature. H₃POP and H₃poat are synthesized using procedures described in Chapter 3 and 4. Phenylglyoxylic acid (PGA) was purchased from Sigma-Aldrich and used without further purification. Sodium phenylpyruvate (NaPhP) was purchased from Alfa Aeser and used without further purification. Tetramethylammonium acetate (NMe₄OAc) was purchased from Sigma-Aldrich, dried under heat and vacuum for several days, and stored under Ar atmosphere.

Physical methods

All electronic absorption spectra were collected in a 1 cm quartz cuvette with a magnetic spin bar inside. Electronic absorption spectra were recorded on an 8453E Agilent UV-vis spectrometer equipped with an Unisoku Unispeks cryostat. X-band EPR spectra were recorded as frozen solutions either using a Bruker EMX spectrometer equipped with an ER041XG microwave bridge, an

Oxford Instrument liquid-helium quartz cryostat, and a dual-mode cavity (ER4116DM), or using a Bruker ELEXSYS spectrometer equipped with an Oxford ESR-910 liquid helium cryostat and a Bruker bimodal cavity for the generation of microwave fields parallel and transverse to the applied magnetic field. The microwave frequency was calibrated with a frequency counter, and the magnetic field was measured with an NMR gaussmeter. The sample temperature was calibrated against a calibrated cernox sensor (Lakeshore CX-1050) mounted inside an EPR tube. A modulation frequency of 100 kHz was used for all EPR spectra. The simulation software SpinCount was written Professor Michael Hendrich at Carnegie Mellon University. Solid-state IR spectra were collected on a Thermo Scientific Nicolet iS5 FT-IR spectrometer equipped with an iD5 ATR accessory.

X-ray crystallography

{Na(NMe₄)[Fe^{II}POP(OAc)]}₂

A colorless crystal of approximate dimensions 0.317 x 0.282 x 0.246 mm was mounted in a cryoloop and transferred to a Bruker SMART APEX II diffractometer. The APEX2²⁷ program package was used to determine the unit-cell parameters and for data collection (40 sec/frame scan time for a sphere of diffraction data). The raw frame data was processed using SAINT²⁸ and SADABS²⁹ to yield the reflection data file. Subsequent calculations were carried out using the SHELXTL³⁰ program. The diffraction symmetry was *2/m* and the systematic absences were consistent with the monoclinic space groups *Cc* and *C2/c*. It was later determined that space group *C2/c* was correct.

The structure was solved by dual space methods and refined on F^2 by full-matrix least-squares techniques. The analytical scattering factors³¹ for neutral atoms were used throughout the analysis.

Hydrogen atoms were included using a riding model. The structure was a dimer located about an inversion center. There was one tetrahydrofuran

solvent molecule per dimeric formula-unit. Several disordered atoms were included as isotropic atoms using multiple components with partial site-occupancy factors.

Least-squares analysis yielded $wR2 = 0.1130$ and $Goof = 1.030$ for 665 variables refined against 13573 data (0.74 \AA), $R1 = 0.0421$ for those 11449 data with $I > 2.0\sigma(I)$.

Table 5-S1. Metric parameters for $\{\text{Na}(\text{NMe}_4)[\text{Fe}^{\text{II}}\text{POP}(\text{OAc})]\}_2$ and $\{\text{Na}(\text{NMe}_4)[\text{Fe}^{\text{II}}\text{HPOP}(\text{PhP})]\}_2$.

Complex	$\{\text{Na}(\text{NMe}_4)[\text{Fe}^{\text{II}}\text{POP}(\text{OAc})]\}_2$	$\{\text{Na}(\text{NMe}_4)[\text{Fe}^{\text{II}}\text{HPOP}(\text{PhP})]\}_2$
Empirical Formula	$\text{C}_{104}\text{H}_{130}\text{Fe}_2\text{N}_{10}\text{Na}_2\text{O}_{24}\text{P}_6$	$\text{C}_{118}\text{H}_{141}\text{Fe}_2\text{N}_{10}\text{Na}_2\text{O}_{26}\text{P}_6$
Fw	2247.67	2458.94
T (K)	133(2)	93(2)
Crystal system	Monoclinic	Triclinic
Space group	$C2/c$	$P\bar{1}$
a (\AA)	28.607(5)	17.059(1)
b (\AA)	16.019(3)	20.071(1)
c (\AA)	24.095(4)	20.942(1)
α ($^\circ$)	90	67.814(1)
β ($^\circ$)	92.191(2)	80.711(1)
γ ($^\circ$)	90	80.085(1)
V (\AA^3)	11033(3)	6503.3(6)
Z	4	2
δ_{calcd} (Mg/m^3)	1.353	1.256
GOF on F^2	1.030	1.048
R1	0.0421	0.0676
wR2	0.1130	0.1895

Synthesis of $\text{Na}(\text{NMe}_4)[\text{Fe}^{\text{II}}\text{POP}(\text{OAc})]$

To a clear colorless solution of H_3POP (599.8 mg, 0.7117 mmol) in 12 mL THF, NaH (52.0 mg, 2.17 mmol) was added and stirred for 1 hour or until gas evolution ceased. $\text{Fe}(\text{OAc})_2$ (256.2 mg, 1.473 mmol) and NMe_4OAc (95.0 mg, 0.713 mmol) were added to the reaction mixture, resulting in immediate change to a white cloudy solution. After stirring for 1 hour, the insoluble salt (NaOAc) was filtered off through a medium pore size frit, and the resulting clear pale-

yellow solution was dried to produce a pale brown solid (crude, 715.6 mg, 95.60 %) under vacuum. The crude solid was redissolved in 4 mL THF and layered under 2:1 pentane:Et₂O. Colorless x-ray quality single crystals of the desired product were obtained after 2 days (505.2 mg, 67.49 %) and the dried product was stored under Ar atmosphere. EPR (X-band, // -mode, 1:1 DMF:THF, 15.9 K): g = 9.20. FTIR (Diamond ATR, cm⁻¹): 3060, 3037, 2951, 2888, 2847, 1592, 1574, 1485, 1453, 1442, 1408, 1289, 1268, 1255, 1242, 1225, 1203, 1161, 1134, 1121, 1067, 1050, 1044, 1025, 1003, 983, 875, 812, 777, 757, 733, 711, 690, 654, 621, 612, 573, 539, 530, 526, 523, 519, 514.

Synthesis of Na(NMe₄)[Fe^{II}HPOP(PhP)]

To a clear colorless solution of H₃POP (600.7 mg, 0.7128 mmol) in 12 mL THF, NaH (52.0 mg, 2.17 mmol) was added and stirred for 1 hour or until gas evolution ceased. Fe(OAc)₂ (130.2 mg, 0.7486 mmol) and NMe₄OAc (99.4 mg, 0.746 mmol) were added to the reaction mixture, resulting in immediate change to a white cloudy solution. After stirring for 1 hour, the insoluble salt (NaOAc) was filtered off through a medium pore size frit, and NaPhP (136.2 mg, 0.7317 mmol) was added and let react overnight due to poor solubility of NaPhP in THF. After the overnight reaction, the solution turned to a dark red heterogenous mixture. The mixture was filtered through a medium pore size frit and the resulting clear red solution was dried to produce a red foam under reduced pressure (573.9 mg, 69.66 %). Red x-ray quality single crystals can be obtained after redissolving the solid in THF and layering under 2:1 pentane:Et₂O for 2 days. EPR (X-band, // -mode, 1:1 DMF:THF, 15.9 K): g = 9.18. UV-vis (DMF:THF, -60 °C): λ_{max}/nm(ε/M⁻¹cm⁻¹) = 540 (360), 533 (110), 573 (75), 930 (8.2). FTIR (Diamond ATR, cm⁻¹): 3207, 3061, 3039, 2953, 2852, 1587, 1485, 1454, 1442, 1401, 1353, 1285, 1261, 1199, 1160, 1121, 1070, 1044, 1024, 1004, 984, 881, 811, 757, 737, 688, 620, 615. Elemental analysis calcd for C₅₅H₆₄FeN₅NaO₁₂P₃·2.5NaOAc: C, 52.84; H, 5.28; N, 5.13 %, found: C, 52.74;

H, 4.91; N, 4.87 %.

Synthesis of the putative Na[Fe^{II}HPOP(PGA)]

To a clear colorless solution of H₃POP (400.4 mg, 0.4751 mmol) in 8 mL THF, NaH (34.9 mg, 1.45 mmol) was added and stirred for 1 hour or until gas evolution ceased. Fe(OAc)₂ (86.8 mg, 0.99 mmol) and NMe₄OAc (65.9 mg, 0.495 mmol) were added to the reaction mixture, resulting in immediate change to a white cloudy solution. After stirring for 1 hour, the insoluble salt (NaOAc) was filtered off through a medium pore size frit, and PGA (76.3 mg, 0.508 mmol) was added. After stirring overnight, the reaction solution turned into a dark blue heterogenous mixture. The mixture was filtered through a medium pore size frit, and the solvent of the clear blue filtrate was removed under reduced pressure. The resulted blue foam was triturated with 4 mL Et₂O (474.3 mg). EPR (X-band, // -mode, 1:1 DMF:THF, 19.0 K): g = 11.5. UV-vis (DMSO, 20 °C): λ_{max}/nm = 377, 606, 670. FTIR (Diamond ATR, cm⁻¹): 3207, 3064, 3041, 2952, 2852, 1659, 1588, 1486, 1454, 1414, 1256, 1191, 1161, 1110, 1170, 1025, 1006, 984, 917, 888, 816, 756, 688, 615.

Synthesis of putative K[Fe^{II}Hpoat(PGA)]

To a clear yellow solution of K[Fe^{II}poat] in 1:4 THF:Et₂O, solid PGA was slowly added and a blue precipitate formed immediately. The PGA solid was added until the clear yellow solution is close to colorless. The blue precipitate was collected on a fine pore size frit and dried under reduced pressure. EPR (X-band, // -mode, DMSO, 10.5 K): g = 15.3. UV-vis (DMSO, 20 °C): λ_{max}/nm = 377, 606, 670.

References

- (1) Price, J. C.; Barr, E. W.; Tirupati, B.; Bollinger, J. M.; Krebs, C. *Biochemistry* **2003**, *43* (4), 1134.
- (2) Price, J. C.; Barr, E. W.; Hoffart, L. M.; Krebs, C.; Bollinger, J. M. *Biochemistry* **2005**, *44* (22), 8138–8147.
- (3) Price, J. C.; Barr, E. W.; Glass, T. E.; Krebs, C.; Bollinger, J. M. *J. Am. Chem. Soc.* **2003**, *125* (43), 13008–13009.
- (4) Krebs, C.; Galonić Fujimori, D.; Walsh, C. T.; Bollinger, J. M. *Acc. Chem. Res.* **2007**, *40* (7), 484–492.
- (5) Blasiak, L. C.; Vaillancourt, F. H.; Walsh, C. T.; Drennan, C. L. *Nature* **2006**, *440*, 368–371.
- (6) Srnec, M.; Wong, S. D.; Matthews, M. L.; Krebs, C.; Bollinger, J. M.; Solomon, E. I. *J. Am. Chem. Soc.* **2016**, *138* (15), 5110–5122.
- (7) Martinie, R. J.; Livada, J.; Chang, W. C.; Green, M. T.; Krebs, C.; Bollinger, J. M.; Silakov, A. *J. Am. Chem. Soc.* **2015**, *137* (21), 6912–6919.
- (8) Li, J.; Liao, H. J.; Tang, Y.; Huang, J. L.; Cha, L.; Lin, T. S.; Lee, J. L.; Kurnikov, I. V.; Kurnikova, M. G.; Chang, W. C.; Chan, N. L.; Guo, Y. *J. Am. Chem. Soc.* **2020**, *142* (13), 6268–6284.
- (9) O'Brien, J. R.; Schuller, D. J.; Yang, V. S.; Dillard, B. D.; Lanzilotta, W. N. *Biochemistry* **2003**, *42* (19), 5547–5554.
- (10) Elkins, J. M.; Ryle, M. J.; Clifton, I. J.; Dunning Hotopp, J. C.; Lloyd, J. S.; Burzlaff, N. I.; Baldwin, J. E.; Hausinger, R. P.; Roach, P. L. *Biochemistry* **2002**, *41* (16), 5185–5192.
- (11) Chiou, Y.; Que, L. J. *J. Am. Chem. Soc.* **1995**, *117*, 3999–4013.
- (12) Sheet, D.; Bhattacharya, S.; Paine, T. K. *Chem. Commun.* **2015**, *51* (36), 7681–7684.
- (13) Hikichi, S.; Ogihara, T.; Fujisawa, K.; Kitajima, N.; Akita, M.; Moro-oka, Y. *Inorg. Chem.* **1997**, *36* (20), 4539–4547.
- (14) Mehn, M. P.; Fujisawa, K.; Hegg, E. L.; Que, L. *J. Am. Chem. Soc.* **2003**, *125* (26), 7828–7842.
- (15) Lacy, D. C.; Gupta, R.; Stone, K. L.; Greaves, J.; Ziller, J. W.; Hendrich, M. P.; Borovik, A. S. *J. Am. Chem. Soc.* **2010**, *132* (35), 12188–12190.
- (16) Oswald, V. F.; Lee, J. L.; Biswas, S.; Weitz, A. C.; Mittra, K.; Fan, R.; Li, J.; Zhao, J.; Hu, M. Y.; Alp, E. E.; Bominaar, E. L.; Guo, Y.; Green, M. T.; Hendrich, M. P.; Borovik, A. S. *J. Am. Chem. Soc.* **2020**, *142* (27), 11804–11817.
- (17) Zart, M. K.; Sorrell, T. N.; Powell, D.; Borovik, A. S. *Dalt. Trans.* **2003**, No. 10, 1986–1992.
- (18) Will, J.; Schneider, L.; Becker, J.; Becker, S.; Miska, A.; Gawlig, C.; Schindler, S. *Isr. J. Chem.* **2020**, *60* (10–11), 999–1003.
- (19) Kitajima, N.; Tamura, N.; Amagai, H.; Fukui, H.; Moro-oka, Y.; Mizutani, Y.; Kitagawa, T.; Mathur, R.; Heerwegh, K.; Reed, C. A.; Randall, C. R.; Que, L. J.; Tatsumi, K. *J. Am. Chem. Soc.* **1994**, *116* (20), 9071–9085.

- (20) Johnson, W. H.; Czerwinski, R. M.; Stamps, S. L.; Whitman, C. P. *Biochemistry* **1999**, *38* (48), 16024–16033.
- (21) Stamps, S. L.; Fitzgerald, M. C.; Whitman, C. P. *Biochemistry* **1998**, *37* (28), 10195–10202.
- (22) Pavel, E. G.; Zhou, J.; Busby, R. W.; Gunsior, M.; Townsend, C. A.; Solomon, E. I. *J. Am. Chem. Soc.* **1998**, *120* (4), 743–753.
- (23) Diebold, A. R.; Straganz, G. D.; Solomon, E. I. *J. Am. Chem. Soc.* **2011**, *133* (40), 15979–15991.
- (24) Lopalco, A.; Douglas, J.; Denora, N.; Stella, V. J. *J. Pharm. Sci.* **2016**, *105* (2), 664–672.
- (25) Rhoda, R. N.; Fraioli, A. V.; Talor, W. L.; Kleinberg, J. *Inorg. Synth.* **1953**, *4*, 159–161.
- (26) Connelly, N. G.; Geiger, W. E. *Chem. Rev.* **1996**, *96* (2), 877–910.
- (27) APEX3 Version 2014.1-1, Bruker AXS Inc: Madison, WI 2014.
- (28) SAINT Version 8.34a, Bruker AXS Inc: Madison, WI 2013.
- (29) Sheldrick, G. M. SADABS Version 2014/5, Bruker AXS, Inc: Madison 2014.
- (30) Sheldrick, G. M. SHELXTL Version 2014/7, Bruker AXS, Inc: Madison 2014.
- (31) Wilson, A. J. C.; Geist, V. *Cryst. Res. Technol.* **1993**, *28* (1), 110.